# MOLECULAR DESIGN AND PROCESS ASPECTS OF PYROMELLITIC AND OLIGOSILANE SMALL MOLECULE ORGANIC SEMICONDUCTORS

by
Ming-Ling Yeh

A dissertation submitted to Johns Hopkins University in conformity with the requirements for the degree of Doctor of Philosophy

Baltimore, Maryland
March 2014

# ABSTRACT

Organic semiconductors comprise organic molecular or polymeric compounds that contain conjugated electron systems with delocalized molecular orbitals, in which holes and electrons can be transferred between adjacent molecular units under appropriate conditions. If the neighboring molecules become closer and align better, the better orbital overlap will help charge transfer and thus higher mobility, the velocity of charge movement at given electric field, can be achieved.

Pyromellitic diimides (PyDIs) are π-conjugated electron-transport materials based on an unusually small aromatic core (benzene). We synthesized PyDI derivatives with a systematic series of fluoroalkyl side chains and investigated their film structures and electrical performances in thin-film transistors. The effect of the length of the fluorinated segment in fluoroalkylmethylene side chains was examined. Shorter side chains within this series induce higher electron mobilities, with a maximum of 0.026 $cm^2/Vs$ achieved with the perfluorobutylmethyl side chain.

Based on what we learned from the systematic comparison of different side chains, we developed different approaches to explore the potential of the pyromellitic core and further enhance its electrical performance. Attaching the optimized side chain to 3,6-dibromo PyDI allowed nearly parallel PyDI cores and an exceptional mobility of 0.2 $cm^2/Vs$, the highest PyDI mobility yet reported. Compared with other larger conjugated systems, the combination of good mobility and wide bandgap can be obtained from PyDI through a short and relatively benign synthetic process.

We also evaluated different solution process methods for growing oligosilane ordered films and successfully controlled the crystallite alignment in areas with defined shapes. Optimized device schemes and dimensions were developed to confirm the electronic conduction phenomenon and a space-limited charge mobility of 1x$10^{-3}$ $cm^2$/Vs. The testing method offered more understanding toward the utilization of oligosilane as charge transport materials, and suggests the hexasilane core as a promising building block for derivatives with greater substitution and dimensionality.

Fullerenes are an important family in organic electronics, especially in bulk heterojunction organic photovoltaics. A fluoroalkylated fullerene compound was synthesized and evaluated as a solution processable n-type material with mobility of 0.01 $cm^2$/Vs. An iodinated fullerene compound that can be used for X-ray and neutron reflectivity analysis and for further functionalization was synthesized via two different routes and structurally identified.

Polystyrene bilayer thin film stacking schemes were realized using thermally cross-linked polystyrene bottom layer and spin-coated top layer. X-ray and neutron reflectometry further confirmed the film schemes as bilayer with smooth and reflective interfaces, offering the basis to probe more complicated layered device architectures.

Advisor: Dr. Howard Katz

# ACKNOWLEDGMENTS

I would like to express my deepest gratitude to my PhD advisor, Professor Howard Katz, for his support and help throughout my years in graduate school. Professor Katz is an inspirational scientist and wonderful mentor. He is knowledgeable, enthusiastic, efficient, and always willing to listen and provide constructive feedback. Under his mentorship, I was able to tackle numerous obstacles and challenges during my scientific development in the field of organic semiconductor. This thesis would not have been possible without his tireless guidance and continuous encouragement.

I would also like to express my great appreciation for my thesis committee members, Dr. Tim Mueller, Dr. J. D. Tovar, Dr. En Ma, and Dr. Rebekka Klausen for their valuable suggestions and discussions to move my project forward. My sincere gratitude goes to my collaborator— Dr. Sravan Surampudi for his help in the oligosilane project.

In addition, I would like to thank Marge Weaver, Jeanine Majewski, Dot Reagle and Mark Koontz in the Department of Materials Science and Engineering for their excellent administrative support. They put every effort to make sure every requirement and deadline in my PhD study was met, and everything in the lab, big or small, went smoothly.

I am really grateful to be surrounded by a group of brilliant people, alumni and present, in the Katz group. Their varied expertise and willingness to share ideals built an enjoyable research environment.

Lastly, and most importantly, I wish to thank my parents and my sister in Taiwan for their support in these years while I was away from home.

I am also deeply grateful to my beloved wife, Hsing-Chen, for her unconditional love and support, and my dearest daughter, Rong-Jia, for her heart-melting smile, which gives me the courage and strength to withstand ups and downs in my PhD study. To them I dedicate this thesis.

# TABLE OF CONTENTS

# LIST OF FIGURES

# LIST OF TABLES

# CHAPTER 1

## Introduction

### 1.1 Organic Semiconductors

Organic molecules are typically electrical insulators. For organic molecular or polymeric compounds that contain conjugated electron systems with delocalized molecular orbitals (Figure 1-1), holes and electrons can be transferred between adjacent molecular units under appropriate conditions and with appropriate intermolecular spacing.

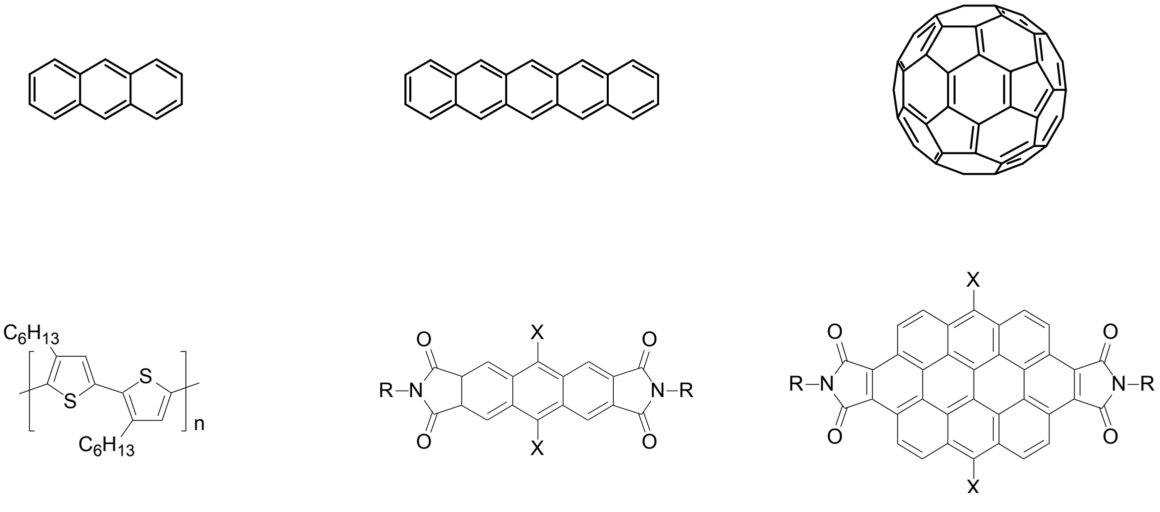

**Figure 1-1 Molecular structures of some common organic semiconductors**

In traditional inorganic semiconductors such as crystalline silicon or germanium, strong covalent bonding holds the composing atoms together and enables band conduction. Organic semiconductor molecules are held together by weak van der Waals bonding. Charge is localized in individual molecules and not delocalized into large energy bands. Each molecule's molecular orbitals play the role of the valence and conduction bands, that is, the highest-occupied-molecular-orbital (HOMO) and lowest-unoccupied-molecular-orbital (LUMO), respectively. The charge transfer is mainly polaron propagation through thermally activated hopping between molecular orbitals of adjacent organic molecules. As a result, if the neighboring molecules become closer and align better, the better orbital overlapping will help charge transfer and thus higher mobility, the velocity of charge movement at given electric field, can be achieved.

Organic semiconducting materials have been investigated intensively for use in light-emitting diodes (OLEDs)[1], organic photovoltaics (OPV)[2], and organic field-effect transistors (OFETs)[3]. However, the hole transporting materials (p-type) have far better mobilities than the electron transporting materials (n-type). Most organic semiconductor are intrinsically p-type, in which the apparent hole mobility exceeds the electron mobility by orders of magnitude. The origin of the low electron mobility is attributed from common trap states that are near the LUMOs of n-type materials but far away from HOMOs of p-type materials.

## **1.2 Experimental Methods for Mobility Determination**

### *1.2.1 Field-effect Transistors*

A field-effect transistor, shown in Figure 1-2, can be view as a two-terminal resistor combined with a capacitor. The current flows between the two terminals, named source (S) and drain (D), is an indication of the conductance of the semiconducting material between the source and the drain electrodes at a given voltage. Furthermore, this resistance is modulated by the capacitor through a third terminal, named gate (G). When a voltage is applied to the gate electrode, a potential gradient is built inside the capacitor structure, the dielectric in the capacitor is polarized, and charge carriers (induced charges) are accumulated at the dielectric/semiconductor interface. As a result, the conductivity of the resistor increases as charge carrier density increases.

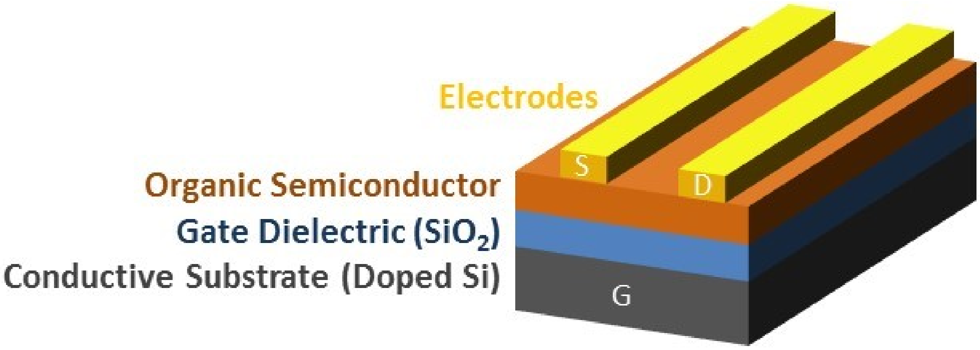

**Figure 1-2 Schematic view of an organic field-effect transistor**

**S is the source electrode, D is the drain electrode, and G is the gate electrode**

Without intentionally doping, charges are injected from the source electrodes and extracted from drain electrodes. In most cases, there is mismatch between the Fermi level of metal electrodes and HOMO of p-type semiconductors or LUMO of n-semiconductors. The mismatch in energy levels induces charge injection barriers, which requires a gate voltage ($V_G$) to shift the molecular orbital levels of semiconductors up or down to align with the Fermi level of metal electrodes. In addition, not all induced charges are mobile and contribute to the current flows though the semiconductor. Trap states, induced from impurities and defects including grain boundaries, have to be filled before additional induced charges become mobile. Thus, gate voltage ($V_G$) higher than a threshold voltage ($V_{TH}$) has to be applied to induce effective charges in the conduction channel, and the effective applied voltage becomes $V_G – V_{TH}$.

Typical current–voltage (I-V) curves obtained from the operation of field-effect transistors are illustrated in Figure 1-3. Due to their low intrinsic conductivity, when there is no applied gate voltage $V_G$ organic semiconductors are normally in the OFF state, meaning very low or no current flows between source and drain electrode, as demonstrated by the lines in the bottom of the left panel of Figure1-2. After applying certain gate voltage $V_G$, as described in previous section, noticeable increases in currents ($I_D$) can be measured. At a fixed $V_G$, the current first increases linearly with the increasing $V_D$ (linear region), and then saturates at certain current level (saturation region). The saturation current of $I_D$ increases with $V_G$, and ideally, is proportional to the square of effective applied voltage $V_G – V_{TH}$. The saturation current $I_D$ is given by the following equation:

$$I_D = \frac{W}{2L}\mu C_i (V_G - V_{TH})^2$$

where $W$ is the width of the conduction channel, $L$ is the length of the conduction channel between source and drain electrodes, $\mu$ is the mobility of charge carriers, and $Ci$ is the capacitance per unit area of the dielectric.

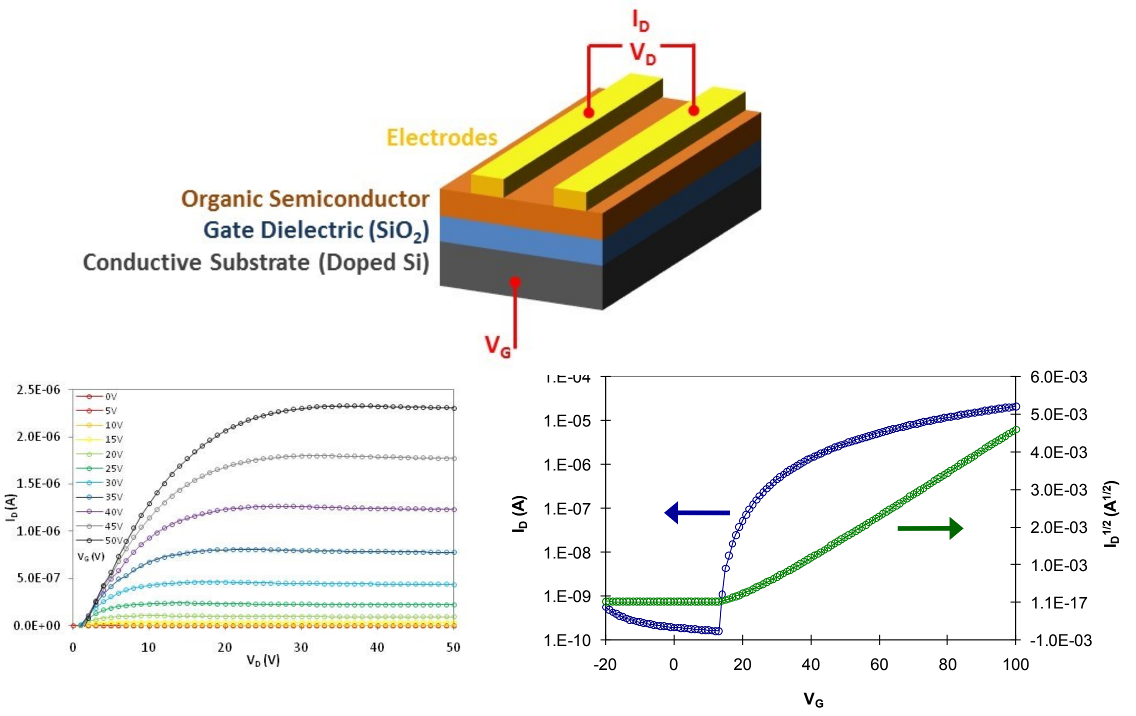

**Figure 1-3 I-V curves of an organic field-effect transistor**

**(left) output curve; (right) transfer curve**

### *1.2.2 Space-charge limited current (SCLC) measurements*

Organic semiconductors have a relatively low density of free charge carriers. As shown in Figure 1-4, under certain applied voltage, all the charge carriers will be injected and not be compensated. This gives the organic semiconductor a net charge, named space charge.[4] In a trap-free intrinsic organic semiconductor, the current density $J$ is given by the Mott–Gurney law:

$$J = \frac{9\epsilon\mu V^2}{8L^3}$$

where $\epsilon$ is the permittivity, $\mu$ is the mobility, $V$ is the voltage applied, and L is the channel length.

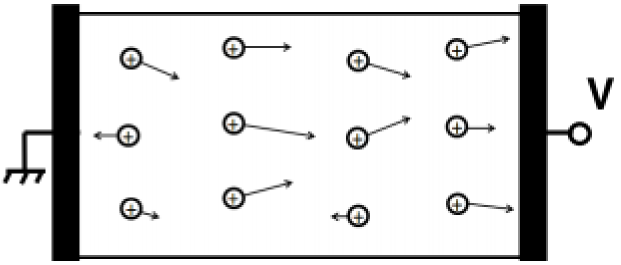

**Figure 1-4 The formation of space charge**

Measuring the current density at applied voltage, the mobility can be extracted from the $J^{1/2} - V$ plot.

# CHAPTER 2

## Effect of Side Chain Length on Film Structure and Electron Mobility of Pyromellitic Diimides

---

### 2.1 Introduction

Organic semiconductors (OSCs) comprise small molecules or polymers bearing closely spaced π-conjugated systems. The molecular constituents can be chemically tailored[5] to meet particular solubility/volatility, photophysical, or electron/hole stability requirements, and are promising building blocks in a wide range of electronic applications.[6-8] Numerous extensive studies have been conducted on the development of high performance organic semiconducting materials. Charge carrier mobility is an important quantity in characterizing the performance of organic semiconductors. It is the measurement of how fast charge carriers migrate under a given electric field, and can be viewed as the overall result in the processes of injection, trapping and transport of charge carriers. Charge injection and trapping processes are determined by the metal/semiconductor and semiconductor/dielectric interfaces, and thus are strongly correlated to the relative energy levels of the materials and microstructure along the interfaces. Charge transport in OSCs is generally depicted in the framework of the two limiting cases of a small polaron propagating by thermally activated hopping between organic molecules (carrier localization on each lattice site) and a coherent band-like transport in extended states (delocalized carriers).[9-10] Realization of either hopping or band-like regimes depends on the reorganization energy and the intermolecular electronic coupling.[11] Reorganization energy is mainly the energy change from distortion of molecules upon charge addition and removal; intermolecular coupling can be approximated as the contribution from π-overlap of nearest neighbors. Cofacial stacking of π-planes leads to better orbital overlap.[12-13] Thus, large, rigid, stacked π systems provide the strongest intermolecular interactions leading to charge delocalization and band-like conduction in single-component organic semiconductors, such as rubrene single crystals, which holds the record for hole mobility of 5-20 $cm^2/Vs$ (depending on the crystallographic orientation and device type).[14] Conversely, it is challenging to obtain high mobilities from OSCs with low deposition temperatures and transparency in the visible range, important for high-throughput electronics on displays and windows.

Numerous factors, including molecular structure and process conductions, change the ordering of common organic molecules, and these principles can also be applied to semiconducting organic molecules.[15-16] Disordered solid states are not considered to be optimal for conduction; therefore, controlling charge transport process through manipulating molecular order has been demonstrated via modification of substrate type and process temperature.

To realize the intrinsic potential of certain conjugated systems, it is necessary to systematically study the behavior of series of molecules to unveil the correlation between molecular structure and electrical performance. Compared to semiconducting polymers, small molecule organic semiconductors offer materials with high purity and well-defined structure, and thus are more suitable for examining structure-performance relationships of organic semiconductors.

Molecules based on polycyclic aromatic hydrocarbon cores are an important family in small molecule organic semiconductors. Among electron transporters, important for complementary circuit elements, arylenediimides including naphthalenetetracarboxylic dimide (NTCDI), perylenetetracarboxylic diimide (PTCDI), and pyromellitic diimide (PyDI) derivatives with different moieties on either the conjugated core or the nitrogen terminals have been employed.[17] While attaching substituents on the conjugated core generally changes the energy levels of the molecule, the side chain tethered to the nitrogen terminals has little effect on molecular energy levels. Core-fluorination has been used as a route to enhance the stability of organic semiconductors by lowering the energy levels.[18] Replacing alkyl substituents with their fluorinated counterparts on NTCDI greatly improves the operability of NTCDI derivatives in air, likely because of protection of the core from oxygen and moisture rather than from changes in orbital energies.[19] Fluorination can also lower the sublimation temperature needed for OSC purification.[20]

PyDIs are electron-transporting materials based on a small aromatic core[17] which is favorable for low-temperature deposition and processing, as well as transparency. Due to their relatively smaller conjugated core (benzene), the substituents would be expected to have a greater influence on the physical and chemical properties of the molecule than would be the case for larger cores. While we already demonstrated reasonable electron mobilities from PyDIs, no systematic study of effects of N-substituent length on PyDI characteristics has been done. Here, we studied packing behavior and electrical performance on thin films sublimed from PyDIs with regularly varied, prototypical side chains. Instead of the more complicated solution deposition that involves more thermodynamic and kinetic factors, vapor deposition process gave stable, well-controlled growth of thin films. Packing behavior and electrical performance were studied on the thin films fabricated from the molecules. Furthermore, an optimal side chain length were determined from the correlation between solid state structure and mobility with the lengths.

## 2.2 Structure-performance Relationships

### *2.2.1 Materials, Thermal Properties and Molecular Energy Levels*

The PyDI derivatives with series of side chains were synthesized by reacting pyromellitic dianhydride with corresponding amines, as shown in Figure 2-1. To ensure high purity for reliable electric property evaluation, the products were further purified by sublimation under high vacuum. Elemental analysis on carbon, hydrogen, nitrogen, and fluorine contents confirmed these molecules were obtained with high purity.

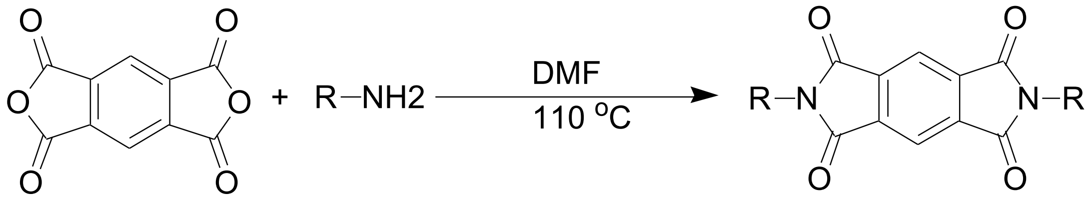

| | | |
|---|---|---|
| R= | $C_3F_7CH_2$ | **3-1-PyDI** |
| | $C_4F_9CH_2$ | **4-1-PyDI** |
| | $C_5F_{11}CH_2$ | **5-1-PyDI** |
| | $C_6F_{13}CH_2$ | **6-1-PyDI** |
| | $C_7F_{15}CH_2$ | **7-1-PyDI** |
| | $C_8F_{17}CH_2$ | **8-1-PyDI** |
| | $C_{10}F_{21}CH_2$ | **10-1-PyDI** |
| | $C_8F_{17}C_3H_6$ | **8-3-PyDI** |

**Figure 2-1 Structures and preparation of the PyDI derivatives**

The thermal properties were investigated by differential scanning calorimetry (DSC). As shown in Figure 2-2, all PyDIs exhibited good thermal stability over the temperature range examined. Each compound exhibits only one reversible thermal transition process in the DSC thermogram that corresponds to its melting and the corresponding recrystallization peaks. No features assignable to glass transitions nor transitions indicating mesophases were observed. As the length of the fluoroalkyl segment increases, the melting point first drops from 202°C (3-1-PyDI) to 155°C (5-1-PyDI) and then keeps increasing to 197°C (10-1-PyDI). For PyDI with the same side chain length of 11 carbons, partially replacing the alkyl with fluoroalkyl also lowers the melting point (8-3-PyDI = 224°C, 10-1-PyDI = 197°C).

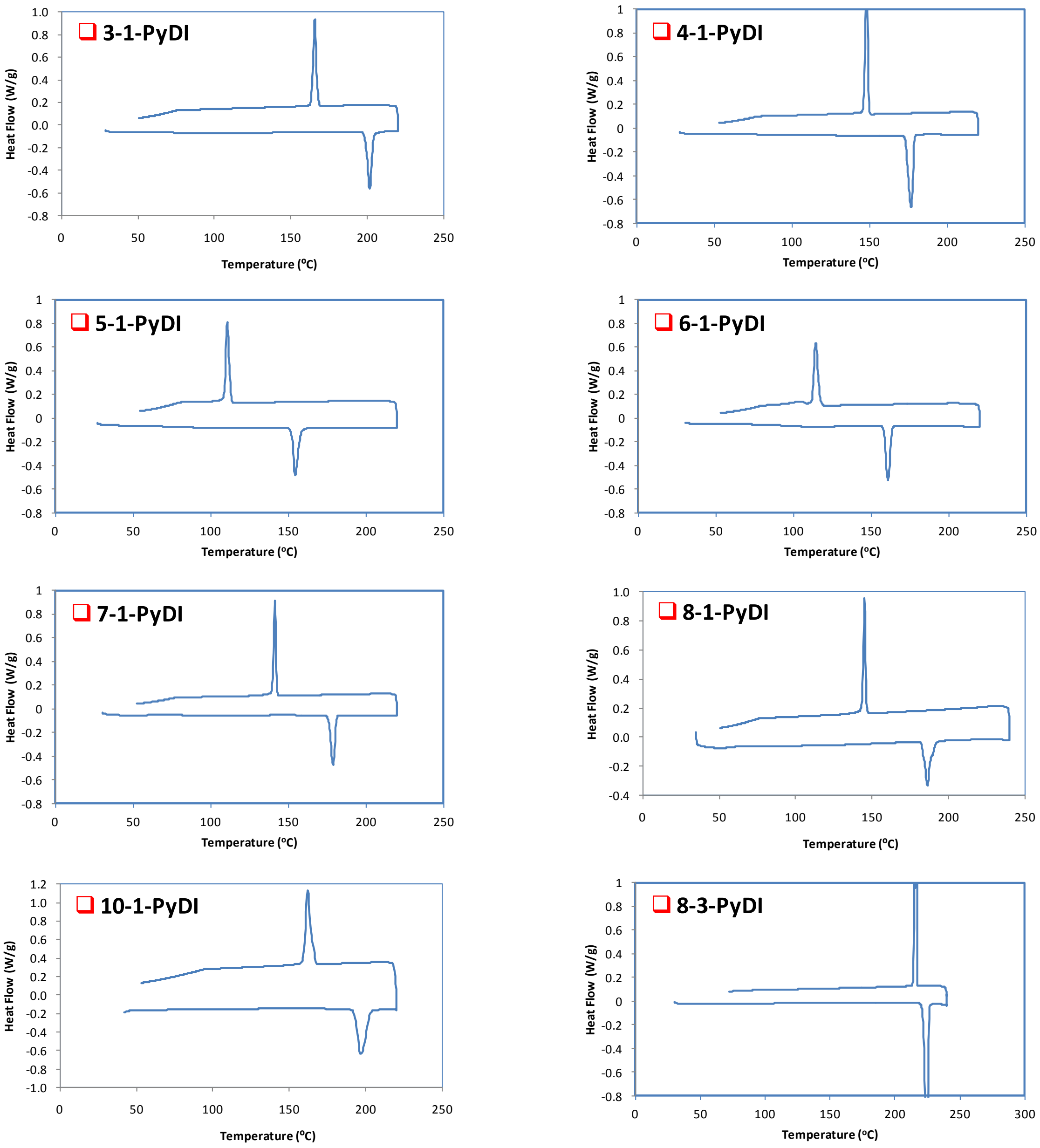

**Figure 2-2 DSC Thermograms of the PyDI derivatives (exothermic up)**

Since the relative energy levels are important factors in determining charge injection and transport in organic semiconductors[22] it is essential to understand how the different side chains affect the molecular energy levels of the PyDI compounds. The lowest unoccupied molecular orbital (LUMO) levels of the molecules are characterized using cyclic voltammetry (CV) in solution and are shown in Figure 2-3. While PyDIs with methylene linkers between the core and the fluoroalkyl termini (n-1-PyDI) have the same reduction onset potential in their CVs, PyDIs with a longer propylene linker (8-3-PyDI) shows a slightly more negative reduction onset potential, indicating that the LUMO level of 8-3-PyDI is only about 0.1eV higher than that of n-1-PyDI, as a result of the weaker inductive effect due to the electron-withdrawing fluoroalkyl tether being further away from the π-conjugated core. Furthermore, the LUMO levels are primarily determined by the alkyl linker length; the variations in fluoalkyl side chain length have little effect on the conjugated cores.

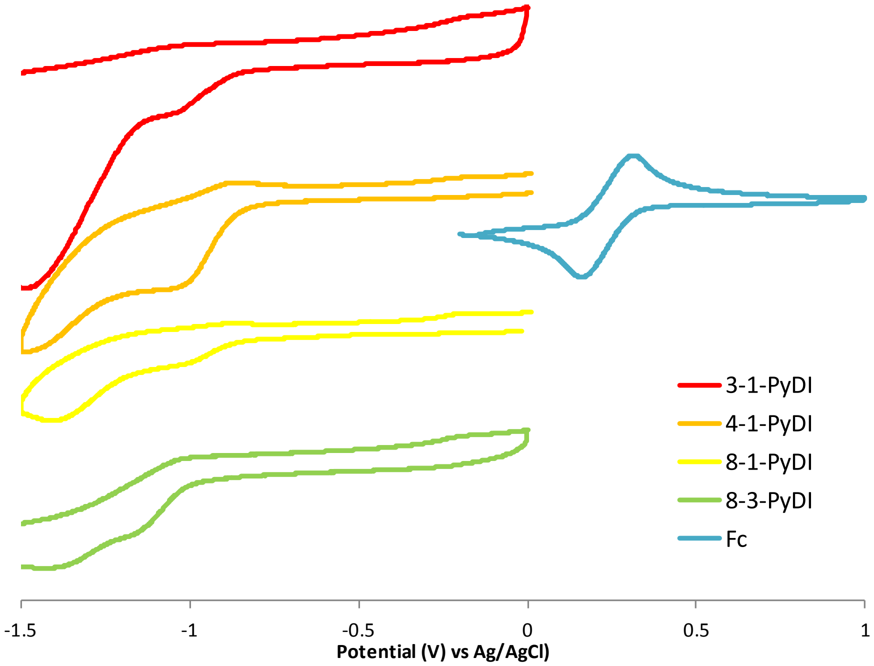

**Figure 2-3 Cyclic Voltammograms of the PyDI derivatives**

**Ferrocene (Fc) was used as an internal standard**

This similarity is also seen in the optical band gaps. The optical band gaps of the PyDIs were estimated from the onset wavelength in their UV absorption spectra in solution, as shown in Figure 2-4. Again, PyDIs with the same methylene linker showed the same optical band gap of 3.76eV, whereas the one with propylene linker has a slightly smaller optical band gap of 3.65eV.

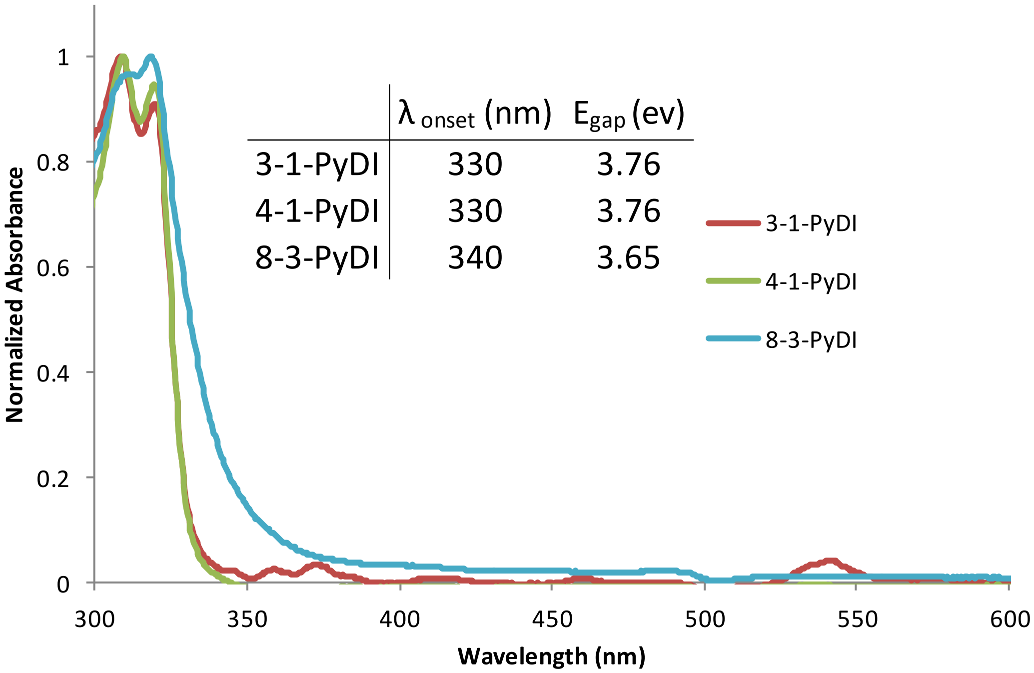

|  | $\lambda_{onset}$ (nm) | $E_{gap}$ (ev) |
|---|---|---|
| 3-1-PyDI | 330 | 3.76 |
| 4-1-PyDI | 330 | 3.76 |
| 8-3-PyDI | 340 | 3.65 |

**Figure 2-4 UV-Vis Spectra of the PyDI derivatives**

Since the n-1-PyDIs have the same HOMO and LUMO levels, relative energy level is not a factor that differentiates the mobilities in these molecules. Their mobilities are instead determined mainly by how the molecules pack in the thin film crystal structures.

### *2.2.2 Thin Film Stacking*

The thin film structures of PyDIs were studied by X-ray diffraction (XRD) for PyDI thin films vacuum-deposited on Si/SiO2 substrates with different surface treatment and varied substrate temperature. With optimized deposition conditions, several orders of the layer diffraction were observed for all PyDI derivatives. As depicted in Figure 2-5, PyDIs with shorter side chains exhibit higher degrees of texture orientation in thin films, shown both in higher intensity of the peaks and narrower full-width-at-half-maximum (FWHM). Also, the d-spacings are close to the calculated molecular lengths, suggesting the molecules stand almost perpendicular to the substrate surface and form layer structures that favor the π–π stacking in the horizontal direction, which would also be the charge transport direction.

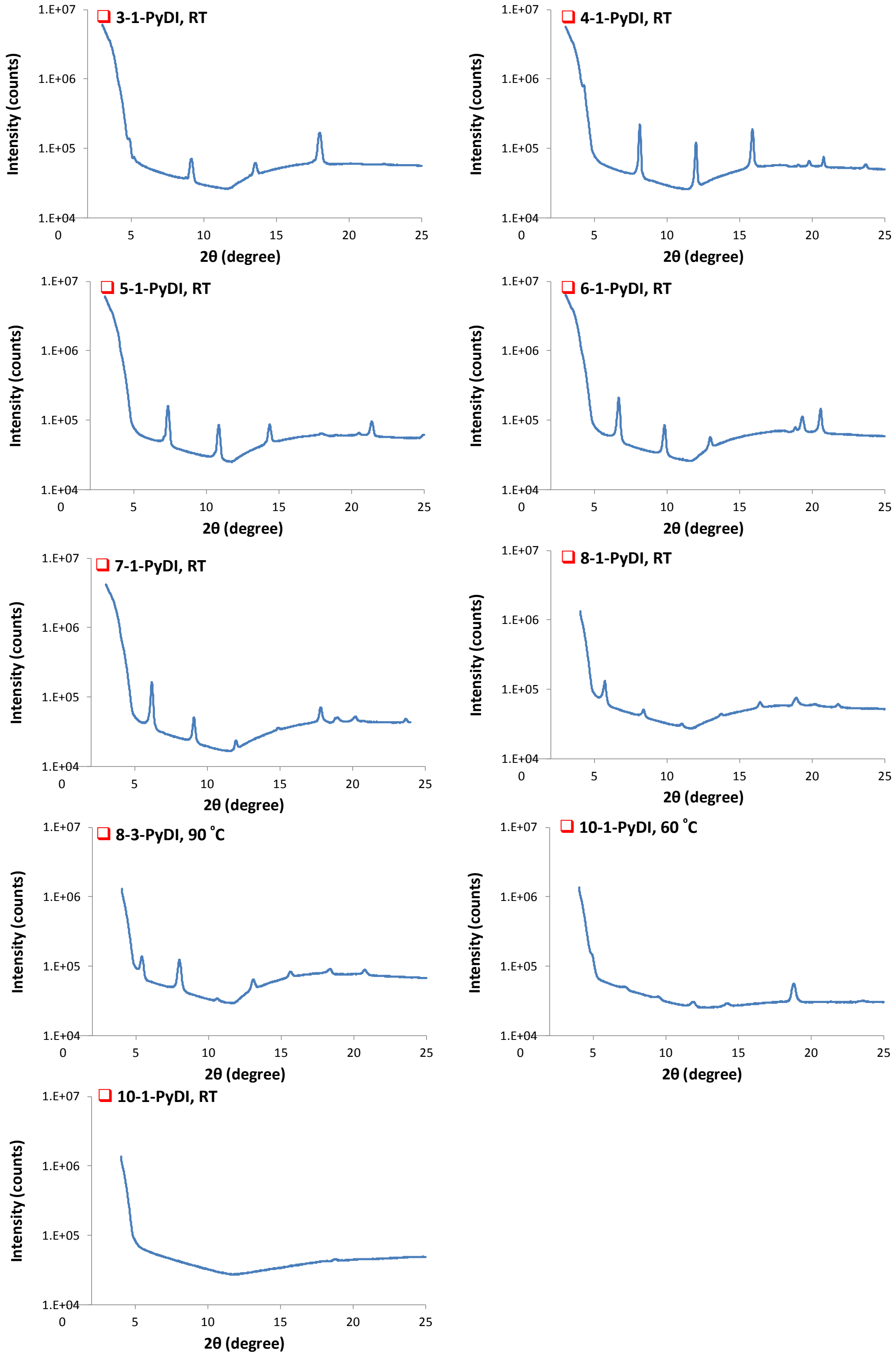

Figure 2-5 X-ray Diffraction for thin films of series of PyDIs.

In single crystals or thin films, the sum of weak intermolecular forces such as van der Waals, hydrogen bonding and π–π interactions determine the final stacking structure. When a molecule is partially fluorinated, the fluorinated segments tend to self-associate and segregate from non-fluorinated counterparts. Long fluoroalkyl tethers could conceivably lead to better alignment and packing of molecules. However, the experimental results indicate that this is not the case for PyDIs. As summarized in Table 2-1, the aromatic segment accounts for less than 10% of the molecule length in these PyDI molecules. If we consider the entire non-fluorinated segment (between two terminal nitrogen atoms), a longer fluorinated end group makes the percentage of the non-fluorinated segment smaller. In 10-1-PyDI, this portion becomes less than 30%. When only a small portion of the molecule is non-fluorinated, that is, when most of the molecule is fluorinated, the energy penalty of disorder or "wrong stacking" is reduced. As shown in Figure 2-5, 10-1-PyDI formed an amorphous film when deposited at room temperature. Only at higher substrate temperature does 10-1-PyDI from a more ordered thin film.

| | **Molecular Length (Å)** | **Percentage of Non-fluorinated Segment** |
|---|---|---|
| 3-1-PyDI | 18.3 | 52% |
| 4-1-PyDI | 20.6 | 46% |
| 5-1-PyDI | 24.5 | 39% |
| 6-1-PyDI | 27.0 | 35% |
| 7-1-PyDI | 29.6 | 32% |
| 8-1-PyDI | 32.1 | 30% |
| 10-1-PyDI | 35.8 | 27% |
| 8-3-PyDI | 35.8 | 39% |

**Table 2-1 Calculated length of the molecule and different segments.**

### *2.2.3 Optimization of Thin Film Process Conditions*

In order to fairly compare the electrical performances of different PyDI molecules, we chose well-controllable vapor deposition to avoid having to control for solvation and solvent removal processes during solution deposition. Still, finding an optimized vapor deposition process condition that can serve as a standard platform for these PyDI molecules is important.

Surface conditions, including substrate temperature and surface treatment with self-assembled monolayer (SAM), can greatly change the thin film solid structure and its electrical performance. XRD spectrum and transistor I-V curves of two PyDIs with long side chains are shown in Figure 2-6 and Figure2-7. Each compound were thermally evaporated on SiO2/Si substrates prior treated with octadecyltrimethoxysilane (OTS) hexamethyldisilazane (HMDS) as SAM on the surface. With 8-1-PyDI, both surface treatment gave crystalline thin film when the molecule was deposited without heating the substrate (room temperature). While devices from both surface treatment demonstrated gate voltage-modulated transistor behavior, OTS gave slightly higher mobility (1.79 x $10^{-3}$ $cm^2/Vs$) than HMDS did (1.56 x$10^{-3}$ $cm^2/Vs$).

When it comes to 10-1-PyDI, deposition at room temperature substrate showed no XRD peaks, indicating an amorphous solid state structure; and the amorphous films did not exhibit transistor activity. Only when depositing the material on the substrate heated at 60°C did it show XRD peaks, and just OTS treatment at this condition gave transistor activity.

Based on these results, thermally evaporation on room temperature substrates with OTS was chosen as the optimized standard test platform for the series of PyDI molecules.

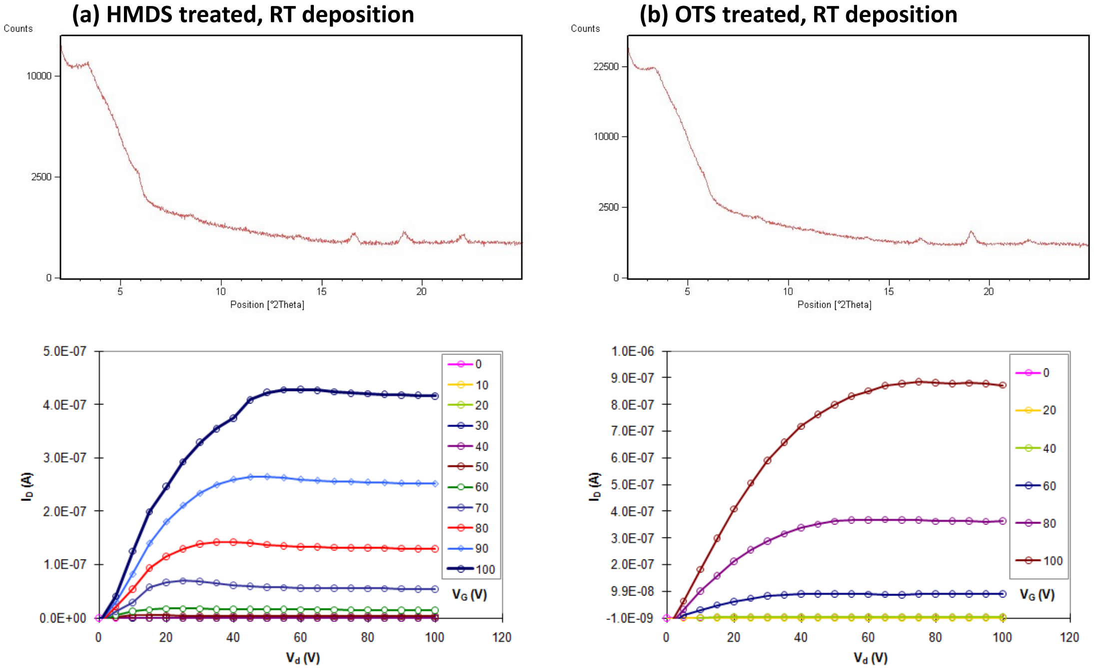

**Figure 2-6 XRD and transistor behavior 8-1-PyDI with different surface treatment and substrate temperature.**

(a) HMDS treated, RT deposition

(b) OTS treated, RT deposition

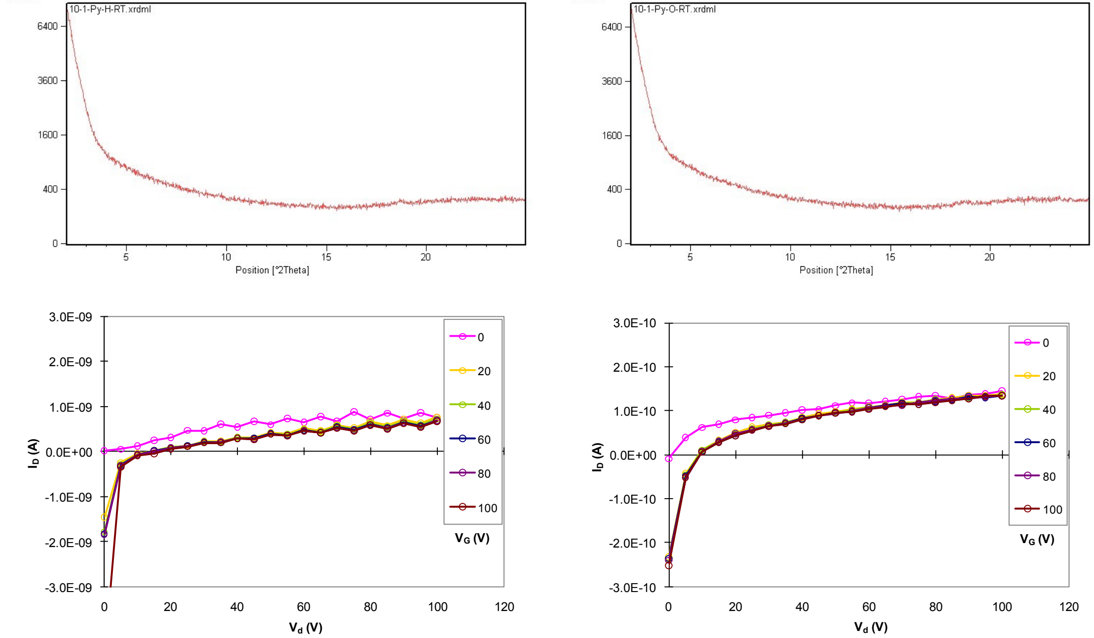

(c) HMDS treated, 60 $^0$C deposition

(d) OTS treated, 60 $^0$C deposition

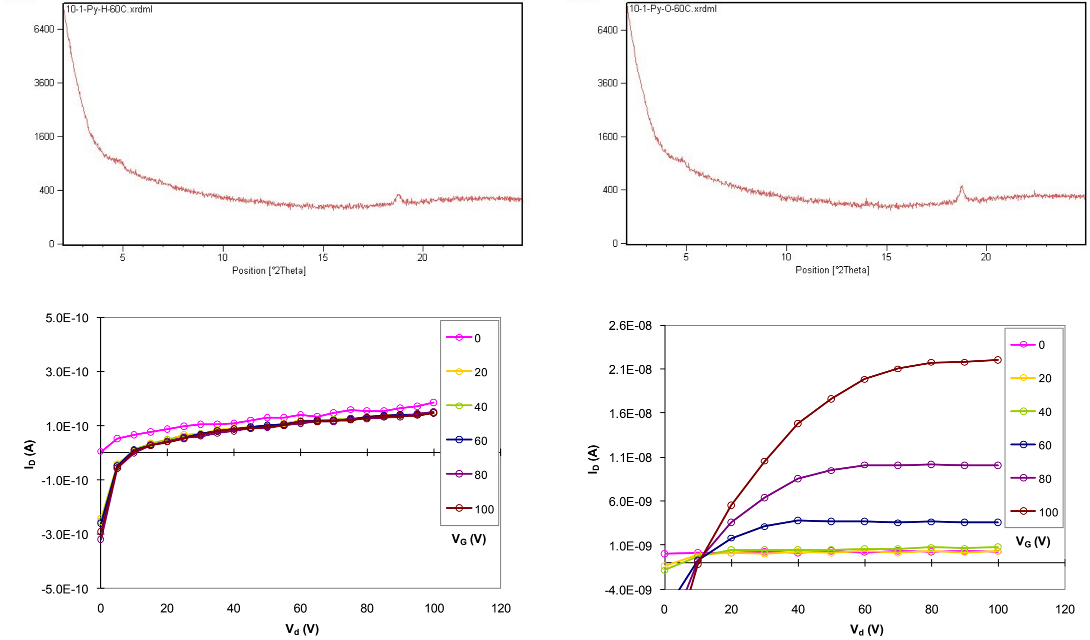

**Figure 2-7 XRD and transistor behavior 10-1-PyDI with different surface treatment and substrate temperature.**

### *2.2.4 Fabrication and Characterization of Thin-Film Transistors*

Thin-film transistors in top-contact/bottom-gate (TCBG) configuration were fabricated using thermally evaporated PyDIs and gold as the semiconducting layer and electrode, respectively, on heavily-doped silicon with 300 nm thermal oxide dielectric layer. Under optimized process conditions, all materials exhibited gate voltage-modulated transistor behavior, as shown in Figure 2-8. The length of the fluorinated segment of the side chain has a significant effect on the mobility of the molecules, as can be seen from mobilities of transistors fabricated from series of PyDIs shown in Figure 2-6. Among the PyDIs with varied perfluoroalkyl lengths and a common alkylene part, 3-1-PyDI exhibits mobility of 0.016 $cm^2/Vs$, and 4-1-PyDI shows a higher mobility of 0.026 $cm^2/Vs$ when deposited at room temperature (Figures 2-9). As the length of the perfluoroalkyl tether was increased to 5, 6, 7, and 8 carbons and deposited at room temperature, the corresponding PyDIs show a decreasing mobility trend, with the lowest mobility around $1.4 \times 10^{-3}$ $cm^2/Vs$ observed in 7-1-PyDI and 8-1-PyDI. Although PyDIs with longer fluoroalkyl side chains can be deposited at higher temperature, 4-1-PyDI still exhibits the highest mobility at achievable temperatures for individual derivatives. The mobilities of the molecules show strong correlation to the crystallinity of the deposited films; the molecules exhibiting better crystallinity led to higher mobility.

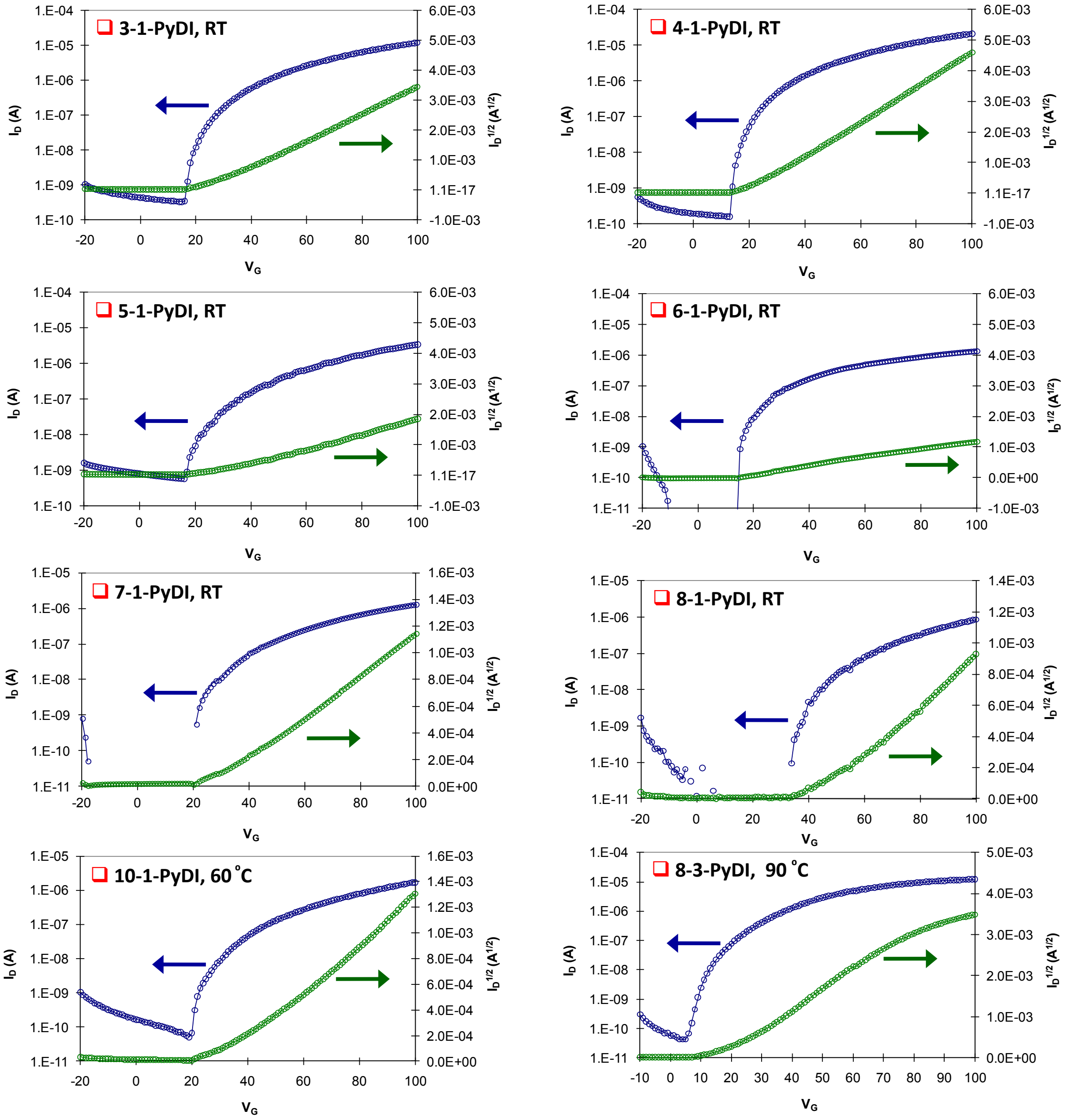

Figure 2-8 Transfer curves of transistors fabricated from series of PyDIs

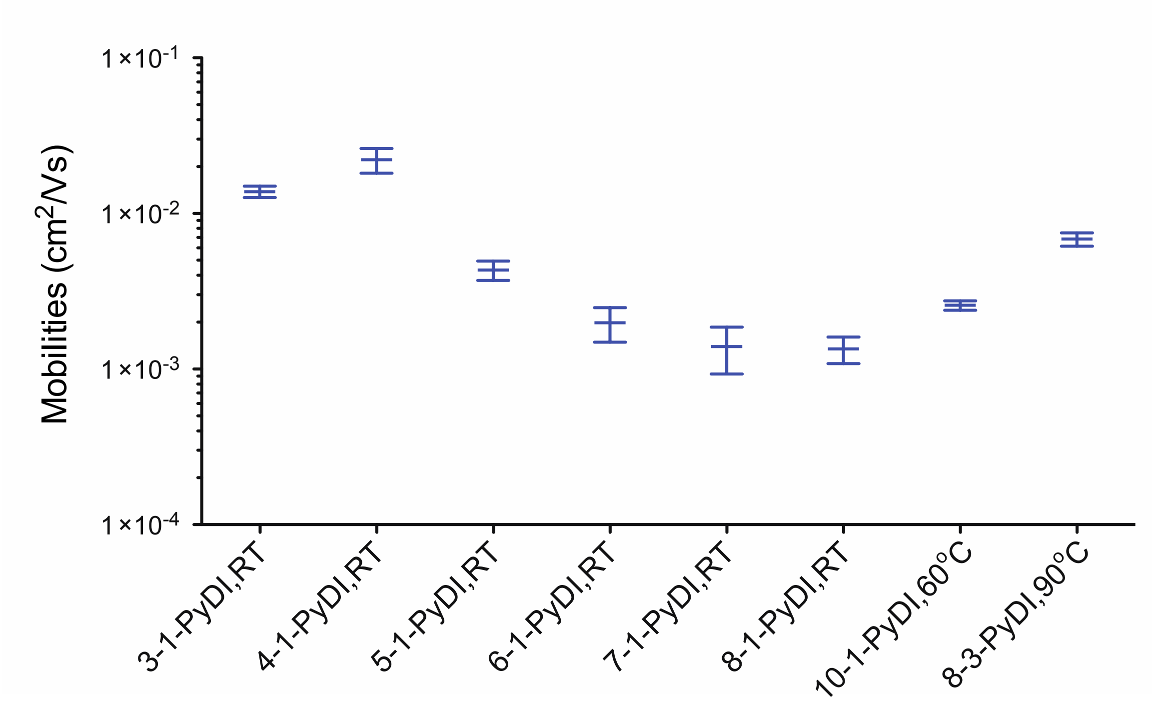

**Figure 2-9 Mobilities of series of PyDIs**

**Error bars were presented as average value plus/minus one standard deviation. 3-1-PyDI data were obtained from 13 devices; 4-1-PyDI data were obtained from 16 devices; 5-1-PyDI data were obtained from 9 devices; 6-1-PyDI data were obtained from 6 devices; 7-1-PyDI data from were obtained 8 devices; 8-1-PyDI data were obtained from 6 devices; 10-1-PyDI data were obtained from 5 devices; 8-3-PyDI data were obtained from 4 devices.**

The good crystallinity and high mobility of 4-1-PyDI is also was validated from the Atomic force microscopy (AFM). The AFM images of 4-1-PyDI thin film shown in Figure 2-10 revealed the presence of smooth surface with large and well-connected grains that contributed to the high mobility.

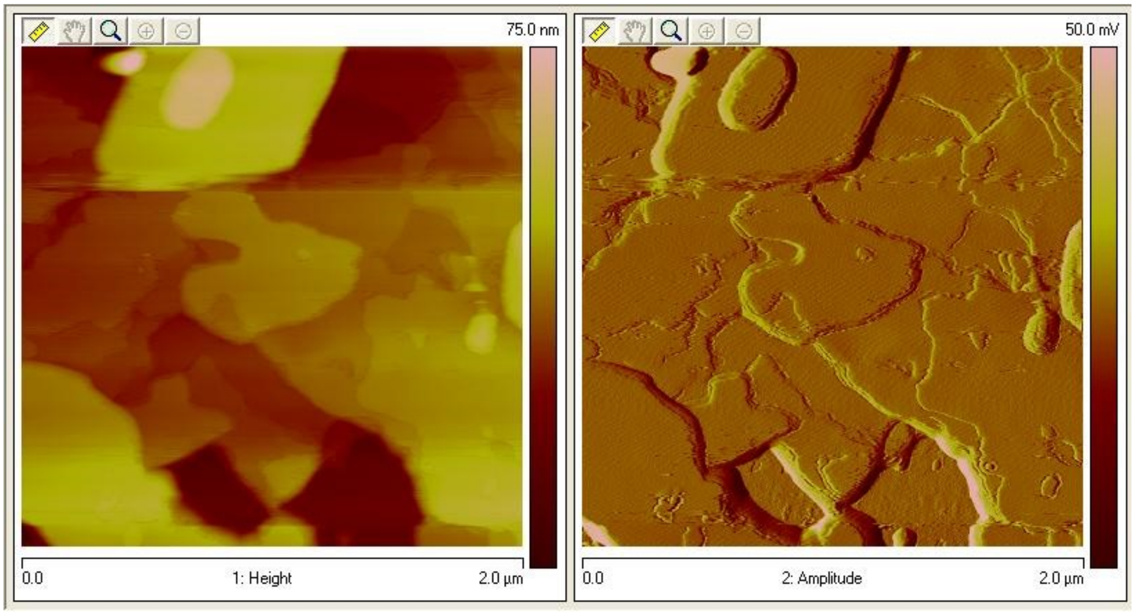

**Figure 2-10 AFM image of 4-1-PyDI thin film**

While the 3-(perfluooctyl)propyl side chain, among the substituents with the same perfluorooctyl group attached to different alkylene chains ranging from one to four carbons, gives particularly high mobility (five to fifty times higher) on the naphthalene core,[23] it does not provide the same beneficial effect on the smaller benzene core in PyDIs (3.6 times higher). The side chain alone does not determine how the molecule packs in its solid state. Packing is the combined result of the interaction between conjugated cores, side chains, and surface energy. Thus the optimized side chain for better molecular ordering differs among systems with varied core sizes. As has also been demonstrated in the pentacene derivatives, shorter side chains improved the π–interactions. Hexyl and longer side chain in the alkylethynl or alkyl(diisopropylsilylethynyl) group attached to pentacene lead to stronger interaction between the side chain and the core, insulating the pentacene from adjacent pentacene units and eliminating the preferred π–stacking interactions.[24] It is also noteworthy that the side chains serve electrically as a dielectric, rather than a conduction segment. As the side chain becomes longer, the non-conducting portion becomes larger in the overall thin film structure. Therefore, even if a longer side chain using certain process conditions may offer better packing, some of the benefits will be lost due to the larger insulation portion. Thus, the optimized length is a balance between minimizing the insulating portion and maximizing the ordering effect.

The densely-packed fluorocarbon groups of the PyDIs in their highly ordered thin-film microstructures seem to act as a kinetic barrier to $O_2$/$H_2O$ trap penetration, leading to air operability. For example, 6-1-PyDI devices showed mobility of 0.018 $cm^2/Vs$ under vacuum and retained mobility of 0.014 $cm^2/Vs$ after 10 minutes exposure to air. Many tetracarboxylic diimide compounds with ordinary N-alkyl substituents, such as N,N'-dioctyl-NTCDI, immediately lose electron mobility on exposure to air.[17]

## 2.3 Other Properties of PyDI

### *2.3.1 Contact Resistance*

When charge carriers travel across interfaces, there is inevitably some resistance coming from the differences in energy level on each sides. To understand how much the contact resistance at the interface between metal electrodes and organic layer are accounted in the electrical property measurements, 8-3-PyDI devices with varying distance (channel length) between electrodes were fabricated and tested. From the plot of total resistance vs channel length in Figure 2-11, contact resistance is the resistance when channel length equals zero, and can be calculated as 2.08MΩ at $V_G$=50V and 1.19MΩ at

$V_G$=45V. The PyDI devices used for mobility calculation has channel length of 270µm. At this channel length, only 10% of the total resistance comes from contact resistance; thus the low contact resistance ensures reliable mobility measurements.

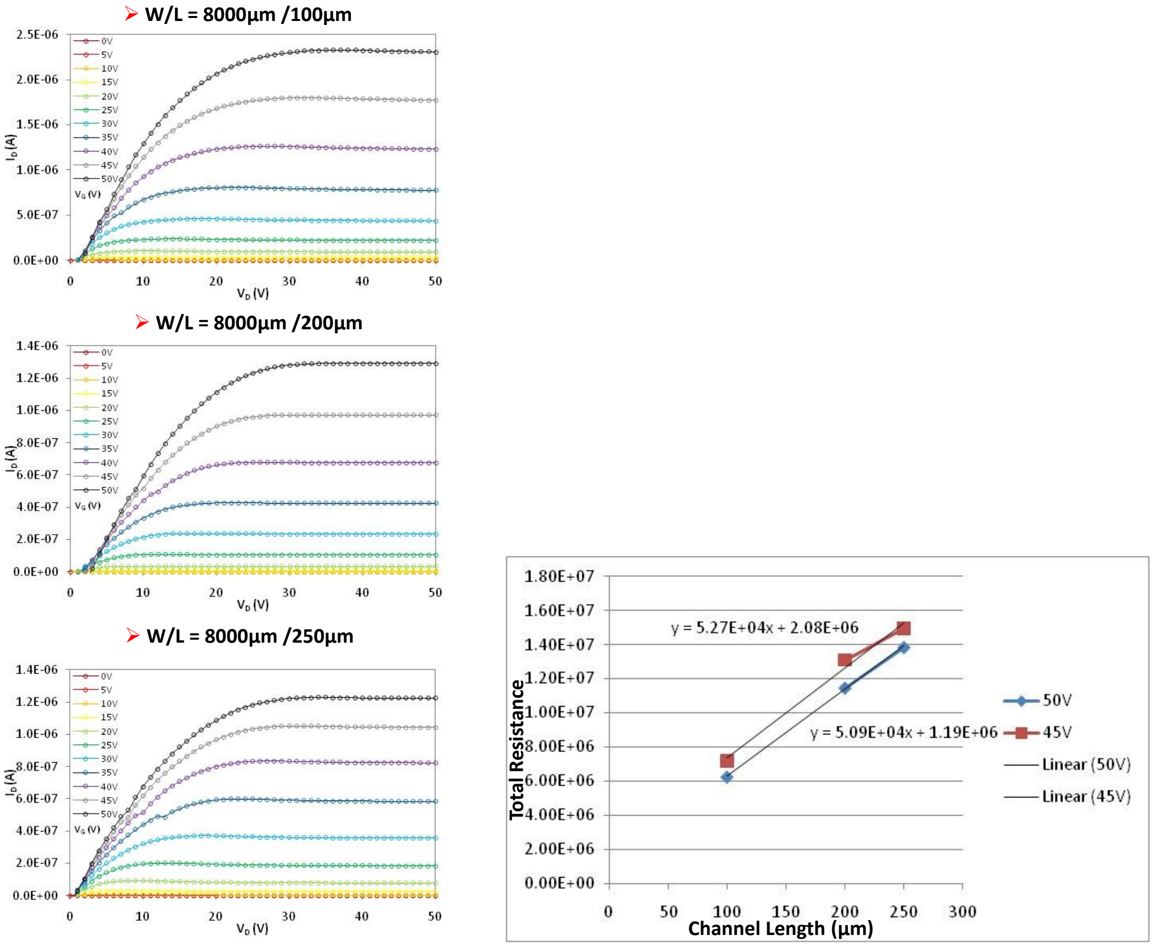

➤ W/L = 8000µm /100µm

➤ W/L = 8000µm /200µm

➤ W/L = 8000µm /250µm

**Figure 2-11 8-3-PyDI devices with varying distance between gold electrodes**

### *2.3.2 Effect of UV Exposure on Electrical Properties*

The large band gap of PyDIs makes them relatively transparent to visible light, and sensitive to UV. The transfer curves of 8-1-PyDI in dark and under irradiation with 254nm UV light are illustrated in Figure 2-12. Upon UV illumination, the 8-1-PyDI transistor exhibited a significant photoresponce at all applied gate voltages ($I_{UV}/ I_{dark}$ = 12.6 at $V_G$ = 50V and 2.1 at $V_G$ = 100V), indicating the additional charge carriers generated from the photogeneration of excitons.[25] The UV exposure does not alter the charge carrier mobility, as can been seen from the similar slope of the curves in the lower panel of Figure 2-12, and the threshold voltage was found to be lowered from 39V to 2V after 3 minutes of UV irradiation. A similar phenomenon was also observed in the devices based on the larger conjugated core perylene tetracarboxylic diimide (PTCDI).[26] The lowering of the threshold voltage is believed to be attributed to the lower electron transport barrier in the conducting channel due to the additional charge carriers induced in the channel[27] and compensation of the local field that opposes the gate voltage at the dielectric interface.[28]

The increase in drain current arising from the lowering in threshold voltage did not immediately diminish after removal of the UV irradiation, but only recovered gradually to values from before UV exposure. Significant shift can still be observed even after several minutes and continuous measurements. This “memory effect” can be used to record the UV exposure history of the device.

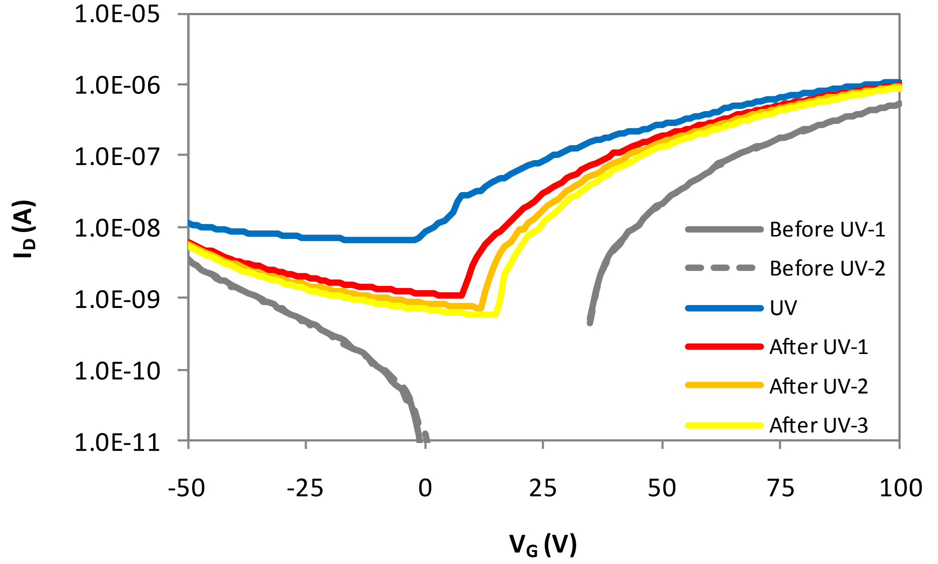

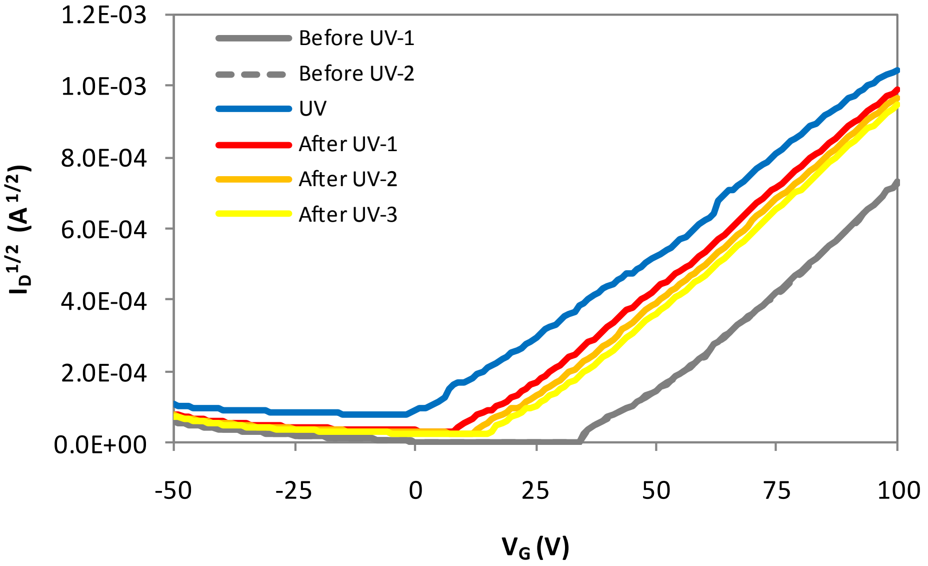

**Figure 2-12 The transfer curves of 8-1-PyDI**

**In dark (Before UV-1, Before UV-2) and under irradiation with 254nm UV light for 3min (UV). After removal of UV source, each measurement was taken 1min apart (After UV-1, After UV-2, After UV-3).**

## 2.4 Conclusions and Outlook

We have synthesized PyDI derivatives with series of side-chains and investigated their film structures and electrical performances in thin-film transistors. For this small conjugated benzene core, a shorter fluoroalkyl side chain was found to yield highly order structure thin film and allow better electron transport. The systematic comparison of different side chains advances our understanding to relationship between molecular structure and its properties, enables a rational design of small molecules and also extends its application to polymers[29] for optimal electrical performance.

## 2.5 Experimental Section

### General

$^1$H NMR spectra were recorded with a Bruker Avance 400 MHz spectrometer. Elemental analyses were performed by Atlantic Mircolab (Norcross, Georgia). DSC measurements were carried out with a TA Instruments DSC Q20 at a heating and cooling rate of 5 °C/min under a nitrogen atmosphere. The electrochemical measurements were carried out in dichloromethane solutions under nitrogen with 0.1M tetrabutylammonium hexafluorophosphate ($NBu_4PF_6$) as the supporting electrolyte at room temperature using an EG&G Instruments 263A potentiostat/galvanostat. The cyclic voltammograms were obtained at a scan rate of 100 mV/s. A platinum disk and platinum wire were used as the working and counter electrode, respectively; Ag/AgCl in 3 M NaCl aqueous solution was used as the reference electrode. UV−vis absorption spectra were collected in dichloromethane solutions using a Varian Cary 50 Bio UV-Vis spectrophotometer. X-ray diffraction scans were acquired in the Bragg-Brentano (θ-2θ) geometry using a Phillips

X-pert Pro X-ray diffraction system. Scan step size was 0.02° and time per step was 2 seconds.

**N, N'-Bis(1H,1H-perfluoropentyl)pyromellitic diimide (4-1-PyDI)** were prepared as reported previously.[21] Other PyDI derivatives were synthesized using the same procedure of 4-1-PyDI: pyromellitic dianhydride was reacted with corresponding amines in DMF overnight at 110$^0$C, and the white solid obtained after filtration was further purified by sublimation under high vacuum.

**N, N'-Bis(1H,1H-perfluorobutyl)pyromellitic diimide (3-1-PyDI)** $^1$HNMR (400MHz, $CDCl_3$): 8.46(s, 2H), 4.45(t, 4H, $J$ = 15.0 Hz). Elemental analysis: Calcd for $C_{18}H_6F_{14}N_2O_4$, C, 37.26; H, 1.04; F, 45.84; N, 4.83. Found: C, 37.47; H, 1.00; F, 44.57; N, 4.92.

**N,N'-Bis(1H,1H-perfluorohexyl)pyromellitic diimide (5-1-PyDI)** $^1$HNMR (400MHz, $CDCl_3$): 8.47(s, 2H), 4.46(t, 4H, $J$ = 15.2 Hz). Elemental analysis: Calcd for $C_{22}H_6F_{22}N_2O_4$, C, 33.87; H, 0.78; F, 53.57; N, 3.59. Found: C, 33.93; H, 0.59; F, 53.58; N, 3.68.

**N,N'-Bis(1H,1H-perfluoroheptyl)pyromellitic diimide (6-1-PyDI)** $^1$HNMR (400MHz, $CDCl_3$): 8.46(s, 2H), 4.44(t, 4H, $J$ = 15.2 Hz). Elemental analysis: Calcd for $C_{24}H_6F_{26}N_2O_4$, C, 32.75; H, 0.69; F, 56.11; N, 3.18. Found: C, 33.63; H, 0.52; F, 56.20; N, 3.15.

**N,N'-Bis(1H,1H-perfluorooxtyl)pyromellitic diimide (7-1-PyDI)** $^1$HNMR (400MHz, $CDCl_3$): 8.46(s, 2H), 4.45(t, 4H, $J$ = 15.2 Hz). Elemental analysis: Calcd for $C_{26}H_6F_{30}N_2O_4$, C, 31.86; H, 0.62; F, 58.14; N, 2.86. Found: C, 31.69; H, 0.41; F, 57.89; N, 2.90.

**N,N'-Bis(1H,1H-perfluorononyl)pyromellitic diimide (8-1-PyDI)** $^1$HNMR (400MHz, $CDCl_3$): 8.46(s, 2H), 4.45(t, 4H, $J$ = 15.2 Hz). Elemental analysis: Calcd for $C_{28}H_6F_{34}N_2O_4$, C, 31.13; H, 0.56; F, 59.79; N, 2.59. Found: C, 30.97; H, 0.51; F, 59.87; N, 2.67.

**N,N'-Bis(1H,1H-perfluoroundecanyl)pyromellitic diimide (10-1-PyDI)** $^1$HNMR (400MHz, $CDCl_3$): 8.46(s, 2H), 4.45(t, 4H, $J$ = 15.2 Hz). Elemental analysis: Calcd for $C_{32}H_6F_{42}N_2O_4$, C, 30.02; H, 0.47; F, 62.32; N, 2.19. Found: C, 30.28; H, 0.36; F, 62.09; N, 2.25.

**N,N'-Bis(3-(perfluoroctyl)propyl)pyromellitic diimide (8-3-PyDI)** Elemental analysis: Calcd for $C_{32}H_{14}F_{34}N_2O_4$, C, 33.82; H, 1.24; F, 56.84; N, 2.47. Found: C, 34.07; H, 1.14; F, 56.93; N, 2.50.

### Device Fabrication and Characterization

Heavily-doped silicon with 300 nm thermal oxide dielectric layer on top was coated with octadecyltrimethoxysilane (OTS) self-assembled monolayer. Thin-film transistors in top-contact/bottom-gate configuration were fabricated on the silicon substrate using thermally evaporated PyDIs (45nm) and gold (50nm) as the semiconducting layer and electrode, respectively. The channel widths were 6 mm, and the channel lengths were 250µm. Device characterization was performed using a Keithley 4200 Semiconductor Parameter Analyzer in a Janis Research ST-500-1 vacuum triaxial probe station. Mobility was calculated from the saturation regime and fitted in the regions of highest slope

.

# CHAPTER 3

## Enhancing the Electrical Performance of Pyromellitic Diimides

### 3.1 Introduction

There are two aspects to controlling the electrical performance of organic semiconducting materials. From the view point of device physics, the HOMO/LUMO levels of the organic molecules and relative energy levels between the interfaces can be adjusted by chemical synthesis to optimize the charge injection and charge transport efficiency.  On the other hand, the crystal structure, morphology, and molecular packing can be altered by different process methods and device schemes. The overall electrical performance is the interplay of these physics and process factors.

In Chapter 2, we established the correlation between the molecular structure and electrical performance for various pyromellitic diimides using a common testing platform. Based on the finding of the optimized side chain, we would like to further explore the potential of the pyromellitic core by examining the factors that determine the charge injection and transport, and to develop approaches for enhancing the electrical performance.

### 3.2 Introducing Hole Transporting Layer and Other Self-Assembled Monolayer at the Dielectric/Organic Interface

The interface between the gate dielectric and organic semiconducting layer is a major factor that determines the overall electronic performance, and there are various ways of modifying/improving the interface properties. Self-assembled monolayers (SAMs) with different HOMO/LUMO levels and dipoles can shift the work function of metals and the electron affinity of semiconductors. They are generally used to change the conduction barrier, reduce gate leakage current, and minimize trapping state density at the interface for maximizing charge injection efficiency.[30] When surface electron traps by the hydroxyl group at the interface were eliminated by using a hydroxyl-free gate dielectic, not only were the higher electron mobilities obtained from n-type semiconductors, but also n-type operation was uncovered from the materials that previously only showed p-type activities.[31]

It has been shown that an electronically active hetero layer can be used to improve the mobility of n-type semiconductors. N,N′-Di-[(1-naphthyl)-N,N′-diphenyl]-1,1′-biphenyl)-4,4′-diamine (NPD), a commonly used hole transporting material for OLED devices, was introduced between the $SiO_2$ gate dielectric and organic semiconductor.[32] For PTCDI with octyl side chains as the organic semiconductor, the mobility from NPD interlayer (0.11cm$^2$/Vs) was three times higher than that of bare $SiO_2$ (0.035 cm$^2$/Vs) and two times higher than that of HMDS (0.069 cm$^2$/Vs). For $C_{60}$ as the organic semiconductor, the NPD interlayer resulted in much higher mobility (1.8 cm$^2$/Vs) than that of bare $SiO_2$ (0.0075 cm$^2$/Vs), OTS (0.50 cm$^2$/Vs), and HMDS (0.80 cm$^2$/Vs). From XRD and AFM analysis results, it was concluded that the mobility improvement did not result from structural or morphological change of the semiconducting layer, but were attributed to electron donating character of the hole transporting interlayer NPD that filled the deep electron traps of the organic semiconductors, as illustrated in Figure 3-1.

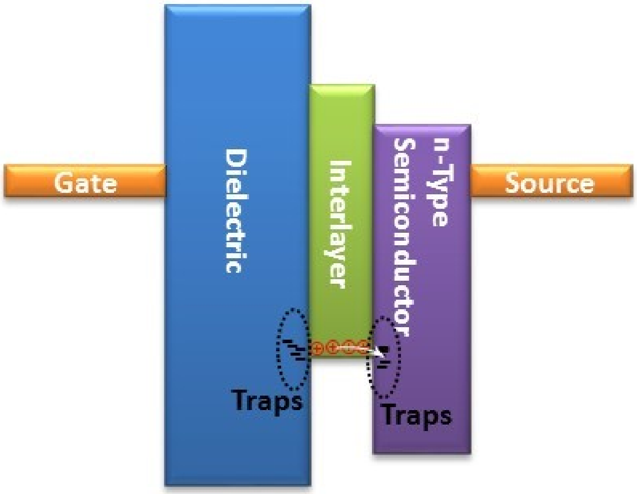

**Figure 3-1 Schematic relationship of energy levels in the hetero-layered structures with a hole transporting interlayer between dielectric and n-type semoconductor.**

To examine this concept, we introduce this 10nm NPD interlayer to the pyromellitic diimide with the optimized side chain (4-1-PyDI). The transistor output curve of 4-1-PyDI with NPD interlayer and the mobility comparison from different conditions were shown in Figure 3-2. Although giving tightly distributed mobilities, the NPD interlayer did not result in higher average mobility, and the mobility (0.19 cm$^2$/Vs) was slightly lower than that of OTS surface treatment (0.26 cm$^2$/Vs).

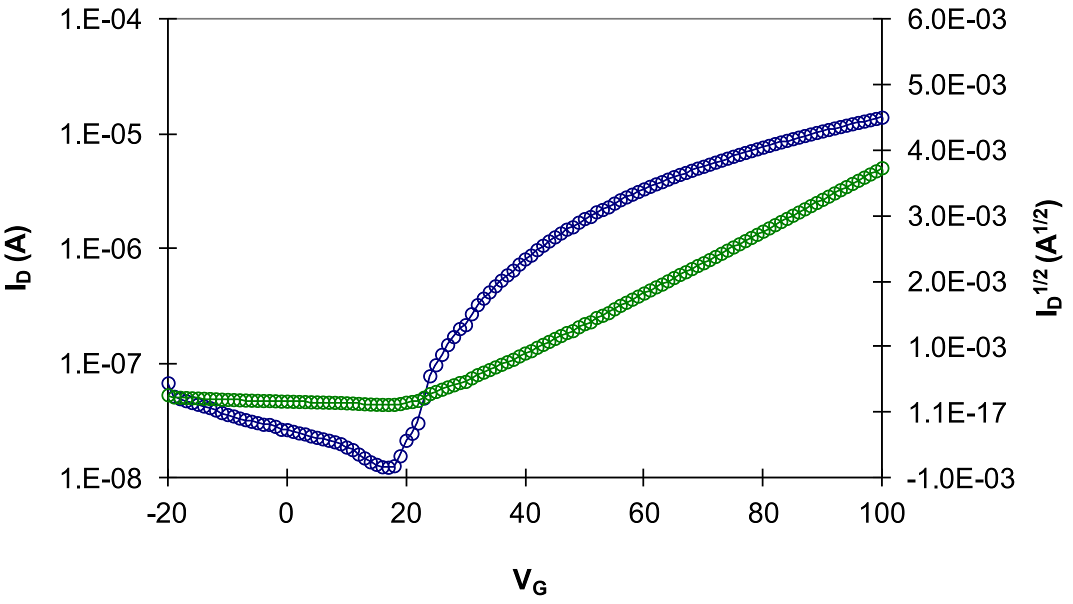

**Figure 3-2 Transistor transfer curve of 4-1-PyDI with NPD interlayer**

The possible reason was revealed from the structural study of 4-1-PyDI with NPD interlayer and surface treatment of octadecyltrimethoxysilane (OTS), 1H,1H,2H,2H-perfluoro-octyltriethoxysilane (FOTS), and octadecyltrichlorosilane (Cl-OTS). From the XRD peaks in Figure 3-3, OTS gave the most crystalline 4-1-PyDI film. The intensities of first-order diffraction peak at 2θ =8.0° come in the order of OTS > Cl-OTS > NPD > FOTS. Without offering the benefit of filling deep electron traps, the NPD slightly decreased the crystallinity of surface-sensitive 4-1-PyDI. The result also confirmed that OTS is the optimized surface treatment among methods chosen for pyromellitic diimides.

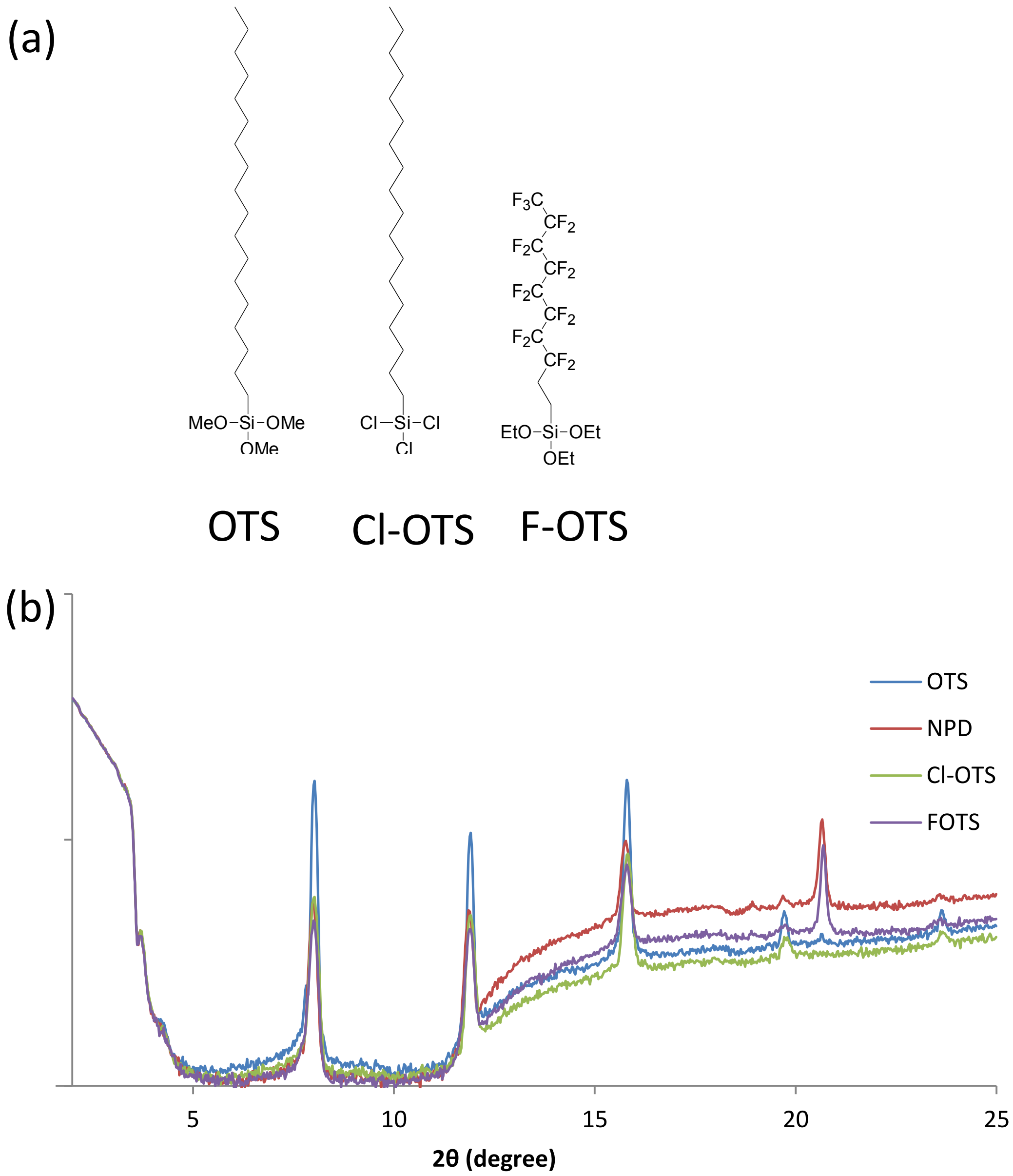

**Figure 3-3 (a) Chemical structures of the surface treatment molecules; (b)XRD spectrum of 4-1-PyDI with NPD interlayer and different surface treatments**

## 3.3 Enhancing the Process Window of Substrate Temperature

While we have shown in Chapter 2 that short fluoroalkyl side chains provide better packing and enable higher mobility, the easy volatilization from the heated substrate surface under high vacuum limits substrate temperature during deposition. For 4-1-PyDI, the highest allowable substrate temperature is 35$^0$C. Poor film uniformity or desorbed film were observed when the substrate was heated above 40$^0$C. Similarly, the low mobility of 8-3-PyDI at 90$^0$C cannot be enhanced at higher temperature. No films were obtained on 120$^0$C substrates.

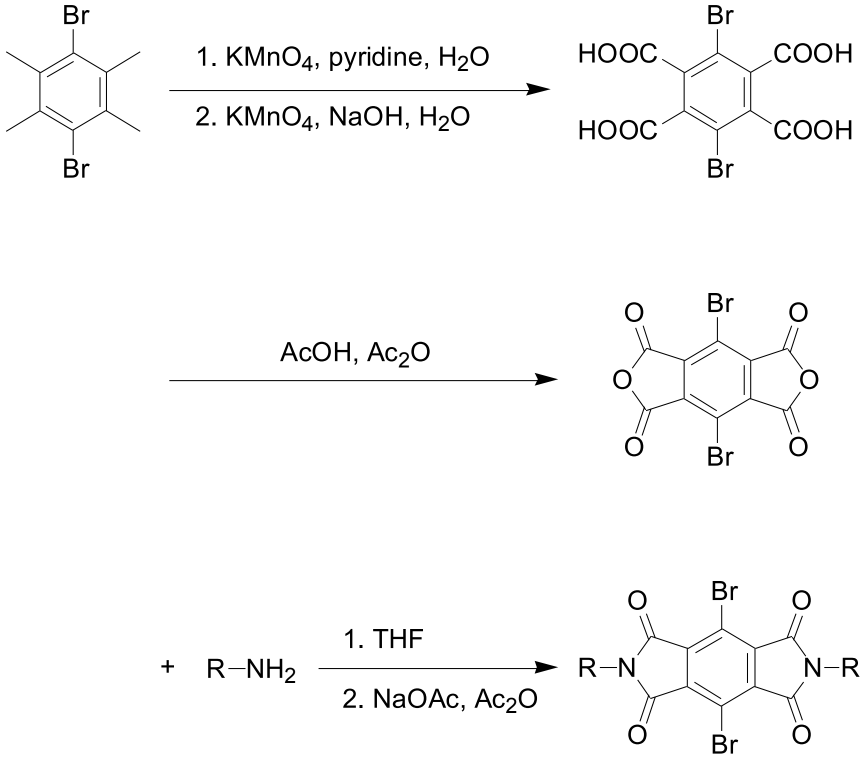

R = $CH_2C_4F_9$ **Br2-4-1-PyDI**

**Figure 3-4 Structures and preparation of Br2-4-1-PyDI**

To further explore the potential of short fluoroalkyl side chains, we took the optimal perfluorobutylmethyl (4-1) side chain and put it on core-brominated pyromellitic diimide via two-step condensation from precursor core-brominated pyromellitic dianhydride as depicted in Figure 3-4. Br2-4-1-PyDI has a much higher melting point relative to 4-1-PyDI (Figure 3-5). This $120^0$C increase in melting point indicates the possibility of keeping the film on the substrate at elevated temperature.

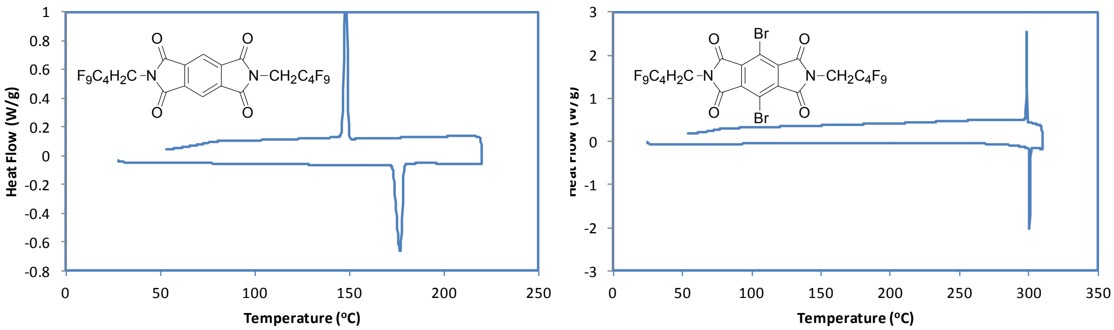

**Figure 3-5 DSC Thermograms of 4-1-PyDI and Br2-4-1-PyDI (exothermic up)**

### *3.3.1 Materials, Thermal Properties and Molecular Energy Levels of Br2-4-1-PyDI*

The high melting point of Br2-4-1-PyDI indicates higher sublimation temperature may be need for vapor deposition. The thermal stability of the material is examined by sequential running DSC of the same sample reaching an increasing highest temperature range from 280°C to 350°C. As shown in Figure 3-6, the compound is thermally stable up till 330°C and degrades when heating to 350°C. During purification by sublimation under vacuum, yellowish powers were obtained 188°C and 208°C, indicating high purity from tight temperature range and also the processability of vapor deposition at a temperature below the degradation temperature.

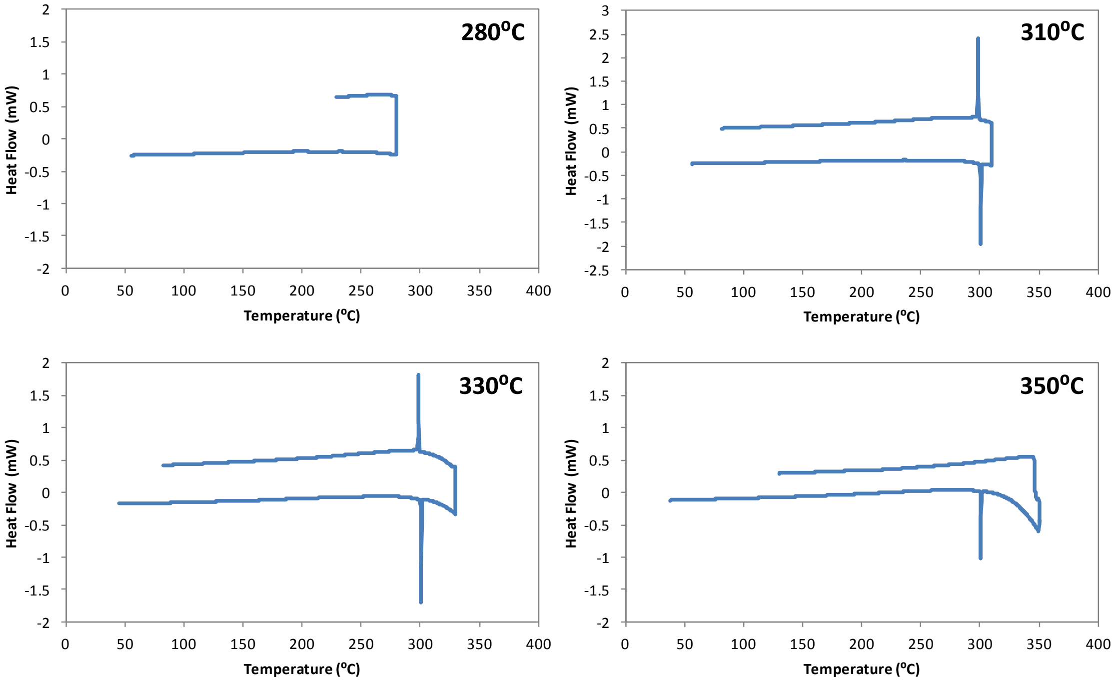

**Figure 3-6 DSC of Br2-4-1-PyDI at different temperature range**

From the cyclic voltammograms in Figure 3-7, bromo substituents makes the compound about 0.2 V easier to reduce, indicating a slightly deeper LUMO energy level of -4.4eV that helps ambient stability by alleviating the effect of oxygen or water.[28]

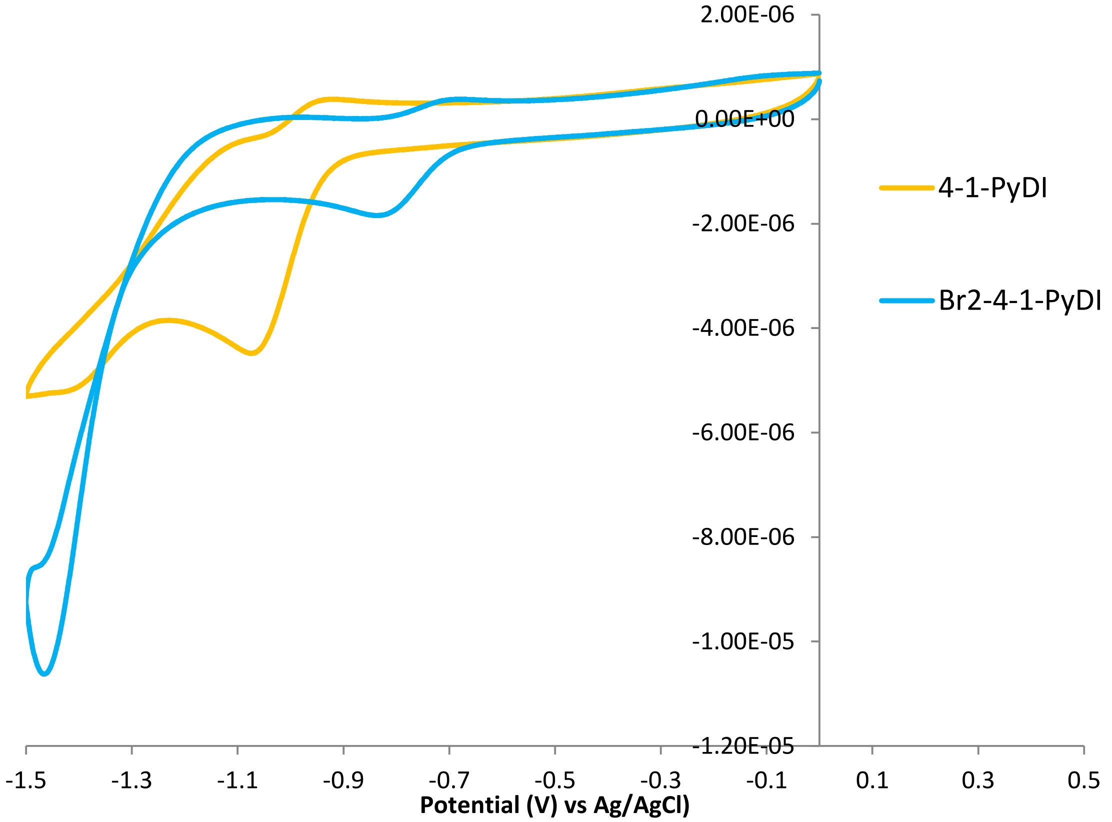

**Figure 3-7 Cyclic voltammograms of 4-1-PyDI and Br2-4-1-PyDI**

The UV spectrum of Br2-4-1-PyDI (Figure 3-8) shows a 50nm increase in wavelength as compared to 4-1-PyDI. The onset of 390nm still stands outside the lower end of the visible light spectrum and retains transparency in the visible range.

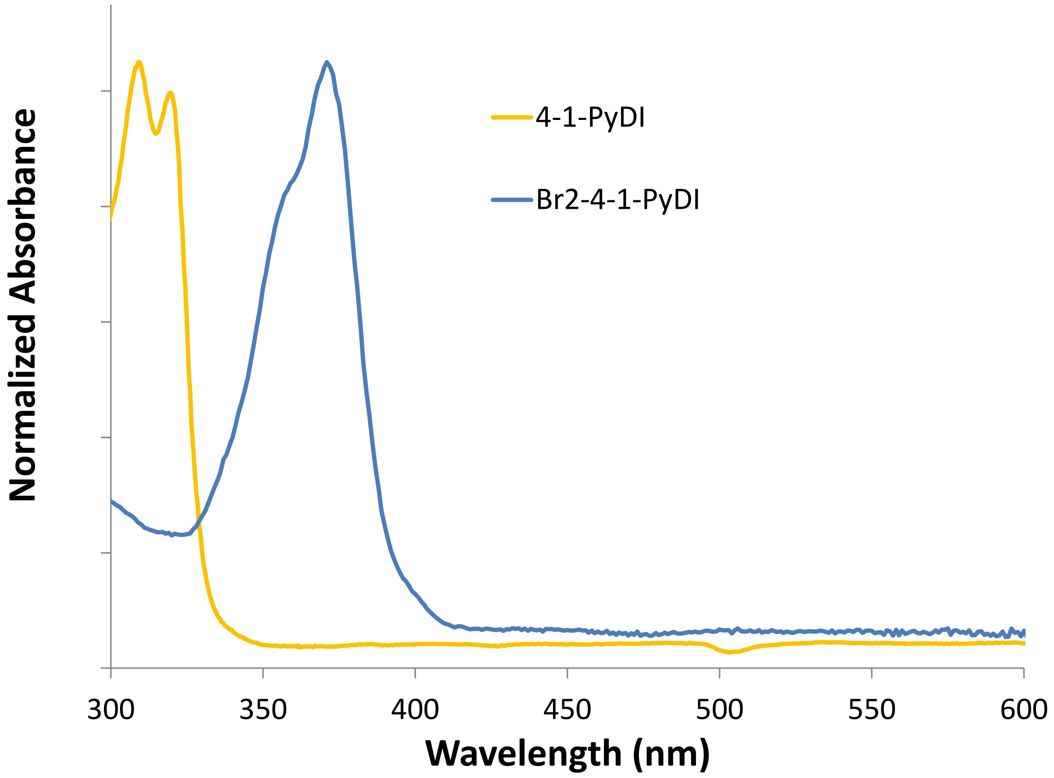

**Figure 3-8 UV-Vis Spectra of the PyDI derivatives**

### *3.3.2 Thin Film Stacking*

The thin film structures of Br2-4-1-PyDIs were studied by X-ray diffraction (XRD) for thin film vacuum-deposited on Si/SiO2 substrates with previously optimized OTS surface treatment. Its thin film XRD (Figure 3-9) reveals highly ordered micro-structure, with d-spacing (20.3Å) close to the calculated molecular length (20.6Å), suggesting the molecules are aligned almost perpendicular to the substrate surface and form layer structures that favor the π–π stacking in the horizontal direction, which would also be the charge transport direction.

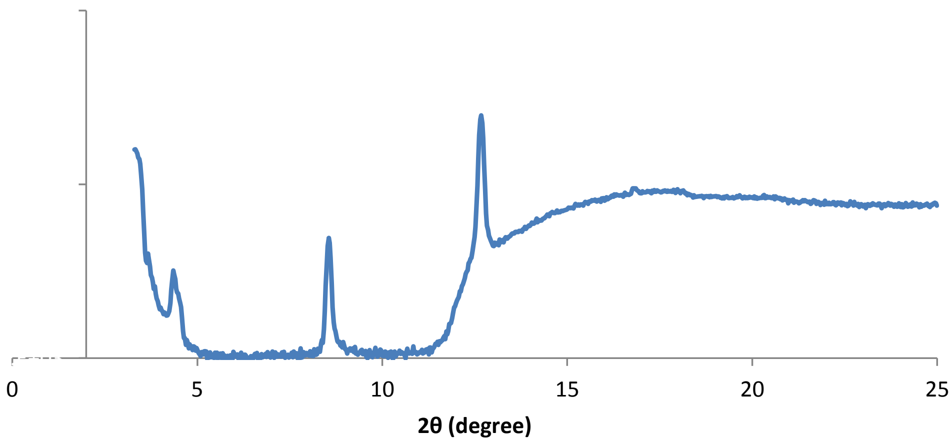

**Figure 3-9 X-ray Diffraction for thin films of Br2-4-1-PyDI**

*3.3.3 Fabrication and Characterization of Thin-Film Transistors*

Thin-film transistors in top-contact/bottom-gate (TCBG) configuration were fabricated using thermally evaporated PyDIs and gold as the semiconducting layer and electrode, respectively, on heavily-doped silicon with 300 nm thermal oxide dielectric layer. As shown in Figure 3-10, when depositing at 60°C the Br2-1-PyDI gives mobility of 0.02 $cm^2/Vs$. The film deposited at 75°C gives an exceptional mobility of 0.2 $cm^2/Vs$, the highest PyDI mobility yet reported and almost ten times higher than core-nonfunctionalized 4-1-PyDI. Br2-4-1-PyDI films made at $80^0C$ exhibit slightly lower mobility, 0.08 $cm^2/Vs$, still four times that of 4-1-PyDI.

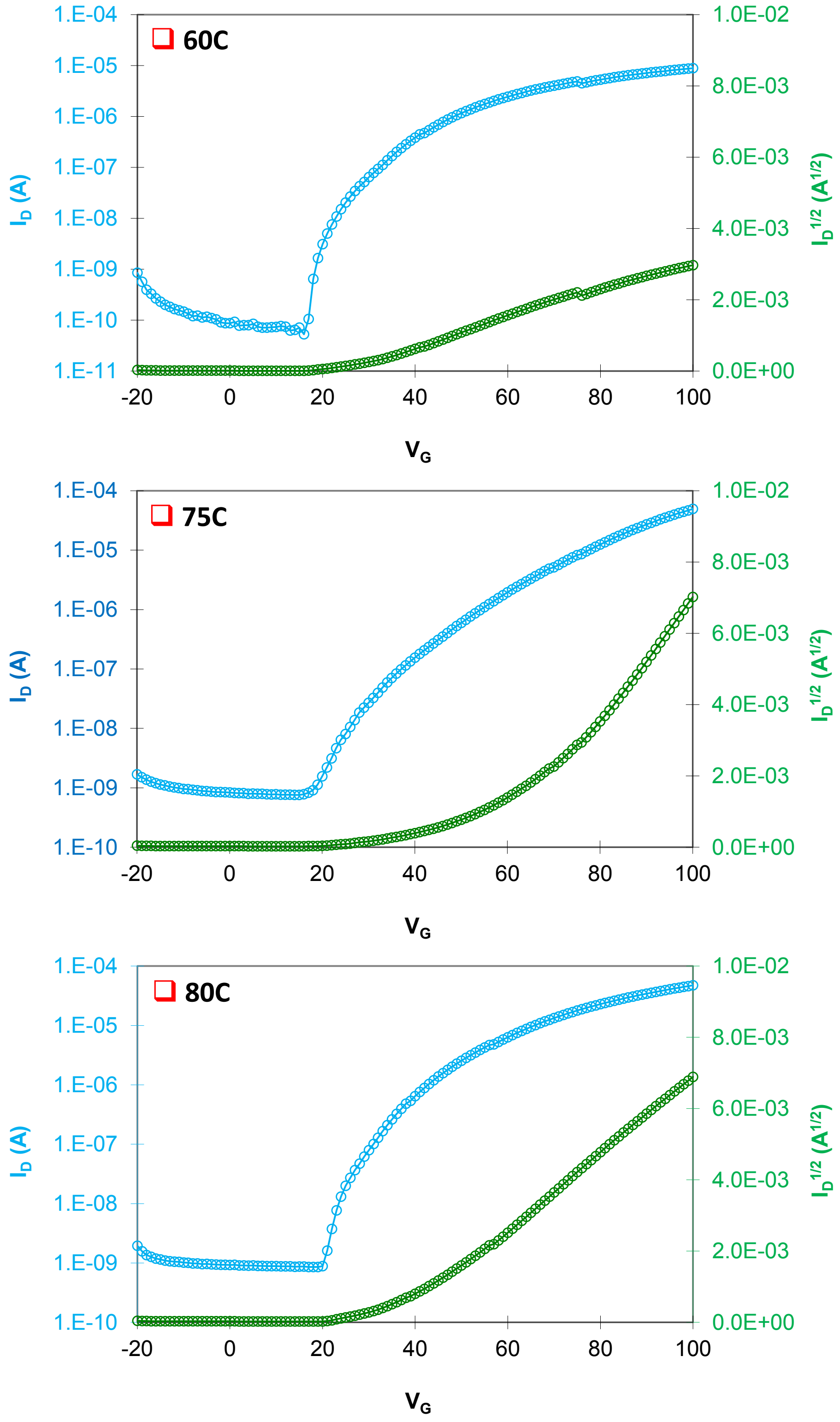

**Figure 3-10 Transistor transfer curves of Br2-4-1-PyDI at different substrate temperature**

Although core-brominated arylenediimides has been reported on larger arylene cores,[32] they are generally used for synthesizing core-functionalized arylenes[33], core-expanded arylenes[34] and arylene-based polymers[35]; rarely are they used directly as semiconducting materials. In the case of PTCDI, a brominated core did not give higher mobility than non-functionalized cores. Instead, dibrominated PTCDI showed similar mobility (with perfluoropropylmethyl imide substituents) or lower mobility (with octyl imide substituents).[33] Tetrabrominated PTCDI with perfluoropropylmethyl imide substituents exhibited a much lower mobility.[36]

### *3.3.4 Single Crystal of Br2-4-1-PyDI*

Br2-4-1-PyDI single crystals were grown by loading source material in a 5-inch long inner quartz tube (16 mm inner diameter/18 mm outer diameter) that was then put into an-other long outer quartz tube. All the tubes were pre-cleaned with HPLC grade acetone. The source was heated at 300°C for 3 hours in a flow of 99.999% pure He at 100 $cm^3$/min.

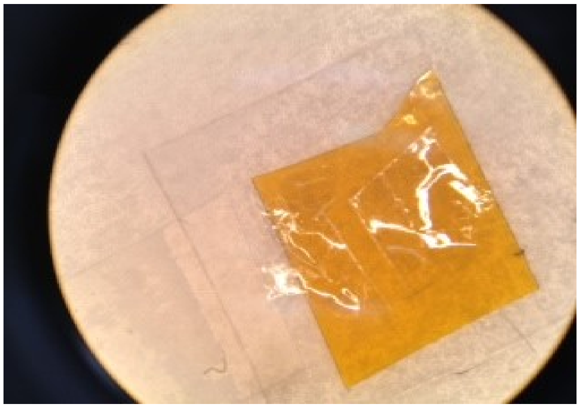

**Figure 3-11 Vapor growth single crystal of Br2-4-1-PyDI**

The vapor grown single crystals are thin flat platelets with smooth facets as shown in Figure 3-11. Based on X-ray diffraction analysis, the normal to these large facets is the a* direction, e.g., the platelet surface is the 100 plane. The room temperature (RT) cell is a = 44.0, b = 6.99, c = 18.0 Angstroms, beta = 104.1, volume = 5350, compared to the 100K cell of a = 41.2, b = 6.94, c = 18.1 Angstroms, beta = 104.6, volume = 5002. Thus, the b- and c-axes appear to expand by about the expected 1% for organic molecular crystals on going from 100K to room temperature. The a-axis value at room temperature has lower precision, but still appears expanded by over 6%, which is significantly anisotropic. At RT (vs 100K), the background is higher and the Bragg intensities are lower and extend to a lower resolution, consistent with the significant disorder of the molecule. The structural model for Br2-4-1-PyDI contains disorder of both aliphatic chains, which is well modeled ($R < 6\%$). The structure further confirms that the molecules are aligned almost perpendicular to the 100 facet, with an a-axis length of 44 Å for two molecules, slightly slipped cofacial packing (Figure 3-12), and an interplanar $\pi$-$\pi$ staking distance of 3.21 Å, as shown in Figure 3-13. The fluoroalkyl side chains adopt a *trans* configuration, enabling close packing of neighboring molecules. In contrast, a core-unsubstituted PyDI with tetradecyl side chains shows a large herringbone angle in its single crystal (Figure 3-14).[37]

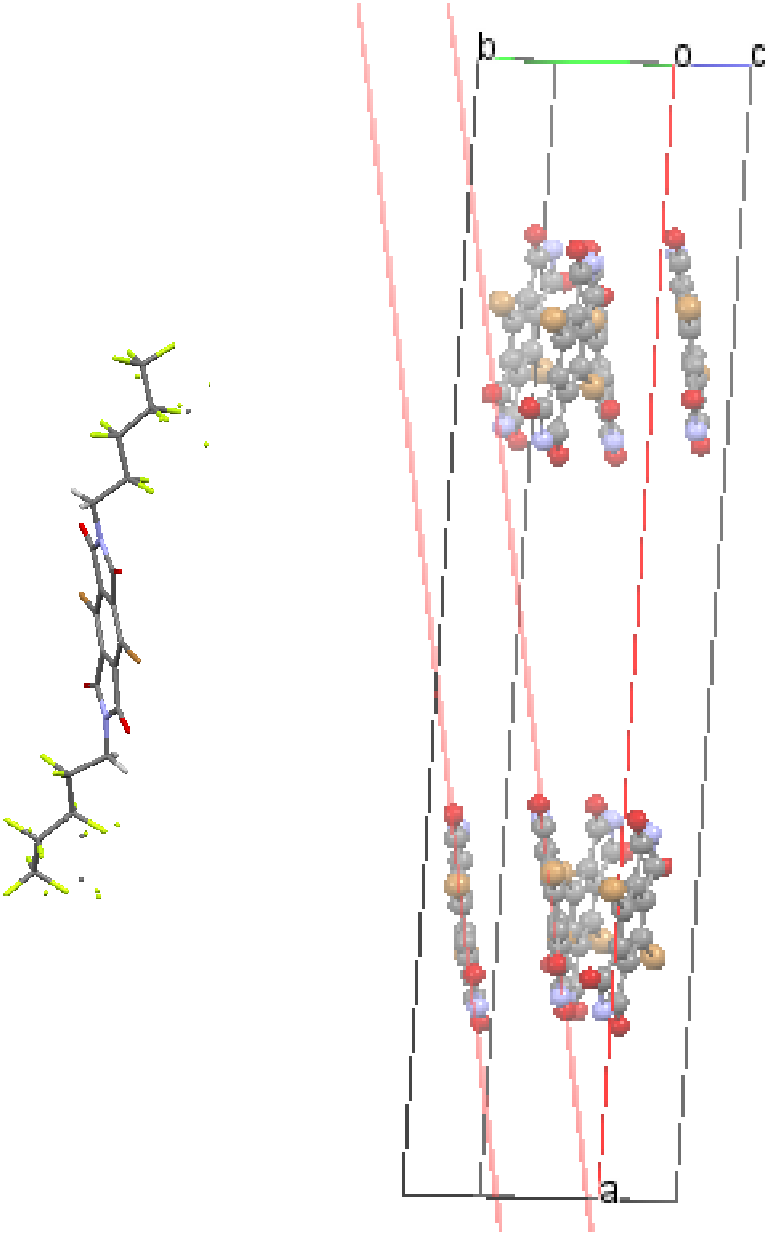

**Figure 3-12 Crystal structure of Br2-4-1-PyDI showing the *trans* configuration and slipped cofacial packing**

**Imide substituents in the packing figure are omitted for easy viewing.**

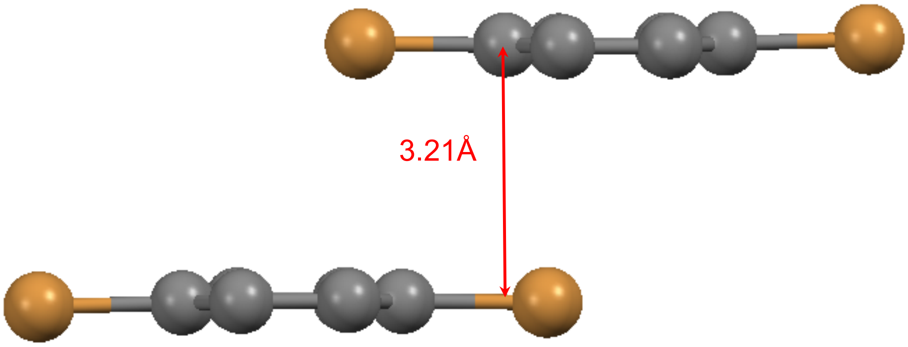

**Figure 3-13 The alignment of Br2-4-1-PyDI molecules and the interplane distance**

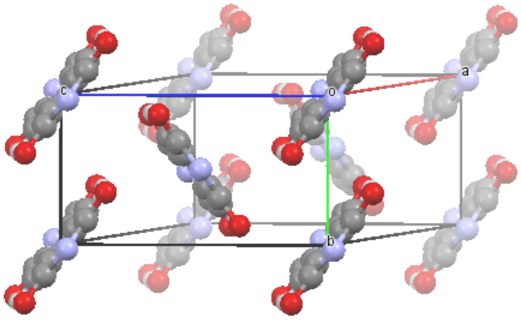

**Figure 3-14 Crystal structure of core-unsubstituted PyDI with tetradecyl side chains holing a herringbone arrangement.**

**Crystal structure data obtained from reference 37.**

### *3.3.5 Air stability and sensing*

The highly crystalline structure in the thin film of Br2-4-1-PyDI also enables air operability and stability. The slightly deeper LUMO energy level is also beneficial to the ambient stability. As demonstrated in Figure 3-15, the transistors exhibit mobility of 0.018 cm$^2$/Vs in air and retain mobility of 0.013 cm$^2$/Vs after six months.

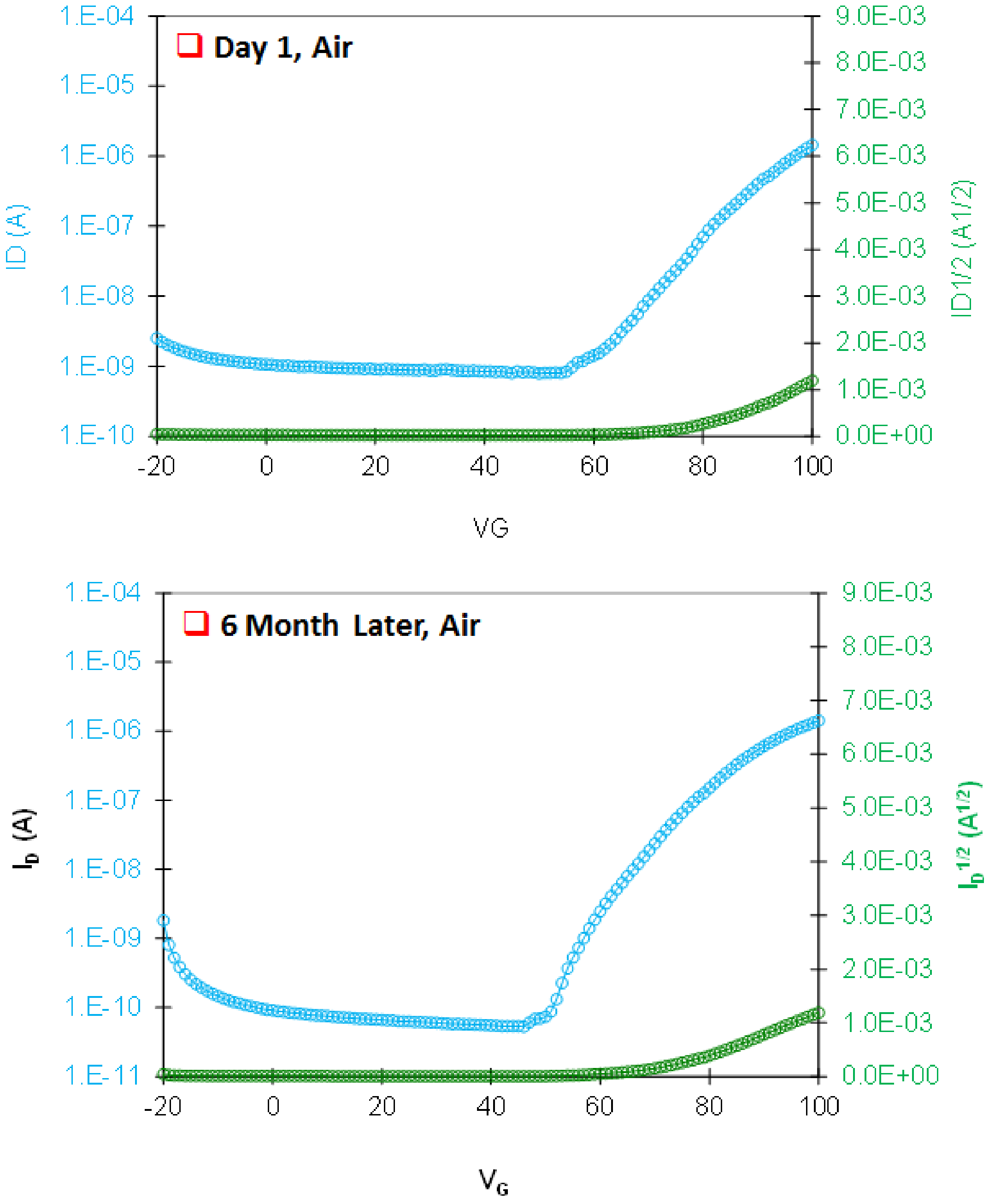

**Figure 3-15 Transistor transfer curves of Br2-4-1-PyDI measured in air: day 1 and after six months**

Br2-4-1-PyDI also has good sensing response to amine. As depicted in Figure 3-16, upon exposing to triethylamine, the output current decreased in corresponding to the addition of triethylamine. Furthermore, the sensing response is reversible. After turning on the turbo pump to remove the triethylamine vapor, the device was fully recovered.

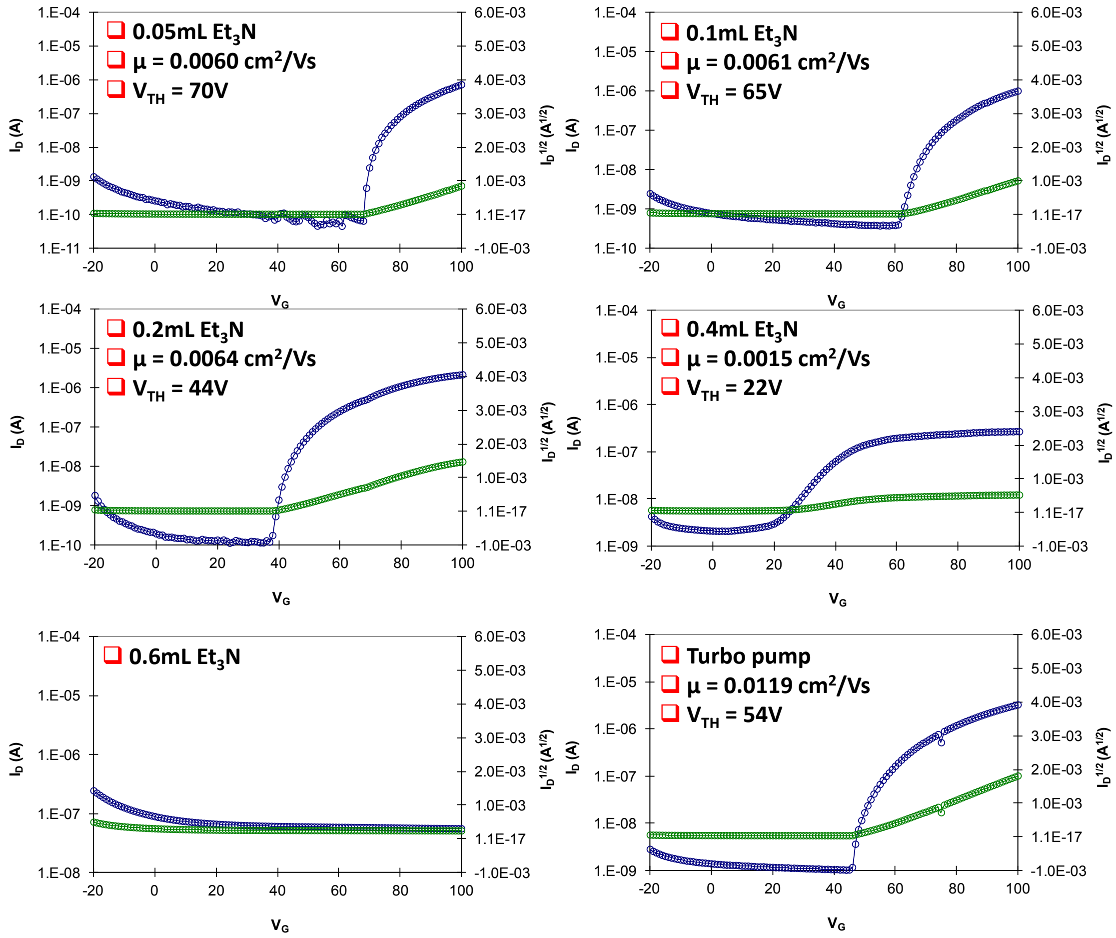

**Figure 3-16 Transistor transfer curves of Br2-4-1-PyDI exposing to different amount of triethylamine in a sealed chamber**

## 3.4 PyDI-Based Solution-processable Homopolymer

Core-brominated PyDI is also a useful building block for PyDI-based polymers. For example, 3,6-dibromo PyDI with octyl side chain underwent Stille coupling reaction with bis(tributylstannyl)acetylene to give a homopolymer[29], as shown in Figure 3-17.

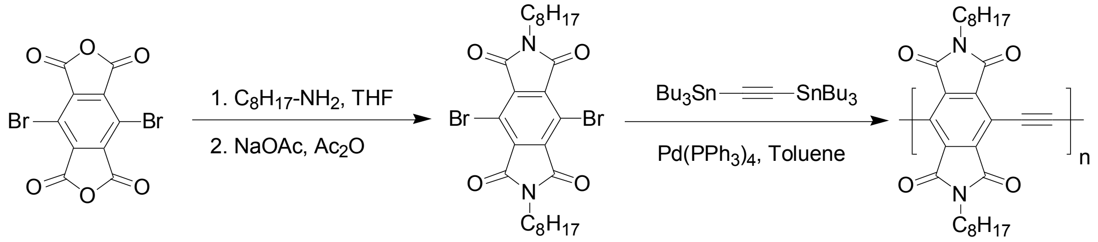

**Figure 3-17 Synthesis of PyDI-based polymer from dibromo PyDI**

This PyDI-based polymer, with a long alkyl side chain, can be solution processed to make thin films for transistors. Although the devices with bottom-gate top-contact geometry did show some transistor behavior, the device worked best in a top-gate bottom-contact geometry using spin-coated CTYOP as the dielectric, and aluminum as the gate electrode. Interdigitated gold electrodes with channel length of 50μm and channel width of 8100 μm ensured short charge carrier traveling distance and higher current level can be achieved. Because polymer synthesis and device fabrication were carried out in ambient environment, addition thermal annealing at 100°C (below the glass transition temperature of CYTOP, 108°C) under vacuum after the device fabrication helped removing the traps in the device. Some enhancement can be observed after a three-hour annealing, and good device performance, as shown in Figure 3-18, was obtained after a twelve-hour annealing. The annealed device showed minimal hysteresis in the on-regime.

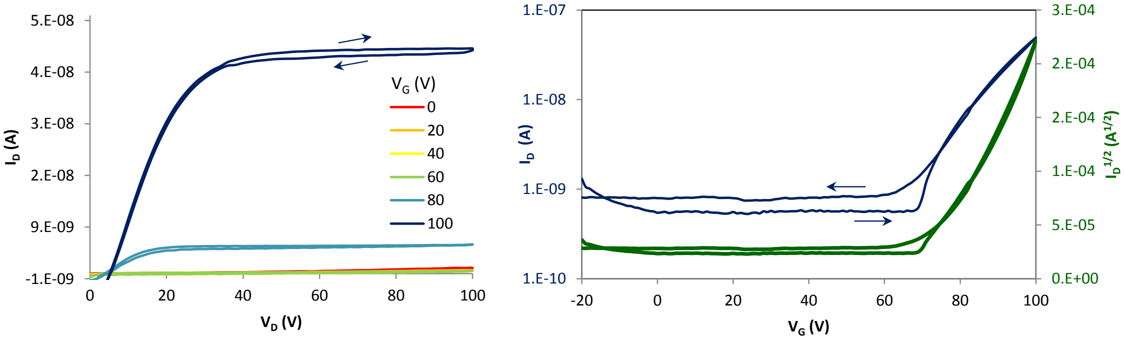

**Figure 3-18 Output curve and transfer curve of transistor made from PyDI-based polymer**

## 3.5 Conclusions

Based on what we learn from the systematic comparison of different side chains in Chapter 2, we developed different approaches to explore the potential of the pyromellitic core and further enhance its electrical performance. Attaching the optimized side chain to 3,6-dibromo PyDI allowed nearly parallel PyDI cores and an exceptional mobility of 0.2 cm$^2$/Vs, the highest PyDI mobility yet reported. The closed-packed thin film also exhibited good air stability after six months

## 3.6 Experimental Section

### General

$^1$H NMR spectra were recorded with a Bruker Avance 400 MHz spectrometer. Elemental analyses were performed by Atlantic Mircolab (Norcross, Georgia). DSC measurements were carried out with a TA Instruments DSC Q20 at a heating and cooling rate of 5 °C/min under a nitrogen atmosphere. The electrochemical measurements were carried out in dichloromethane solutions under nitrogen with 0.1M tetrabutylammonium hexafluorophosphate ($NBu_4PF_6$) as the supporting electrolyte at room temperature using an Aautolab PGSTAT 302 potentiostat/galvanostat. The cyclic voltammograms were obtained at a scan rate of 100 mV/s. A platinum disk and platinum wire were used as the working and counter electrode, respectively; and $Ag/Ag^+$ (0.01M $AgNO_3$) was used as the reference electrode. UV−vis absorption spectra were collected in dichloromethane solutions using a Varian Cary 50 Bio UV-Vis spectrophotometer. X-ray diffraction scans were acquired in the Bragg-Brentano (θ-2θ) geometry using a Phillips X-pert Pro X-ray diffraction system. Scan step size was 0.02° and time per step was 2 seconds.

**N,N'-bis(1H,1H-perfluoropentyl)-3,6-dibromopyromellitic diimide (Br2-4-1-PyDI)**

1H,1H-perfluoropentyl amine (1.59g) was added into a solution of 3,6-diibromopyromellitic dianhydride[38] (0.8g) in dry THF (20mL) under nitrogen environment. The mixture was stirred at room temperature overnight. After removing the solvent under reduced pressure, anhydrous sodium acetate (0.70g) and acetic anhydride (15mL) were added. The mixture was heated at $100^0$C under nitrogen for 3 hours. After pouring ice water, the precipitate was collected by filtration (1.55g, 87%) and purified by sublimation under high vacuum. $^1$HNMR (400MHz, $CDCl_3$): 4.44(t, 4H, $J$ = 15.2 Hz). Elemental analysis: Calcd for $C_{20}H_4F_{18}N_2O_4Br_2$, C, 28.66; H, 0.48; F, 40.81; N, 3.34. Found: C, 28.75; H, 0.30; F, 40.91; N, 3.44.

**Device Fabrication and Characterization.**

Heavily-doped silicon with 300 nm thermal oxide dielectric layer on top was coated with different self-assembled monolayer. Thin-film transistors in top-contact/bottom-gate configuration were fabricated on the silicon substrate using thermally evaporated PyDIs (45nm) and gold (50nm) as the semiconducting layer and electrode, respectively. The channel widths were 6 mm, and the channel lengths were 250µm. Device characterization was performed using a Keithley 4200 Semiconductor Parameter Analyzer in a Janis Research ST-500-1 vacuum triaxial probe station. Mobility was calculated from the saturation regime and fitted in the regions of highest slope.

For PyDI-based polymer, heavily-doped silicon with 300 nm thermal oxide was used as the substrate, and interdigitated (channel length of 50µm and channel width of 8100 µm) gold electrodes (30nm) with a thin underlying chromium adhesive layer (3nm) were thermally evaporated using pre-patterned photoresist as the shadow mask. The polymer was spin-coated from 10mg/mL solution in toluene at 1000RPM for 60 seconds and then annealed at 150°C for 10 minutes. After cooling with mild nitrogen flow, CYTOP dielectric was spin-coated from a 1:1 mixture of a mixture of CYTOP CTL-809M and CT-solv 180 at 1000RM for 60 seconds, and then annealed at 100°C for 15 minutes. 15nm tetratetracontane was thermally evaporated on top of CYTOP, and then small pad of 100nm aluminum electrode was thermally evaporated as the gate electrode. The fabricated device was further annealed at 100°C under vacuum for 12 hours. Device characterization was performed using a Keithley 4200 Semiconductor Parameter Analyzer in a Janis Research ST-500-1 vacuum triaxial probe station.

# CHAPTER 4

## Crystal Engineering and Device Scheme Optimization for Oligosilane Conductivity Measurements

### 4.1 Introduction

While π-bond conjugation systems are by far the most studied and developed materials in organic molecular electronics, spectral evidence[39,40] on saturated oligosilanes indicates the possibility of electron transfer behavior similar to that of conjugated carbon-based materials. Polysilanes, having electrons delocalized along the Si backbone, were intensively investigated for their hole transporting behavior.[41,42] These studies have suggested σ-bond conjugation systems as a new type of charge carrier transporting materials.[43]

Recently, conductance through a single small oligosilane chain was explored computationally,[44] and the compound synthesized experimentally and characterized electrically.[45] Using a scanning tunneling microscope-based break-junction (STM-BJ) technique,[46-48] single-molecule conductances were measured and found to decrease slowly with increasing chain length with a decay constant considerably less than that of the corresponding alkanes and comparable to that of π-bond conjugated polyacetylene fragments.

For this thesis, in order to extend the finding from molecular scale to bulk devices and explore the feasibility of using them as organic electronic materials, oligosilanes with S-Me (**Si-4-SMe**) and ethyl cyanoacrylate terminal groups (**Si-n-OC1** and **Si-n-OC6**), as shown in Figure 4-1, were investigated for their crystal growth at different process conditions and their bulk conduction properties in the solid state. We began with **Si-4-SMe,** and later stated using **Si-n-OC1** and **Si-n-OC6** that were designed for enhanced charge transfer ability and better alignment.

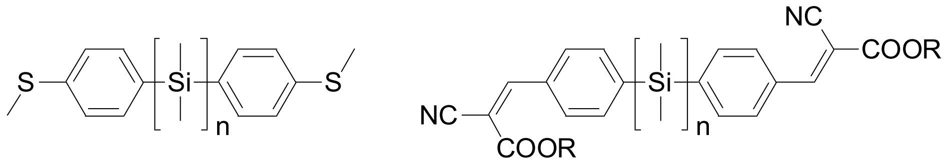

**Si-n-SMe**

**Si-n-OC1** R = $CH_3$

**Si-n-OC6** R = $C_6H_{12}$

**Figure 4-1 Structures of two series of oligosilanes**

**Si-n-SMe and Si-n-OCx. n is the length of silicon backbone, and x is the length of alkyl group of the terminal ester moiety**

## 4.2 Thin Film Growth and Crystal Structure Analysis

### *4.2.1 Spin-coating from different solvents with varied rotation speeds*

The oligosilanes have high solubilities in common organic solvents, including chloroform, acetonitrile, toluene, chlorobenzene, and dichlorobenzene. Spin-coating of **Si-4-SMe** onto $SiO_2$/Si substrates results in various forms of films, depending on the solvent used. As shown in Figure 4-2, chlorobenzene gave rough films near the edge of the substrates. Acetonitrile yielded radial patterns at high rotation speed (2000RPM) and small crystalline patterns at low rotation speed (500RPM). Dichlorobenzene resulted in continuous films, though not uniform, covering most of the substrate surface.

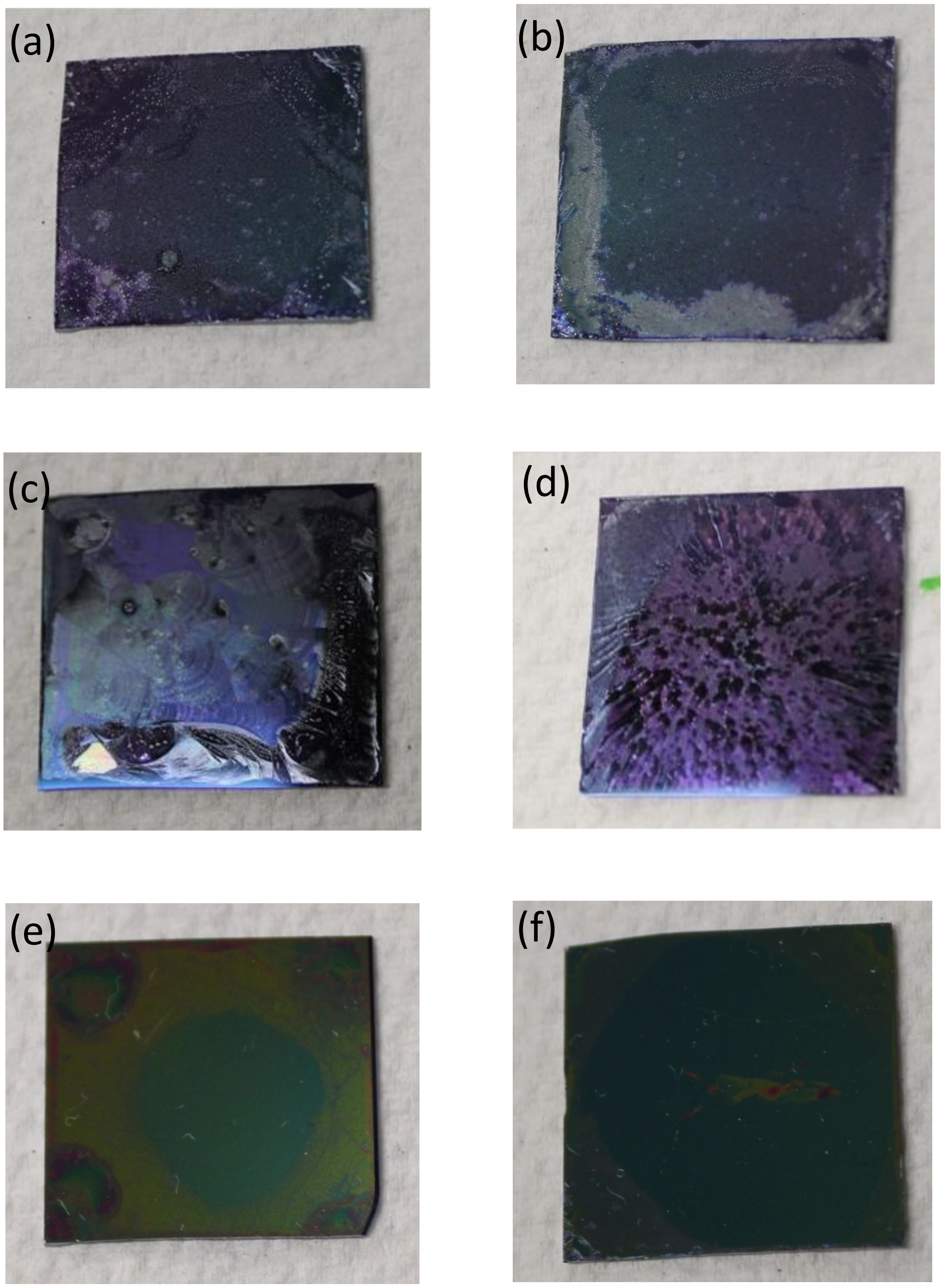

**Figure 4-2 Spin-coating thin films of Si-4-SMe**

**(a)chlorobenzene, 500RPM; (b)chlorobenzene. 1000RPM; (c)acetonitrile, 500RPM; (d)acetonitrile, 2000RPM; (e)dichlorobenzene, 500RPM; (f)dichlorobenzene, 1000RPM**

XRD analysis of the thin film made from dichlorobenzene (Figure 4-3) indicated the same crystalline structure for both 500RPM and 100RPM films, with a diffraction peak corresponding to the interlayer spacing of 6.8Å.

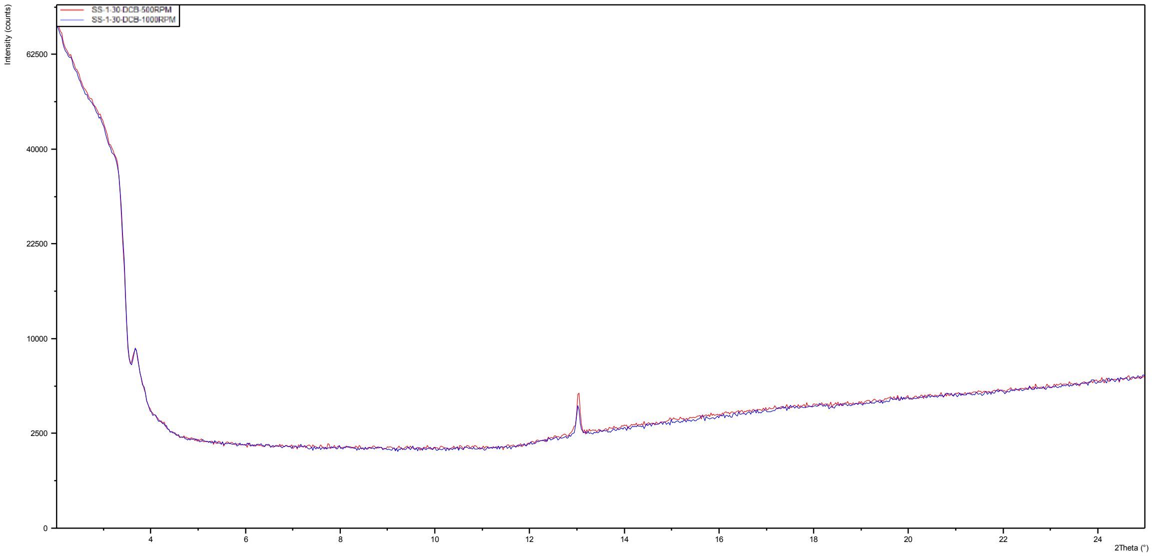

**Figure 4-3 XRD spectrums of Si-4-SMe thin films made from with dichlorobenzene with spin-coating rotation speed of 500RPM and 1000RPM**

### *4.2.2 Drop-casting films and devices*

While spin-coating film from dichlorobenzene with both 500RPM and 1000RPM rotation speed gave crystalline films, 500RPM resulted in higher XRD peak intensity and better surface coverage on the substrate. Since lower rotation speed seemed to be beneficial to thin film formation for this material, and 500RPM is approaching the lower limit of the spin coater, this finding encouraged us to further investigate the thin film growth using the drop casting method.

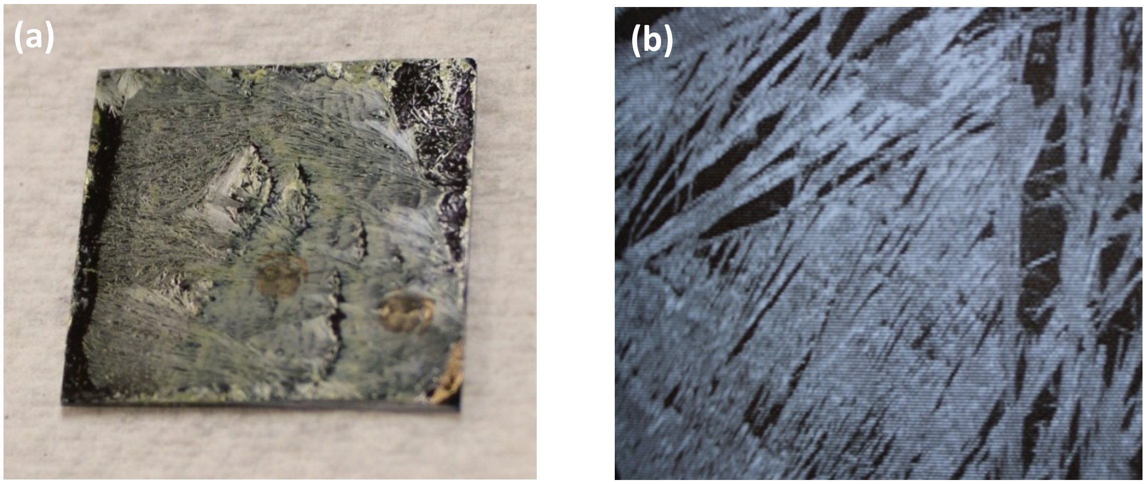

**Figure 4-4 Drop-casting thin film and device of Si-4-SMe. The golden dot is the electrodes made from gold using TEM grid as shadow mask**

Thin films made by drop-casting from dichlorobenzene indeed gave very good coverage over the entire surface, as shown in Figure 4-4. In addition, needle-shaped crystals can be seen by the naked eye and further confirmed under the optical microscope.

The efforts in making thin film transistors using drop-casting films did not result in satisfactory working field-effect transistors. The highly crystalline but rough surface made electrical contact from the top a challenge. At some spots the gold electrode pads stood directly on the $SiO_2$ dielectric surface, making it difficult to distinguish the actual currents from the gate leakage currents.

## 4.3 Crystal Engineering and Conductivity Measurements from Different Device Dimensions

To obtain the accurate conductivity measurement from the current that actually flows though the oligosilanes without the interference of gate leakage currents, two-terminal deices made on glass slides were used instead of three-terminal transistors made on $SiO_2/Si$ substrates. A bottom contact device scheme was also used to overcome the surface roughness of oligosilane thin films.

### *4.3.1 Direct drop casting on glass slides*

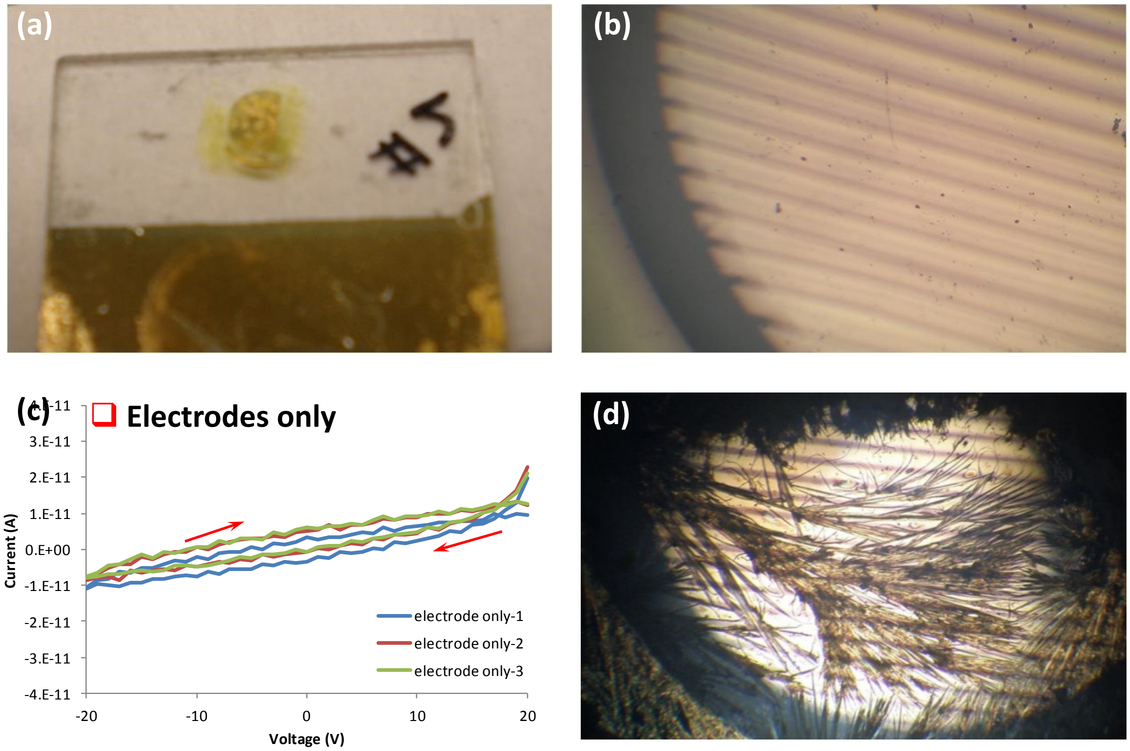

**Figure 4-5 Drop cast Si-4-OC1 onto glass slide pre-patterned with gold electrodes Gold stripe width = 63µm. Spacing between gold stripes = 25µm**

As the same time, a new group of oligosilane became available. Oligosilanes **Si-4-OC1** with ethyl cyanoacrylate terminal groups, designed to enhance intramolecular charge transfer, were drop-casted onto glass substrates pre-patterned with gold using TEM grids as shadow mask. As shown in Figure 4-5(b), the width of gold stripes is 63μm, and the spacing between them is 25μm. The blank current was measured before drop casting to ensure no electric contact between the densely aligned gold electrodes. The measured current (~1 x $10^{-11}$A) is approximately the background current that the instrument can detect, confirming the good isolation between electrodes.

Although the surface conditions on glass slides and gold electrodes were different from $SiO_2$/Si, the oligosilane still formed fine needle-shaped crystals on the surface. Currents measured from the area filled with the crystals (~2 x $10^{-7}$A) were much higher than the background currents (Figure 4-6). In addition, the material was checked for photorsponse; no observable response to UV irradiation of 254nm and 365nm was found.

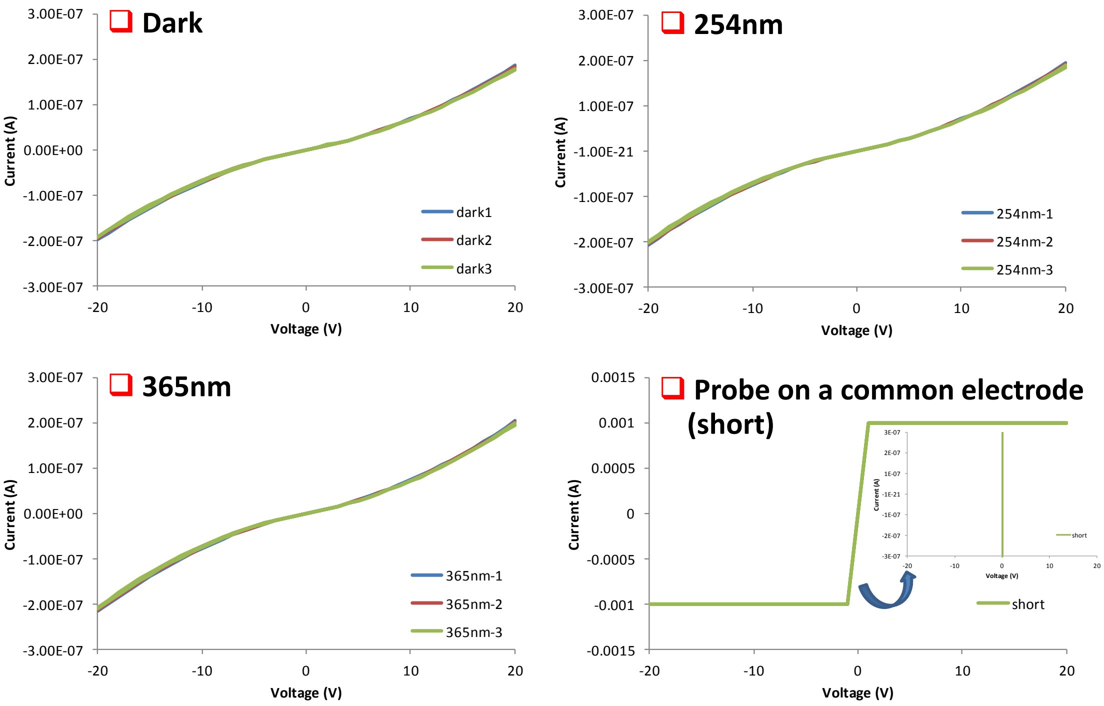

**Figure 4-6 I-V curves of drop casting Si-4-OC1 onto glass slide pre-patterned with gold electrodes**

### *4.3.2 Drop casting with a tiled angle*

When drop casting on a large surface, as shown in Figure 4-7(b), there is no preferred directional growth of the needle-shaped crystals. Drop casting on the surface with a tiled angle was evaluated to see whether it can help the alignment of needle-shaped crystals. While the alignment seemed to be better along the bottom corner, the effect was only valid in very small area.

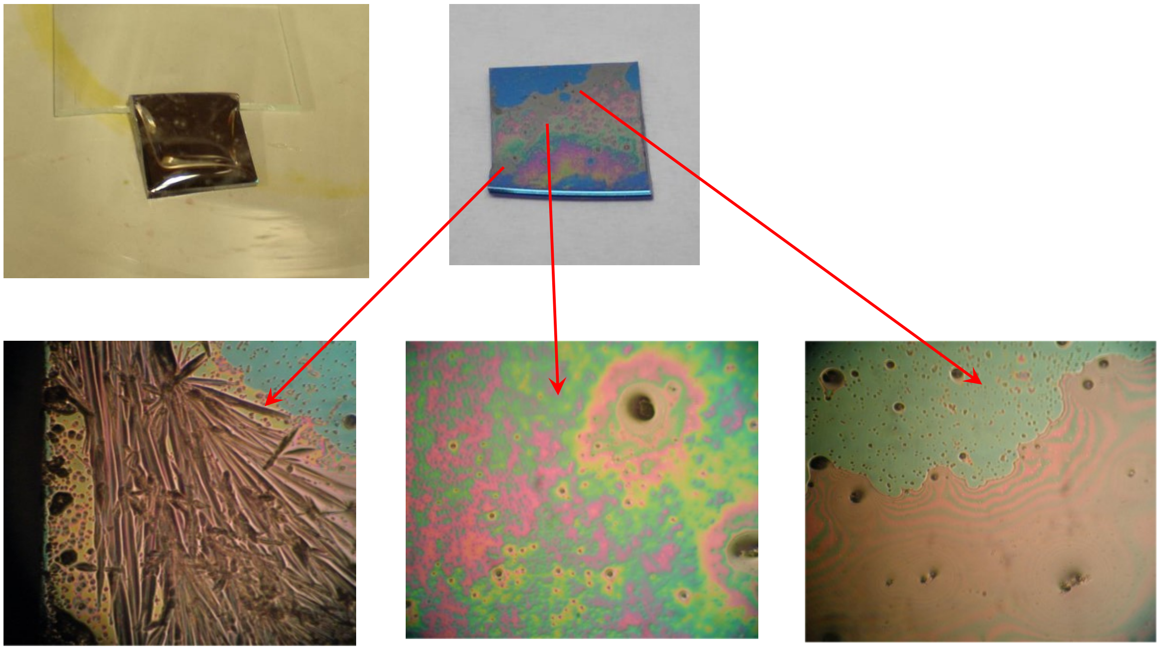

**Figure 4-7 Si-4-OC1 drop casting on glass slide with a tilted angle**

### *4.3.3 Drop casting in a small defined area*

The needle-shaped crystals seemed to align better in a small area, thus we used n fluorinated paint electrode, Novec, to define different sizes and shapes of small areas. Oligisilane **Si-4-OC6** with a longer alkyl side chain was also applied. As illustrated in Figure 4-8, Scotch tape was first used to protect the area where there should be not Novec coating. After painting with Novec, drying, and removal of Scotch tape, the defined small area was then filled with maximum amount of oligosilane solution possible. As seen in Figure 4-9, the resulting crystalline films have highly directional structure along the long axis of the defined area.

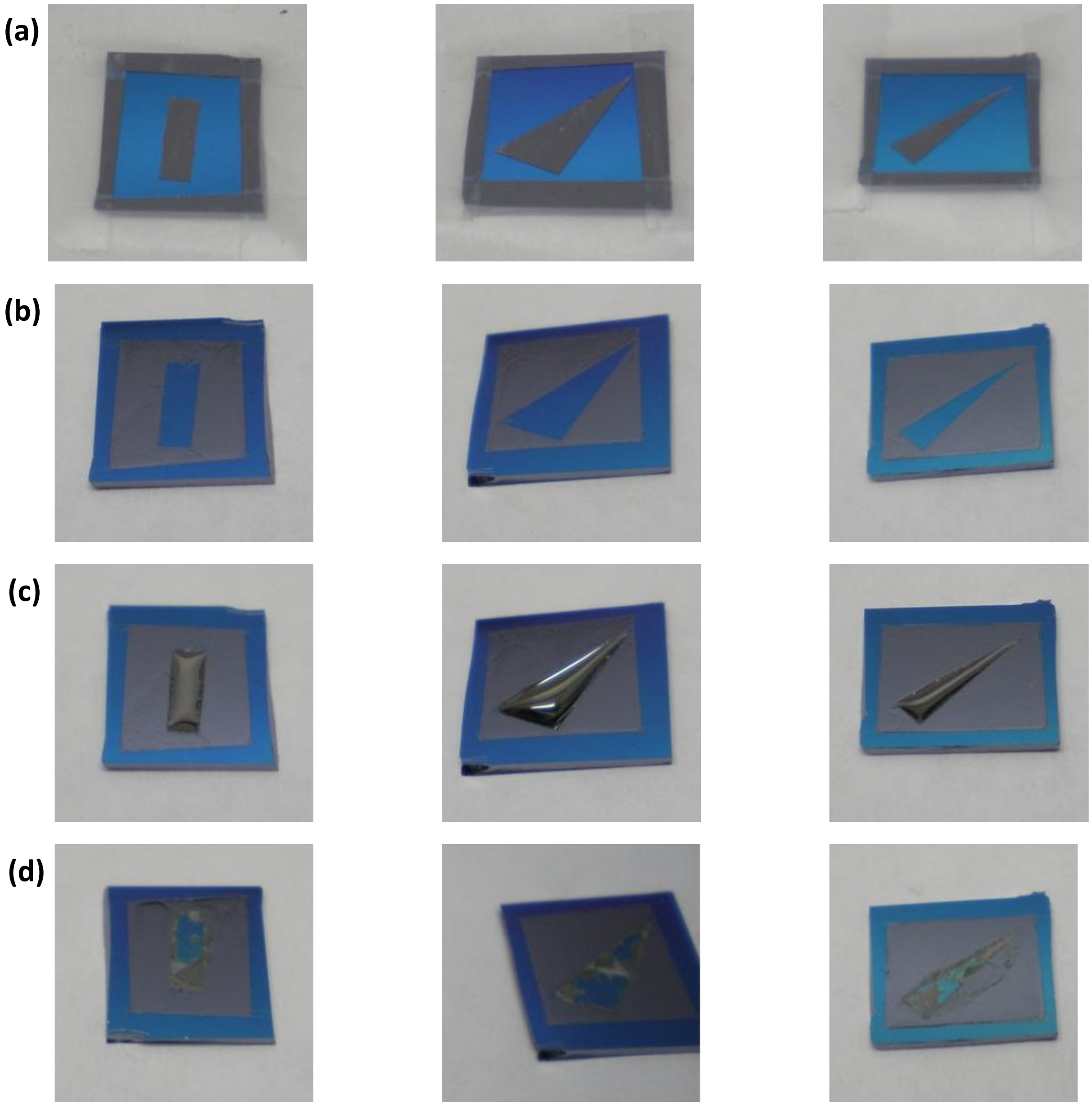

**Figure 4-8 Si-4-OC6 thin film formation**

**(a) pattern with Scotch tape, (b) paint with Novec and remove Scotch tape, (c) dropcast within Novec boundaries, (d) the finished films**

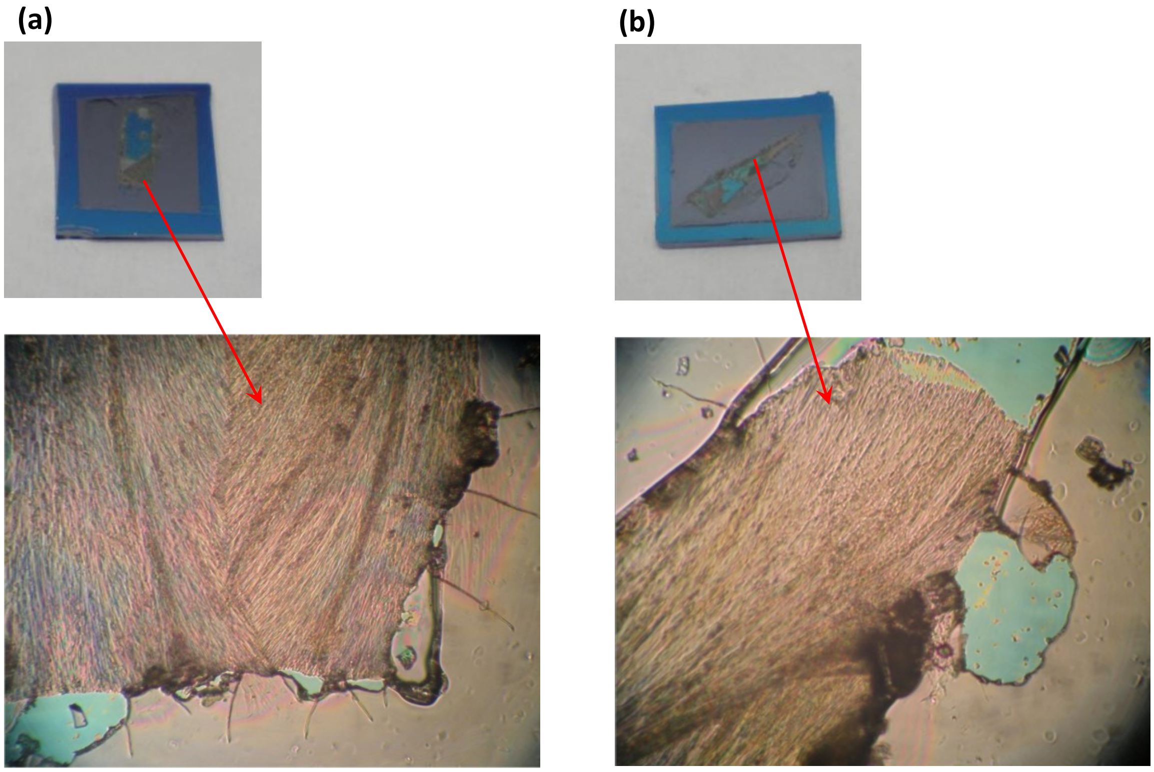

**Figure 4-9 Si-4-OC6 films in small defined areas. (a) rectangle shape, (b) triangle shape**

This method was then applied to glass substrates pre-patterned with gold electrodes using thin metal wires as the shadow mask. The advantage of thin metal wires over TEM grids as shadow mask is that it provided the same small spacing feature while offering a larger electrode area on which to probe.

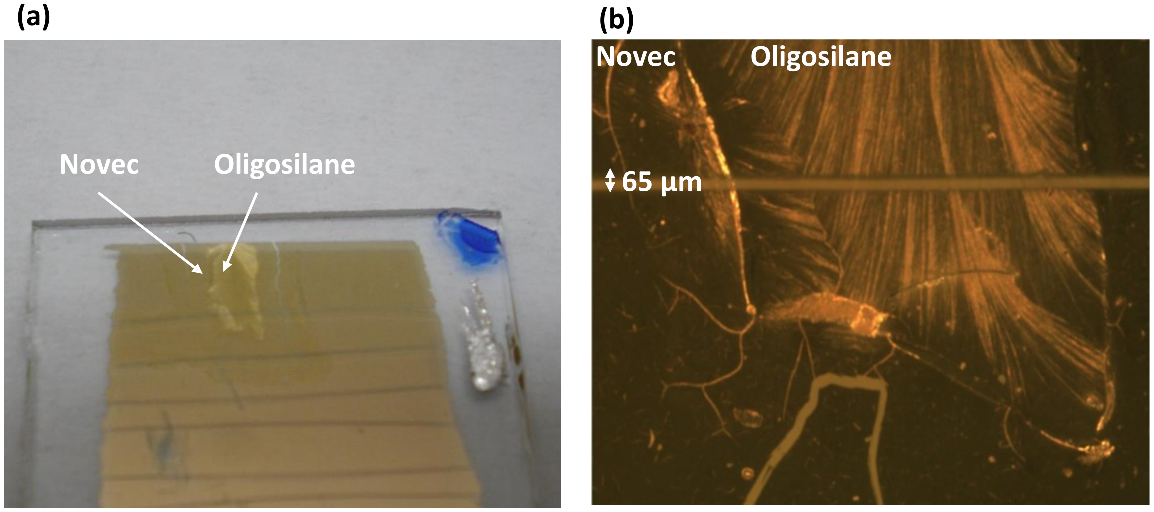

**Figure 4-10 Drop casting of Si-4-OC6 inside a small defined area on a glass slide with pre-patterned electrodes**

From Figure 4-10, it is very clear that the crystals lay across the gap between electrodes. Again, the insulation between electrodes was verified before applying the oligosilane (Figure 4-11). I-V measurement at +/- 5V (Figure 4-12) gave current of ~3 x $10^{-11}$A. Though not very high, it was considerably higher than the background current. And UV irradiation, both 254nm and 365nm, made the I-V curves noisy, indicating some degree of charge injection was happening. The same responses were also seen when measuring at +/- 50V (Figure 4-13) with a higher current of ~4 x $10^{-10}$A.

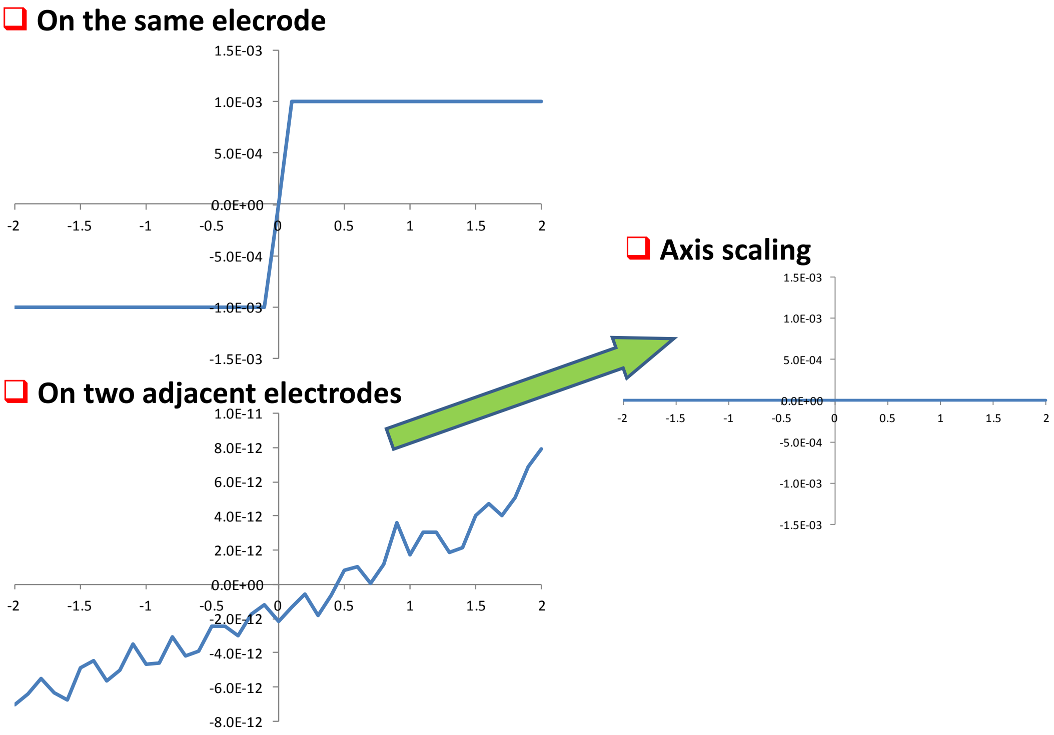

**Figure 4-11 I-V curves of pre-patterned electrodes before drop-casting the oligosilane.**

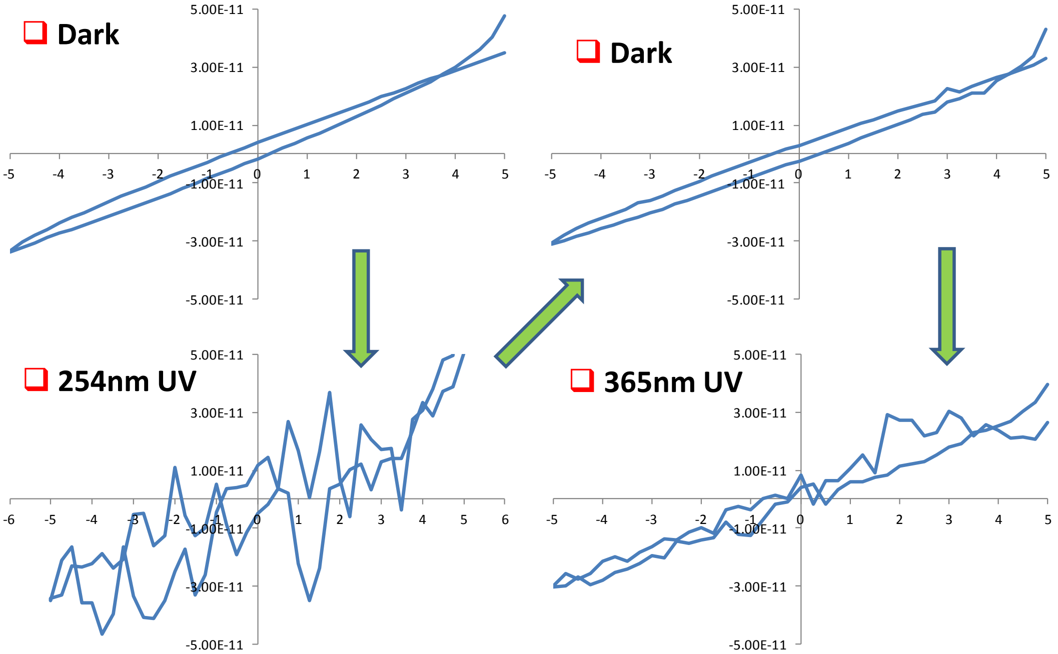

**Figure 4-12 I-V curves of Si-4-OC6 film, measured between +/- 5V**

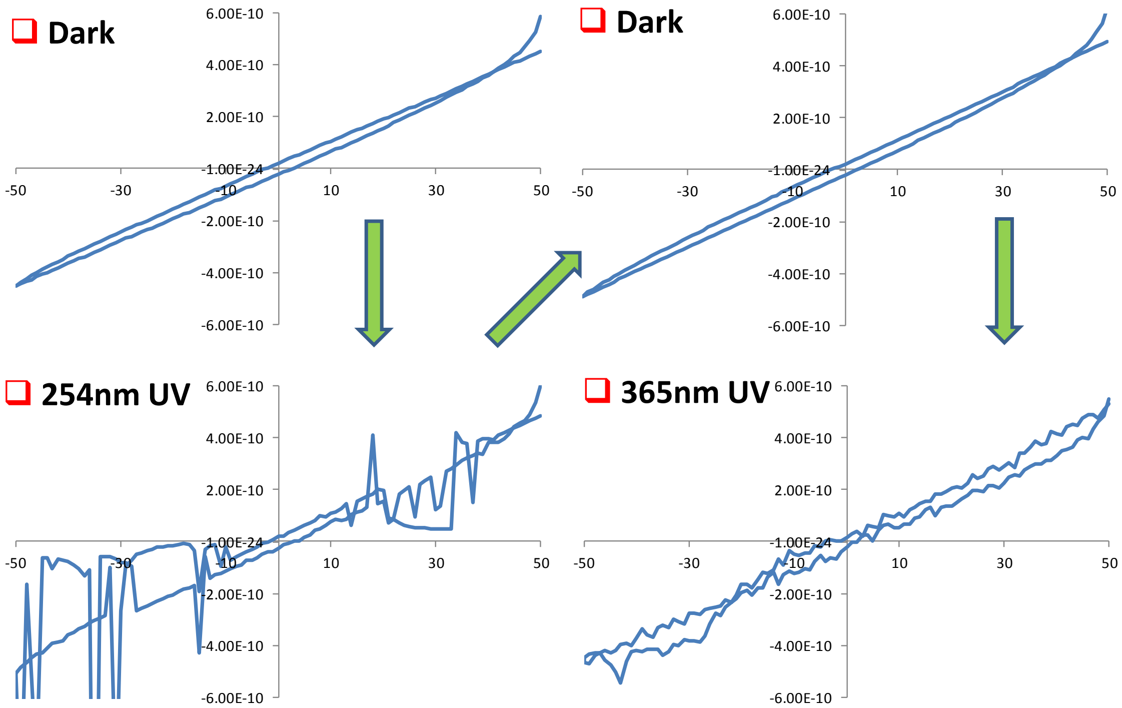

**Figure 4-13 I-V curves of Si-4-OC6 film, measured between +/- 50V**

The obtained current was further enhanced by reducing the electrode spacing from 65µm to 25µm and using oligosilane **Si-6-OC6** with a longer silane backbone. The currents reached 1 x $10^{-8}$A at +/- 20V (Figure 4-14) and 4 x $10^{-8}$A at +/- 50V (Figure 4-15). The noisy responses to UV irradiation were not observed, due the higher current obtained with the smaller electrode spacing. Instead, they showed some, but not very reliable, increase in currents.

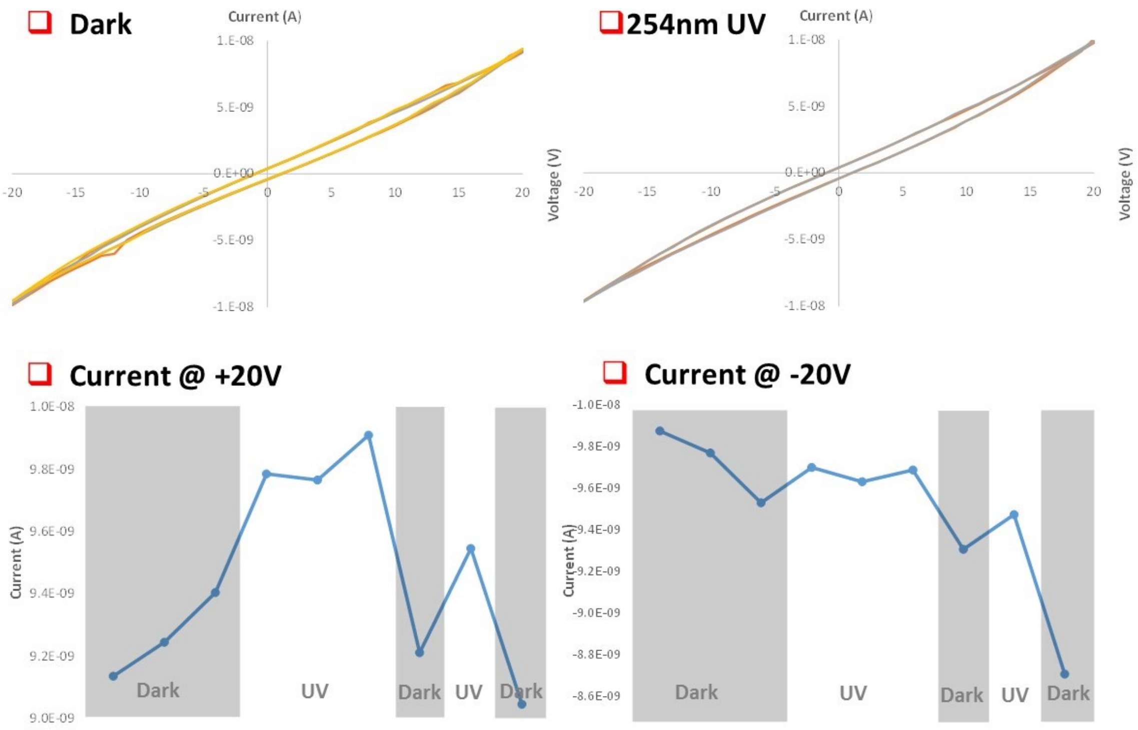

**Figure 4-14 Device made from Si-6-OC6 with 25µm channel length. I-V sweep between +/- 20V and comparison of currents at different conditions**

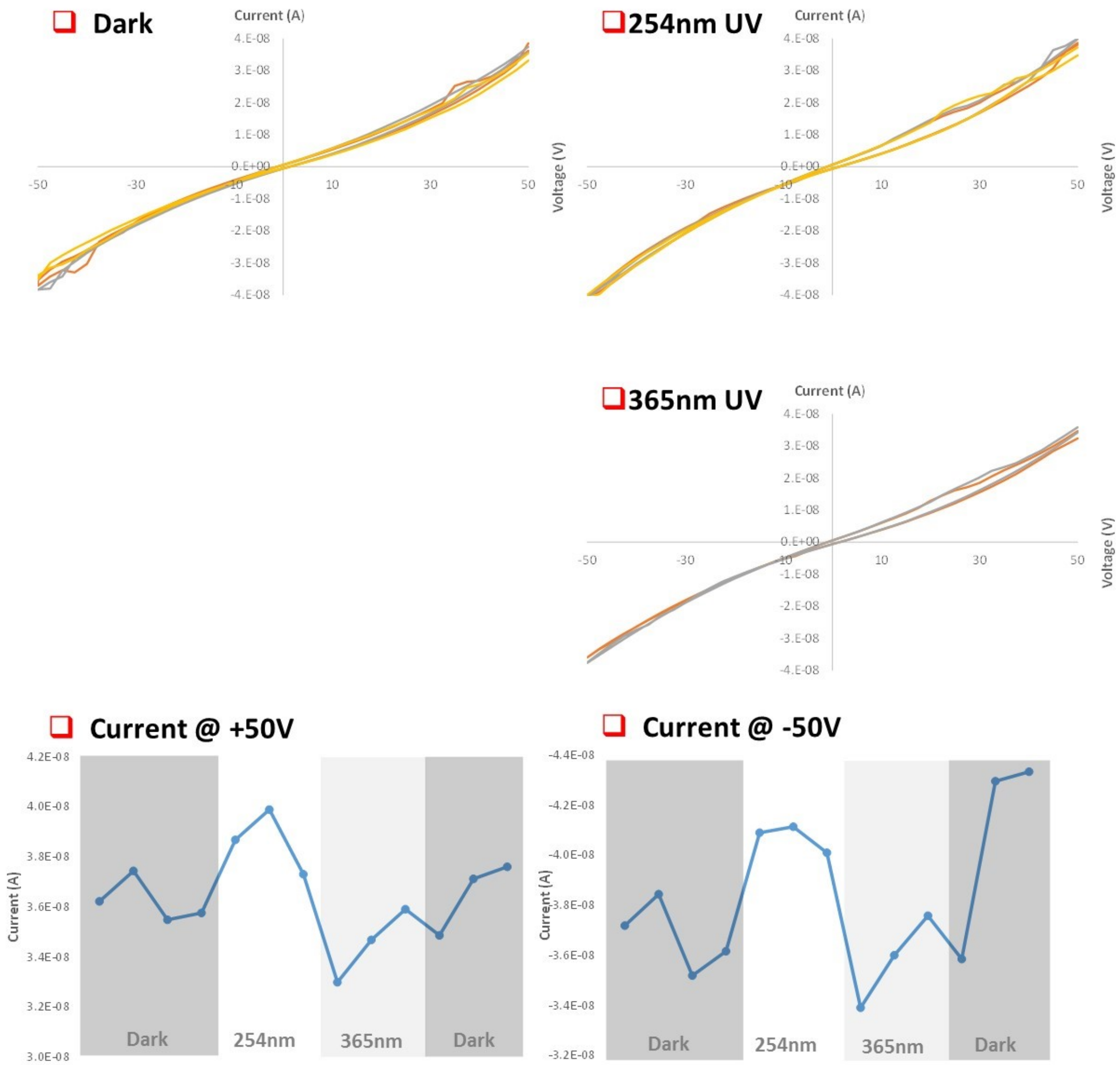

**Figure 4-15 Device made from Si-6-OC6 with 25μm channel length. I-V sweep between +/- 50V and comparison of currents at different conditions**

From the I-V curves sweep between +/-50V, the space-charge-limited was extracted according to the Mott–Gurney law:

$$J = \frac{9\epsilon\mu V^2}{8L^3}$$

The current density is calculated as the obtained current divided by the cross-sectional area of the thin film, which was estimated from the amount of material applied (10 mg/mL x 20 µL), the drop-casting area (0.2cm x 0.5cm), and an estimated mass density of 0.7–1.0 g/cm$^3$.[49]

The $J^{1/2} - V$ plots corresponding to mass density of 0.7 g/cm$^3$ and 1.0 g/cm$^3$ are shown in Figure 4-16 panel (a) and panel (b), respectively. The liner fit between 30V and 50V gave high regression coefficients and the extracted mobility is 0.8-1.4 x 10$^{-3}$ cm$^2$/Vs, corresponding to the lower and upper limits of mass density assumption. This number is similar to the mobilities of methyl-terminated oligoslianes obtained from time-of-flight (TOF) transient photocurrent measurement.[50]

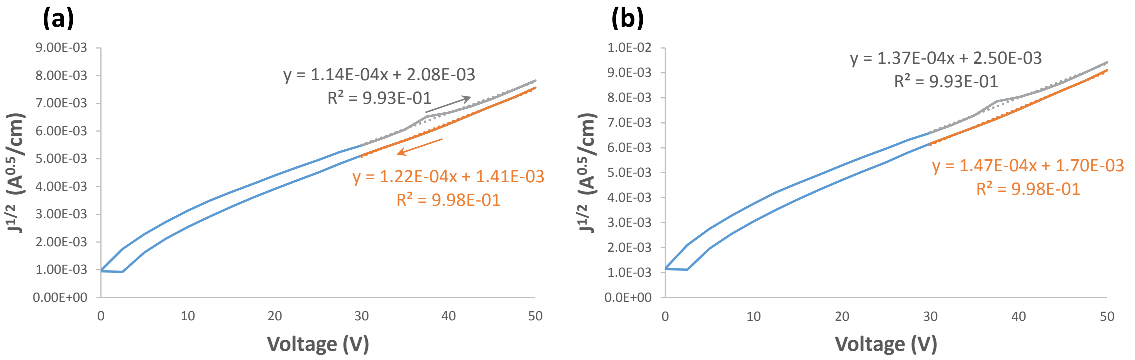

**Figure 4-16 Si-6-OC6 $J^{1/2} - V$ plots corresponding to mass density of (a) 0.7 g/cm$^3$ and (b) 1.0 g/cm$^3$**

As shown in Figure 4-17, the device could not stand the high voltage testing at +/-100V and degraded after the third scan, and thus was not able to yield space-charge-limited currents at a higher voltage.

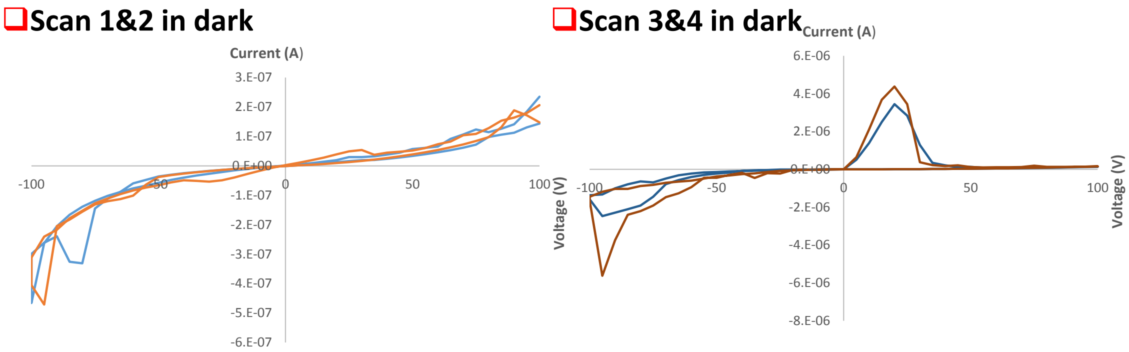

**Figure 4-17 Device made from Si-6-OC6 with 25µm channel length. I-V sweep between +/- 100V**

## 4.4 Conclusions and Outlook

We evaluated different solution process methods for growing oligosilane crystals and successfully controlled the crystal alignment in areas with defined shapes. Optimized device schemes and dimensions were developed to confirm the electric conduction phenomenon, though no reliable UV responses observed. This UV responses could be further confirmed if a more intense UV source is available.

The method developed here can be used as a platform to compare oilgosilanes with different Si backbone length and varied side chains. More detailed understanding can be obtained to establish the structural-conductivity relationships that help using them as charge transporting materials in organic electronics.

## 4.5 Experimental Section

### General

All solvents used for solution process were anhydrous grade solvents from Sigma-Aldrich. Novec coating was purchased from 3M. X-ray diffraction scans were acquired in the Bragg-Brentano ($\theta$-$2\theta$) geometry using a Phillips X-pert Pro X-ray diffraction system. Scan step size was 0.02° and time per step was 2 seconds.

### Device Fabrication and Characterization.

Heavily-doped silicon with 300 nm thermal oxide dielectric layer on top was used for transistor devices. Glass slides were used for two-terminal I-V measurements. Oligosilane solution of 10mg/mL from different solvents were used in spin-coating and drop-casting. Gold electrodes, whether in top contact of bottom contact device schemes, were thermally evaporated in a vacuum chamber using TEM grid, or metal wires of 65μm or 25μm as shadow mask. Device characterization was performed using an Agilent 4155C semiconductor parameter analyzer.

# CHAPTER 5

# Halogenated Fullerene Compounds

## 5.1 Introduction

Fullerenes derivatives that comprise C60 buckyball are an important family in organic electronics. C60 can undergo up to six reversible one-electron reductions and the low-lying LUMO level makes it a good electron accepter. Its ball shape also makes it easier for intermolecular interactions to occur between nearest neighboring molecules. However, the low solubility in common organic solvents limits its use in thin filmfabrication. Therefore, fullerene derivatives with various substituents are made to meet certain chemical/physical properties and process requirements.

Among the numerous fullerene derivatives, phenyl-C61-butyric-acid-methyl-ester ([60]PCBM)) has been intensively studied, mainly because of its use in bulk heterojunction organic photovoltaics consisting of PCBM/P3HT blends.[51] Compounds with similar molecular structure to PCBM but with altered side chain or functional group[52] can help identifying how different chemical features change the efficiencies of mechanistic steps of organic electronic devices, such as charge separation and recombination.

## 5.2 Fluoroalkylated Fullerene Compound

The unique low surface energy of fluorinated compounds offers the offer the opportunity for interfacial studies including self-assembly[53] and surface aggregation.[54] A fullerene derivative with a fluoroalkyl ester side chain was synthesized using the reaction route shown in Figure 5-1. The carboxylic acid starting material was esterified with a fluoroalkyl alcohol. After converting to hydrazine, the side group underwent [3+2] cycloaddition with C60 to yield a [5,6]open product and then thermally isomerized to the more thermodynamically stable [6,6]closed product.

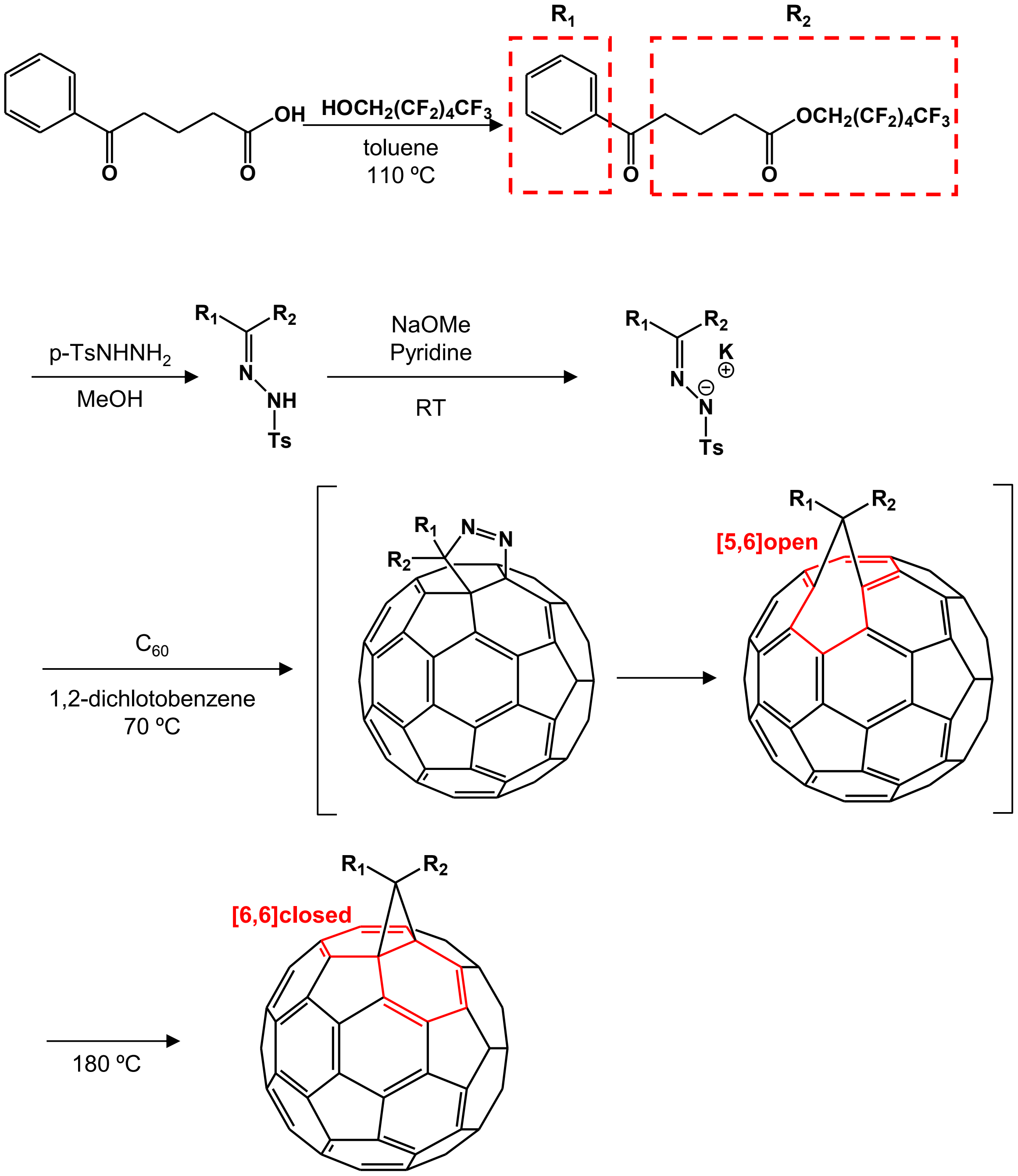

**Figure 5-1 Preparation of the fluoroalkylated fullerene compound**

Although bearing a long fluoalkyl side chain, the fullerene derivative is still soluble in some organic solvents and thus enabled thin film fabrication using solution processes. The transfer curves of transistors made from trifluoritoluene solution spin-coated films were shown in Figure 5-2. 1800RPM gave significantly better mobility of 9.8 x 10-3 cm$^2$/Vs than lower rotation speed did.

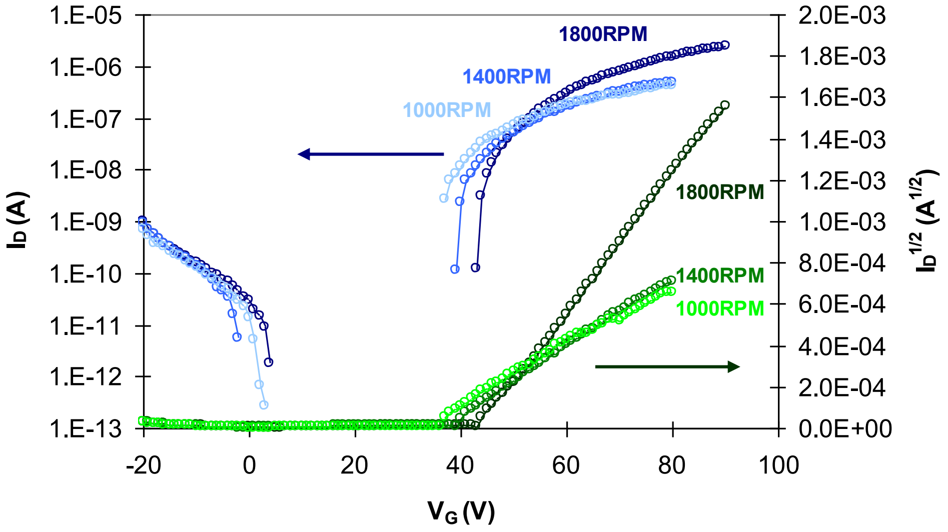

**Figure 5-2 Transfer curves of fluoalkyl fullerene made from trifluotoluene**

As shown in Figure 5-3, spin-coating from chlorobenzene at 2000RPM resulted in similar mobility of 9.9 x 10$^{-3}$ cm$^2$/Vs. For comparison, PCBM transistors were also made under the same process conditions and exhibited mobility if 5.4 x 10$^{-3}$ cm$^2$/Vs.

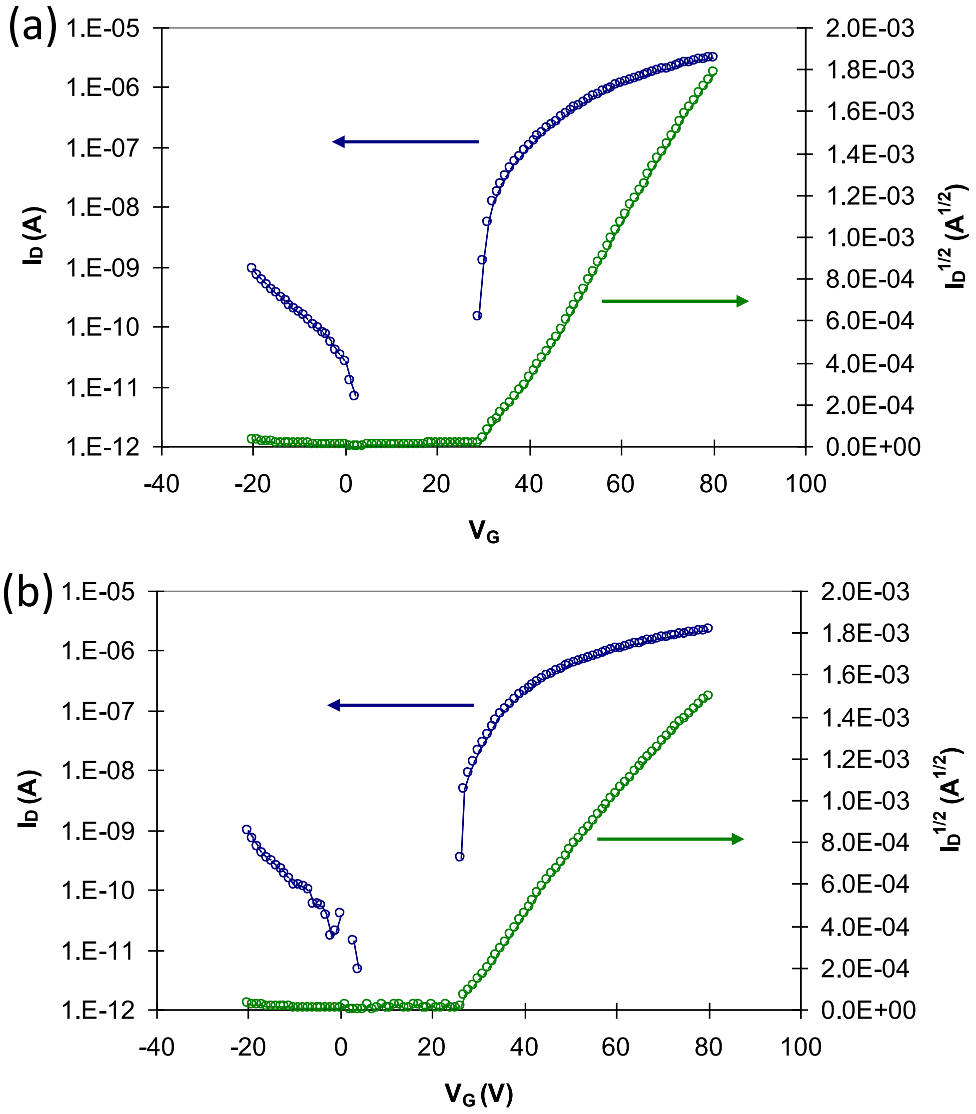

**Figure 5-3 Transfer curves of transistors from chlorobenzene solution: (a) fluoroalkylated fullerene (b)PCBM**

## 2.3 Iodinated Fullerene Compound

Iodine atom has high electron density that can increase scattering length density and provide better contrast to other materials in X-ray reflectometry. Iodine is also a good nucleophile and a good leaving group, which makes iodinated compounds versatile building blocks for other compounds. Synthesis of iodinated fullerene began with iodination on benzophenone derivatives as shown in Figure 5-4. By controlling the amount of N-Iodosuccinimide (NIS) in the reaction, the benzophenone can be either di-iodinated or tetra-iodinated. The tetra-iodo compound was then attached to C60 following a similar procedure used for the fluoalkylated fullerene mentioned in the previous section.

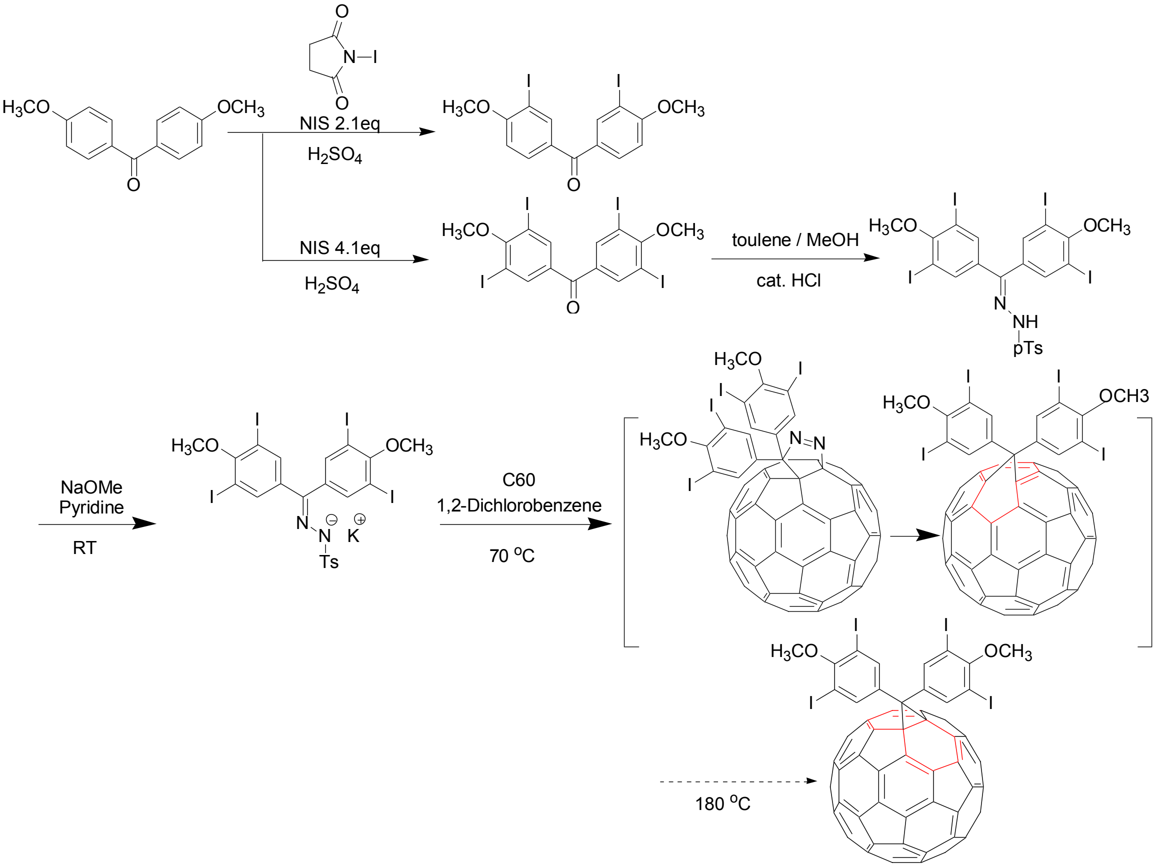

**Figure 5-4 Iodination and synthesis of iodinated fullerene compound**

There were only two types of proton signals in the $^1$H NMR of the final product. To further confirm the molecular structure of the obtained fullerene, another reaction route that put the iodination in the last step, as shown in Figure 5-5, was pursued and the $^1$H NMR of the final product was the same as the one that underwent iodination first.

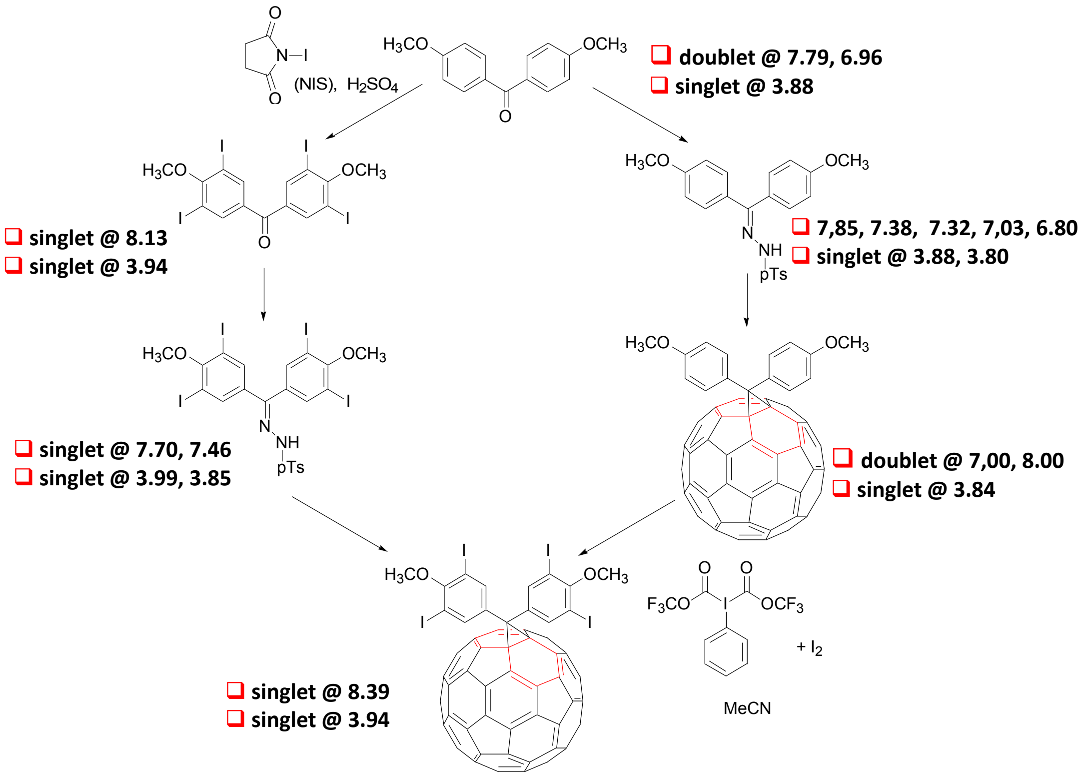

**Figure 5-5 Two reaction routes and $^1$H NMR results that lead to the iodinated fullerene**

The presence of the iodo substituent was also confirmed from X-ray photoelectron spectroscopy (XPS), as shown in Figure 5-6.

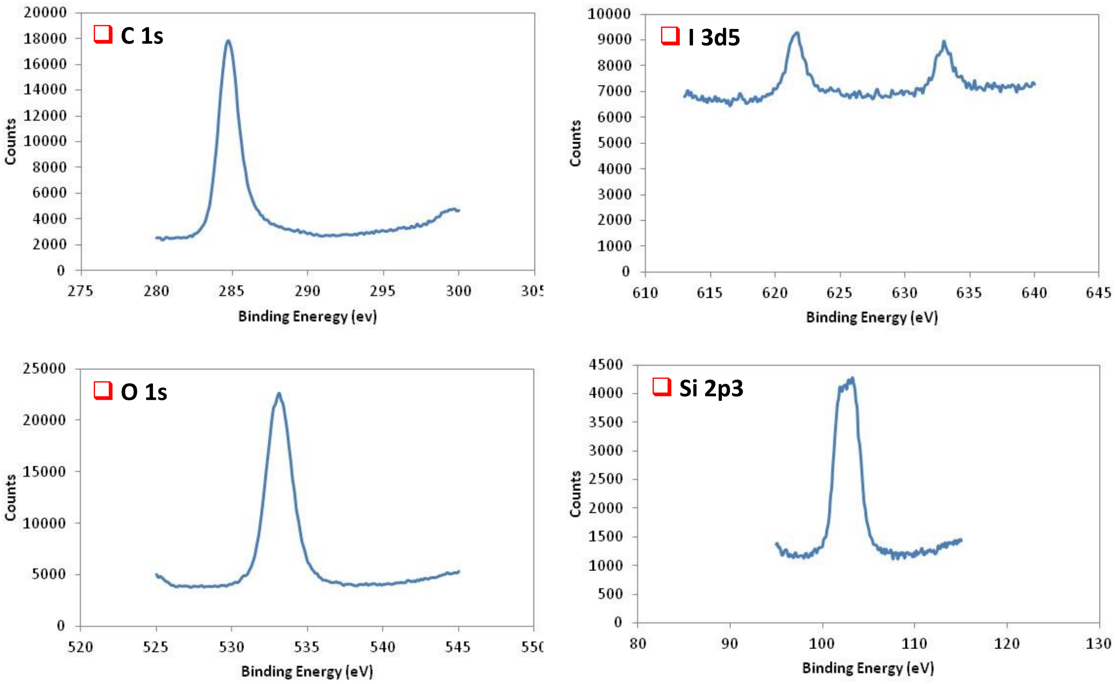

**Figure 5-6 The XPS result of thin film made from the iodinated fullerene**

## 5.4 Conclusions

Fullerenes are an important family in organic electronics, especially in bulk heterojunction organic photovoltaics. A fluoroalkylated fullerene compound was synthesized and demonstrated as a solution processable n-type material with mobility of 0.01 cm$^2$/Vs, comparable to that of PCBM made in the same condition. An iodinated fullerene compound that can be used for X-ray and neutron reflectivity analysis and for further functionalization was synthesized via two different reaction routes and structurally identified from $^1$H NMR and XPS.

## 5.5 Experimental Section

### General

C60 and PCBM were purchased from Nano-C (Westwood, MA). 1H NMR spectra were recorded with a Bruker Avance 400 MHz spectrometer. X-ray photoelectron spectroscopy (XPS) were performed using Mg Kα radiation.

**Phenyl-C61-buryric acid 1H,1H-undecafluoro-1-hexyl ester**. Hydrazone (4 mmol) was added to a 250mL three-necked flask and filled with nitrogen. Dry pyridine (30mL) and NaOMe (225mg) were then added. The mixture was stirred for 30min at room temperature and then a solution of 1.44g C60 in 100mL 1,2-dichlorobenzene was added. The mixture was heated at 70°C for 24h and then was refluxed for 7h. The solvents were then evaporated, the mixture was separated and purified by silica gel chromatography with toluene. $^1$HNMR (400MHz, $CDCl_3$): 7.94 (d, 2H, $J$ = 11.6 Hz), 7.58-7.42 (m, 3H), 4.38(t, 2H, $J$ = 8.8 Hz), 2.94-2.88(m, 2H), 2.57-2.44 (m, 2H), 2.24-2.13 (m, 2H).

### Device Fabrication and Characterization

Heavily-doped silicon with 300 nm thermal oxide dielectric layer on top was used as the substrate. Thin-film transistors in top-contact/bottom-gate configuration were fabricated on the silicon substrate using spin-coated fullerene from 10mg/mL solution. The channel widths were 6 mm, and the channel lengths were 250μm. Device characterization was performed using a Keithley 4200 Semiconductor Parameter

Analyzer in a Janis Research ST-500-1 vacuum triaxial probe station. Mobility was calculated from the saturation regime and fitted in the regions of highest slope.

# CHAPTER 6

## Polystyrene Bilayer Scheme for X-Ray and Neutron Reflectometry

### 6.1 Introduction

Interfaces, whether in photovoltaics, diodes, or transistors, play an important role in the operation of organic electronic devices. However, they are usually buried inside the device film stacks and not easily investigated. Although the interfaces can be revealed after removing the top layers, the device is no longer functional and the interface properties may be altered. Reflectometry offers an opportunity for the direct observation of a device while it is functioning and thus provides more interesting details.

Good reflectometry measurement relies on sufficient contrast between the two sides of interfaces. That is, the scattering length densities for electrons or neutrons have to be very different among the constituent layers. For the purposes of our current study, polystyrenes with different functional substituents can provide the difference in electron or neutron densities as well as alter the dielectric properties.

### 6.2 Fabrication of Polystyrene Bilayers

Making bilayer film stacking structures is the first step in utilizing reflectometry measurement for more complicated film schemes and interfaces. However, the polystyrenes of interest, shown in Figure 6-1, have good solubilities in common organic solvents. Other than finding orthogonal solvent combinations, lowering the solubility by cross-linking one of the polystyrenes would be a feasible approach.

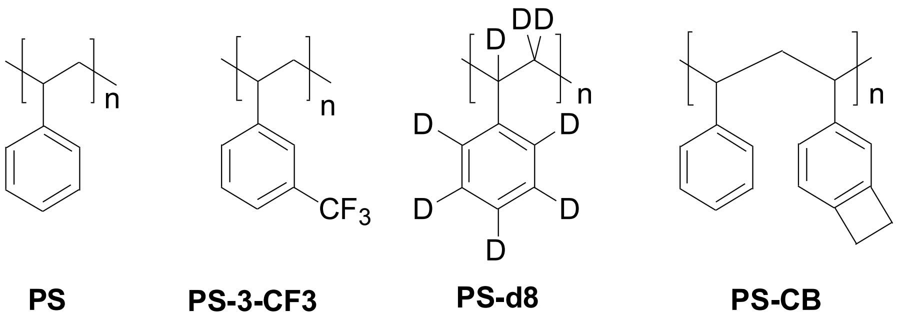

**Figure 6-1 Polystyrene derivatives used in bilayer schemes**

Preliminary efforts on UV-initiated crosslinking were not successful even with the maximum power of solar simulator or photolithography exposure systems. To attempt thermal annealing instead, polystyrenes with 5% and 10% of 3,4-cyclobutenostyrenes (PS-CB) as the cross-linker were made. Spin-coating of them from chloroform solution followed by 250°C thermal annealing for one hour under nitrogen gave the cross-linked films that were no longer soluble in chloroform. After thermal annealing, the polystyrene and polystyrene with 5% cross-linker both have a certain degree of surface aggregation and were not reflective, as shown in Figure 6-2. Only the polystyrene with 10% cross-linker retained a smooth and reflective surface; thus it was chosen as the bottom layer for the bilayer scheme.

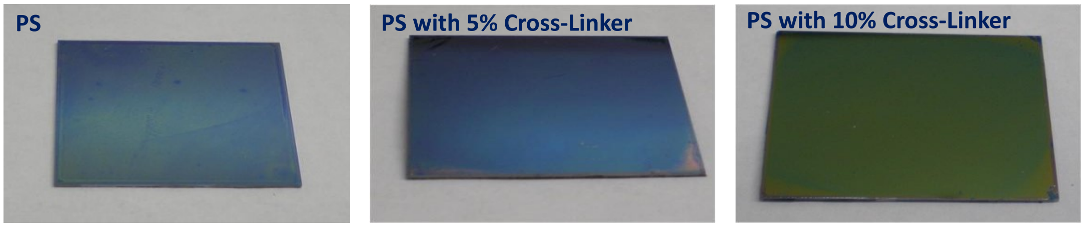

**Figure 6-2 Preparation of the fluoroalkylated fullerene compound**

## 6.3 XRR and NR Measuerments of Polystyrene Bilayers

Deuterated polystyrene (PS-d8) and poly-3-(trifluoromethyl)styrene (PS-3CF3) were spin-coated from chloroform solution onto the cross-linked polystyrene bottom layer. The X-ray reflectivity (XRR) measurement results of bilayers with PS-3-CF3 and PS-d8 on cross-linked PS-CB were shown in Figure 6-3. The bilayer with PS-3-CF3 exhibited a bilayer scheme from the two oscillation frequencies, while no bilayer oscillation was seen with PS-d8 due to the similar electron scattering length density. The bilayer with PS-d8 still showed strong overall reflection, indicating smooth interfaces.

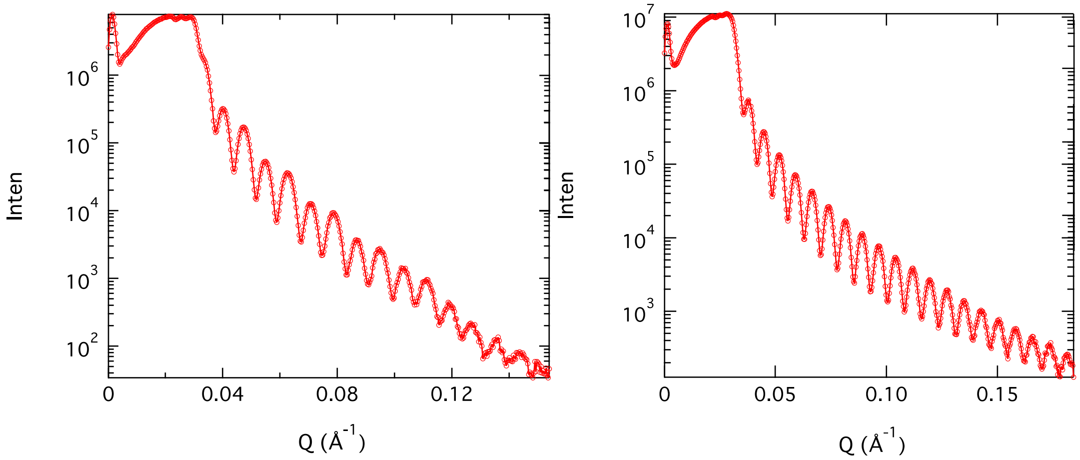

**Figure 6-3 XRR results of bilayer with PS-3-CF3 (left) and PS-d8 (right) on PS-CB**

The neutron reflectivity measurement results of bilayers with PS-3-CF3 and PS-d8 on cross-linked PS-CB were shown in Figure 6-4. Both film schemes exhibited the bilayer signature of two oscillation frequencies.

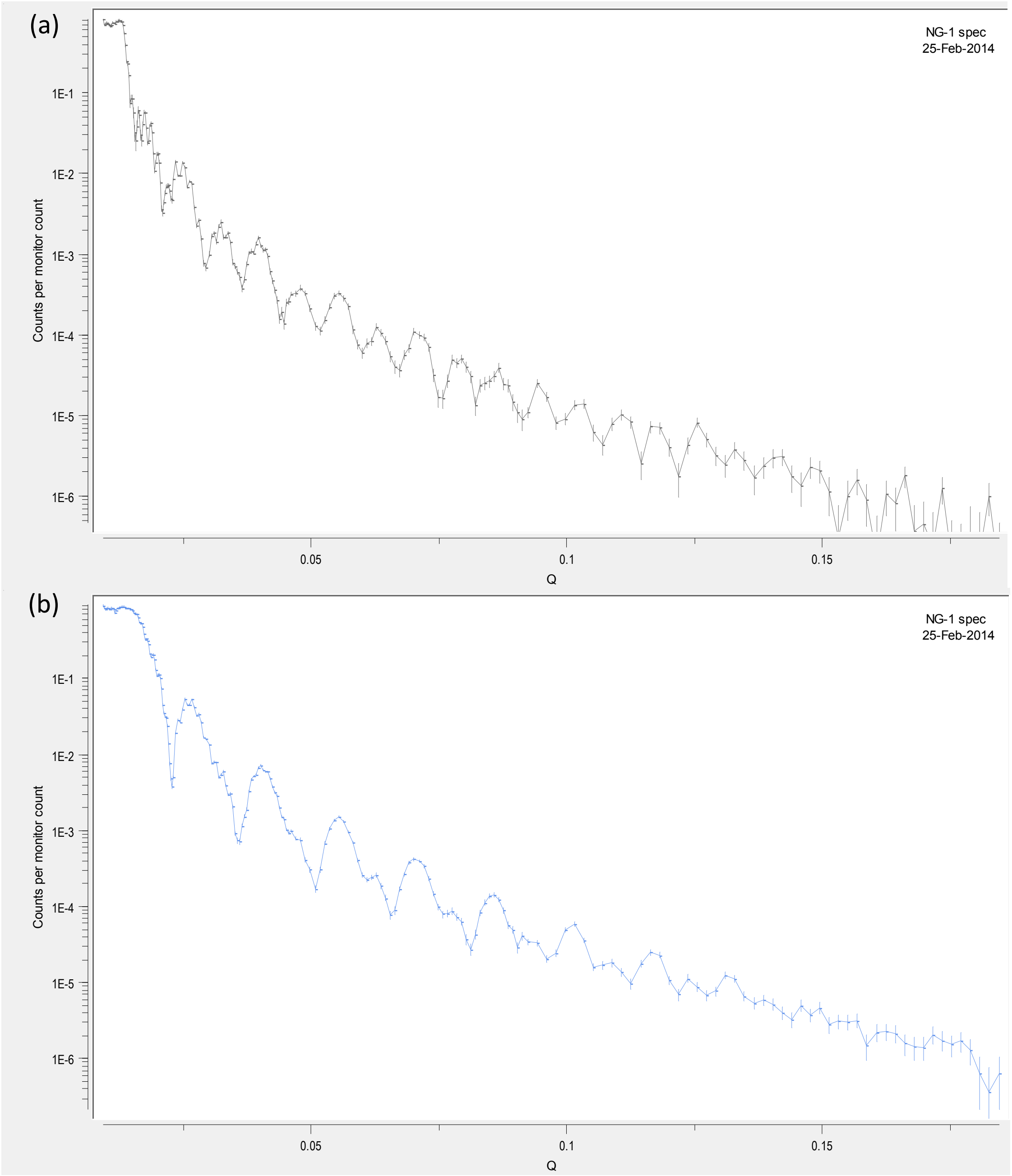

**Figure 6-4 Neutron reflectivity results of bilayer scheme of (a) PS-3-CF3 and (b) PS-d8 on PS-CB**

## 6.4 Conclusions

Polystyrene bilayer thin film stacking schemes were realized using thermally cross-linked polystyrene bottom layer and spin-coated top layer. X-ray and neutron reflectometry further confirmed the film schemes as bilayer with smooth and reflective interfaces, offering the basis to probe more complicated layered device architectures.

## 6.5 Experimental Section

### General

Reflectometry measurements were performed on samples with dimensions of 2 inch x 2 inch. XRR measurements were carried out using diffractometers with Cu X-ray sources at Johns Hopkins University. Neutron reflectometry measurements were carried out using the NG-D Polarized Beam Reflectometer/Diffractometer (PBR) at the NIST Center for Neutron Research.

### Bilayer Film Scheme Fabrication

Heavily-doped silicon with 300 nm thermal oxide dielectric layer on top was used as the substrate. Solutions of polystyrene derivatives were made as 3.5 mg/mL or 7.0 mg/mL from anhydrous chloroform and then filtered with 0.45μm PTFE filter. Thin films were spin-coated at 1500RPM for 60 seconds. After spin-coating, the sample was placed into a chamber preheated at 250°C. The chamber was pumped and purged three times with nitrogen and then the sample was kept at 250°C under nitrogen. After one hour, the chamber was slowly cooled and the sample removed.

# CHAPTER 7

## Conclusions and Outlook

For polycyclic aromatic hydrocarbon systems, increasing the size of the planar conjugated backbones offers stronger cofacial π-π stacking. It is less probable thatr a small conjugated system like pyromellitic diimide, with just one benzene ring, would have sufficient intermolecular interactions in its solid state. However, the weaker π-π interaction also means the molecular arrangement in the solid state is more sensitive to the substituents, whether on the core or the imide nitrogen. It offers a great chance to study the relationship between the molecular structure and the packing phenomena, as was described in Chapter 2.

The correlation further led to selection of an optimized side chain to vary process conditions and molecular structure in Chapter 3. A higher substrate temperature during deposition was enabled by the brominated core and resulted in an exceptional mobility of 0.2 $cm^2/Vs$, the highest PyDI mobility yet reported. Considering the weaker π-π interaction from this small core, this is a substantial electron transport capability. Highest mobilities of other lager polycyclic aromatic hydrocarbon systems are listed in Table 7-1. NTCDI, with five fused benzene ring that contains 20 atoms, offers good packing and high mobility. Among the systems with smaller conjugated cores, pyromellitic diimide provides good mobility in a short and relatively safe synthetic process.

| Compound | Mobility ($cm^2/Vs$) | Size of Conjugated Core (atoms) | LUMO | Bandgap (eV) | Number of Synthetic Steps | Reference |
|---|---|---|---|---|---|---|
| 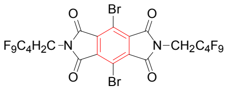 | 0.2<br>(vacuum deposition) | 6 | -4.4 | 3.18 | 3 | this work |
| 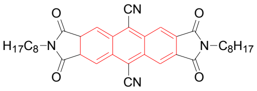 | 0.02<br>(vacuum deposition) | 14 | -4.3<br>(Estimated) | 2.58<br>(Estimated) | 5 | (55) |
| 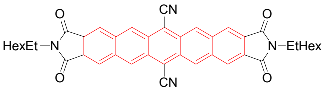 | 0.07<br>(solution deposition) | 22 | -4.15 | 1.9 | 10 | (56) |
| 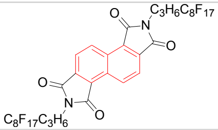 | 0.52<br>(vacuum deposition) | 10 | N/A<br>(low solubility) | N/A | 4 | (57) |
| 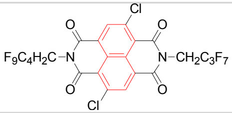 | 1.32<br>(vacuum deposition) | 10 | -4.01 | 2.91 | 5 | (58) |
| 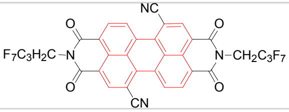 | 0.64<br>(vapor dsposition) | 20 | -4.5 | 2.3 | 3 | (59) |
| 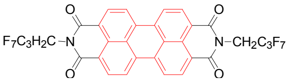 | 1.42<br>(vacuum deposition) | 20 | -3.85 | N/A | 1 | (60) |

**Table 7-1 Highest mobility of different polycyclic aromatic hydrocarbon systems along with their size of conjugated core, LUMO, bandgap, and number of synthetic steps**

In addition, larger conjugated systems result inshifting the absorption bands toward longer wavelength, meaning smaller bandgaps. High mobilities were demonstrated in many highly conjugated heterocyclic aromatic systems, shown in Table 7-2. However, their low bandgaps (< 2 eV) prohibit their use in wide bandgap applications, such as transparent displays and other transparent circuitry.[67] In Table 7-1, the only compound that has a superior combination of mobility and high bandgap compared to the PyDI is the dichloro-NTCDI. As compared with the four dangerous steps to make the precursor anhydride for dichloro-NTCDI, PyDI can be obtained in a short and relatively benign reaction route.

| Compound | Mobility ($cm^2$/Vs) | Size of Conjugated Core (atoms) | LUMO | Bandgap (eV) | Number of Synthetic Steps | Reference |
|---|---|---|---|---|---|---|
| 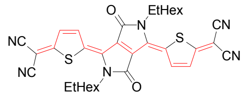 | 0.50<br>(vacuum deposition) | 14 | -4.51 | 1.73 | 4 | (61) |
| 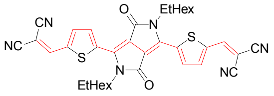 | 0.39<br>(vapor deposition) | 16 | -4.45 | 1.48 | 3 | (62) |
| 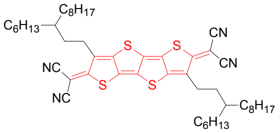 | 0.43<br>(solution deposition) | 20 | -4.3 | 1.8 | 6 | (63) |
| 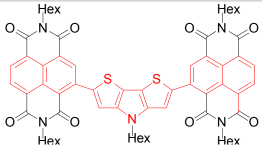 | 1.5<br>(solution deposition) | 31 | -3.7 | 1.6 | 6 | (64) |
| 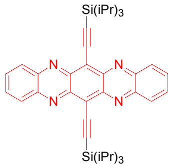 | 1.87<br>(vacuum deposition) | 26 | -4.01 | 1.74 | 5 | (65) |
| 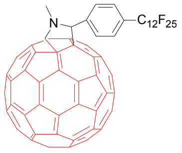 | 0.25<br>(solution deposition) | 60 | -3.63 | N/A | 4 | (66) |

**Table 7-2 Highest mobility of different heterocyclic aromatic and fullerene systems along with their size of conjugated core, LUMO, bandgap, and number of synthetic steps**

Making use of the easy synthetic steps for PyDI, additional structural explorations can be made. For example, polymers with PyDI backbone were synthesized[29] and various process methods and device schemes were evaluated to obtain the working devices and enhanced performances. Further variations on this polymer can take advantage of semifluorinated side chains and spacings similar to those defined by the bromo substituents in the dibromo derivative discussed in Chapter 3.

Similarly, different process methods for growing oligosilane crystals were examined and successfully aligned the crystals in areas with defined shapes. Device schemes and dimensions were optimized to verify the electric conduction phenomenon. The testing method will offer more understanding toward their utilization as charge transporting materials, and suggests the hexasilane core as a promising building block for derivatives with greater substitution and dimensionality.

# REFERENCES CITED

1. Friend1, R. H.; Gymer, R. W.; Holmes, A. B.; Burroughes, J. H.; Marks, R. N.; Taliani, C.; Bradley, D. D. C.; Dos Santos, D. A.; Brédas, J. L.; Lögdlund, M.; Salaneck, W. R.; *Nature*, 1999, 397, 1218.
2. Brabec, C. J.; Sariciftci, N. S.; Hummelen, J. C. *Adv. Funct. Mater.* 2001, 11, 15.
3. Zaumseil, J.; Sirringhaus, H. *Chem. Rev.*, **2007**, 107, 1296.
4. Kao, K. C.; Huang, W. *Electrical Transport in Solids, With Particular Reference to Organic Semiconductors* Pergamon Press, New York, **1981**.
5. Pron, A.; Gawrys, P.; Zagorska, M.; Djurado, D.; Demadrille, R. *Chem. Soc. Rev.* **2010**, *39*, 2577.
6. Arias, A. C.; MacKenzie, J. D.; McCulloch, I.; Rivnay, J. Salleo, A. *Chem. Rev.* **2010**, *110*, 3.
7. Guo, Y; Yu, G.; Liu, Y *Adv. Mater.* **2010**, *22*, 4427.
8. Torsi, L; Maqliulo, M.; Manoli, K.; Palazzo, G. *Chem. Soc. Rev.* **2013**, *42*, 8612.
9. Wang, L. J.; Nan, G. J.; Yang, X. D.; Peng, Q.; Li, Q. K.; Shuai, Z. G. *Chem. Soc. Rev*. **2010**, *39*, 423.
10. Cheung, D.L.; Troisi, A. *Phys. Chem. Chem. Phys*. **2008**, *10*, 5941.
11. Mas-Torrent, M.; Rovira, C. *Chem. Rev.* **2011**, 111, 4833.
12. Hutchison, G. R.; Ratner, M. A.; Marks, T. J. *J. Am. Chem. Soc*. **2005**, *127*, 16866.
13. Bredas, J. L.; Beljonne, D.; Coropceanu, V.; Cornil, J. *Chem. Rev.* **2004,** *104*, 4971.
14. Podzorov, V. *MRS Bull.* **2013**, *38*, 15.
15. Virkar, A. A.; Mannsfeld, S.; Bao, Z.; Stingelin, N. *Adv. Mater.* **2010**, *22*, 3857.
16. Lee, J.; Kaake, L. G.; Cho, J. H.; Zhu, X. Y.; Lodge, T. P.; Frisbie, C. D. *J. Phys. Chem. C **2009***, *113*, 8972.
17. Jung, B. J.; Tremblay, N. J.; Yeh, M.-L.; Katz, H. E. *Chem. Mater.* **2011**, *23*, 568.
18. Tang, M. L.; Bao, Z. *Chem. Mater.* **2011**, *23*, 446.
19. Katz, H. E.; Johnson, J.; Lovinger, A. J.; Li, W. J. *J. Am. Chem. Soc.* **2000**, *122*, 7787.
20. Wang, Y.; Herron, N.; Grushin, V. V.; LeCloux, D.; Petrov, V. *Appl. Phys. Lett*. **2001**, *79*, 449.

21. Zheng, Q. D.; Huang, J.; Sarjeant, A.; Katz, H. E. *J. Am. Chem. Soc.* **2008**, *130*, 14410.

22. Natali, D.; Caironi, M. *Adv. Mater.* **2012**, *24*, 1357.

23. Jung, B. J.; Lee, K.; Sun, J.; Andreou, A. G.; Katz, H. E. *Adv. Funct. Mater.* **2010**, *20*, 2930.

24. Chen, J. H.; Subramanian, S.; Parkin, S. R.; Siegler, M.; Gallup, K.; Haughn, C.; Martin, D. C.; Anthony, J. E. *J. Mater. Chem.* **2008**, *18*, 1961.

25. El Gemayel, M.; Treier, M.; Musumeci, C.; Li, C.; Muellen, K.; Samori, P. *J. Am. Chem. Soc.* **2012**, *134*, 2429.

26. Thalacker, C.; Roger, C.; Würthner, F. *J. Org. Chem.* **200**6, *71*, 8098.

27. Würthner, F.; Ahmed, S.; Thalacker, C.; Debaerdemaeker, T. *Chem. Eur. J.* **2002**, *8*, 4742.

28. Jones, B. A.; Facchetti, A.; Marks, T. J.; Wasielewski, M. R. *Chem. Mater.* **2007**, *19*, 2703.

29. Kola, S.; Kim, J. H.; Ireland, R.; Yeh, M.-L.; Smith, K.; Guo, W.; Katz, H. E. *ACS Macro Lett.* **2013**, *2*, 664.

30. DiBenedetto, S. A.; Facchetti, A.; Ratner, M. A.; Marks, T. J. *Adv. Mater.* **2009**, *21*, 1407.

31. Cuha, L.-L.; Zaumsell, J.; Chang, J.-F.; Ou, E. C.-W.; Ho, P. K.-H.; Sirringhaus, H.; Friend, R. H. *Nature*, **2004**, 194.

32. Nakayama, K.-I.; Yokoyama, M.; Pu, Y.-J.; Kido, J. *Organic Light Emitting Diode - Material, Process and Devices*, *2011*, 147.

33. Jones, B. A.; Facchetti, A.; Wasielewski, M. R.; Marks, T. J. *J. Am. Chem. Soc.* **2007**, *129*, 15259.

34. Gao, X.; Di, C.; Hu, Y.; Yang, X.; Fan, H.; Zhang, F.; Liu, Y.; Li, H.; Zhu, D. *J. Am. Chem.* Soc. **2010**, *132*, 3697.

35. Sommer M. *J. Mater. Chem. C* **2014**, DOI: 10.1039/C3TC31755B

36. Schmidt, R.; Oh, J. H.; Sun, Y.-S.; Deppisch, M.; Krause, A.-M.; Radacki, K.; Braunschweig, H.; Könemann, M.; Erk, P.; Bao, Z.; Würthner F. *J. Am. Chem. Soc.* **2009**, *131*, 6215.

37. Lyncha, D. E.; Hamilton. D. G. *Acta Cryst. E.***2004**, *60*, o597.

38. Suh, D. H.; Chung, E. Y.; Hong, Y. T.; Choi, K.-Y. *Die Angew. Makromol. Chem.* **1998**, *254*, 33.

39. Gilman, H.; Atwell, W. H.; Schwebke, G. L. *J. Organomet. Chem.* **1964**, 2, 369.

40. Gilman, H.; Morris, P. J. *J. Organomet. Chem*. **1966**, 6, 102.

41. Kepler, R. G.; Zeigler, J. M.; Harrah, L. A.; Kurtz, S. R. *Phys. Rev. B* **1987**, 35, 2818.

42. Abkowitz, M.; Ba:ssler, H.; Stolka, M. *Philos. Mag. B* **1991**, 63, 201

43. Pope, M.; Swenberg, C. *Electronic Processes in Organic Crystals and Polymers, 2nd Ed.* Oxford University Press, **1999**, Ch. 11.

44. George, C. B.; Ratner, M. A.; Lambert, J. B. *J. Phys. Chem. A* **2009**, 113, 3876.

45. Klausen, R. S.; Widawsky, J. R.; Steigerwald, M. L.; Venkataraman, L.; Nuckoll, C. *J. Am. Chem. Soc.* 2012, 134, 4541.

46. Venkataraman, L.; Klare, J. E.; Nuckolls, C.; Hybertsen, M. S.; Steigerwald, M. L. *Nature* **2006**, 442, 904.

47. Park, Y. S.; Whalley, A. C.; Kamenetska, M.; Steigerwald, M. L.; Hybertsen, M. S.; Nuckolls, C.; Venkataraman, L. *J. Am. Chem. Soc.* **2007**, 129, 15768.

48. Venkataraman, L.; Klare, J. E.; Tam, I. W.; Nuckolls, C.; Hybertsen, M. S.; Steigerwald, M. L. *Nano Lett.* **2006**, 6, 458.

49. Jones, R. G.; Ando, W.; Chojnowski, J. Silicon-*Containing Polymers: The Science and Technology of Their Synthesis and Applications*, Springer Publishing Company, New York, **2001**, 559.

50. Okumoto, H.; Yatabe, T.; Richter, A.; Peng, J.; Shimomura, M.; Kaito, A.; Minami, N. *Adv. Mater*. **2003**, 15, 716.

51. Dennler, G.; Scharber, M. C.; Barbec, C. J. *Adv. Mater.* **2009**, *21*, 1323.

52. He, Y.; Li, Y. *Phys. Chem. Chem. Phys.* **2011**, *13*, 1970.

53. Ulman, A. *Chem. Rev.* **1996**, *96*, 1533.

54. Iyengar, D. R.; Perutz, S. M.; Dai, C. A.; Ober, C. K.; Kramer, E. J. *Macromolecules* **1996**, 29, 1229.

55. Wang, Z.; Kim, C.; Facchetti, A.; Marks, T. J. *J. Am. Chem. Soc.*, **2007**, 129, 13362.

56. Chang, J.; Qu, H, OOI, Z.; Zhang, J.; Chen, Z.; Wuab, J.; Chi, C. *J. Mater. Chem. C.*, **2013**, 1, 456.

57. Chen, S.-C.; Ganeshan, D.; Cai, D.; Zheng, Q.; Yin, Z.; Wang, F. *Org. Electron.*, **2013**, 14, 2859.

58. Oh, J. H.; Suraru, S.; Lee, W.; Könemann, M.; Höffken, H. W.; Röger, C.; Schmidt, R.; Chung, Y.; Chen, W.; Würthner, F.; Bao, Z., *Adv. Funct. Mater.*, **2010**, 20, 2148.

59. Soeda, J.; Uemura, T.; Mizuno, Y.; Nakao, A.; Nakazawa, Y.; Faccjetti, A.; Takeya, J. *Adv. Mater.*, **2011**, 23, 3681.

60. Schmidt, R.; Oh, J. H.; Sun, Y.; Deppisch, M.; Krause, A.; Radacki, K.; Braunschweig, H.; Könemann, M.; Erk, P.; Bao, Z.; Würthner, F. *J. Am. Chem. Soc.*, **2009**, 131, 6215.

61. Qiao, Y.; Guo, Y.; Yu, C.; Zhang, F.; Xu, W., Liu, Y.; Zhu, D. *J. Am. Chem. Soc.*, **2012**, 134, 4084.

62. Yoon, W. S.; Park, S. K.; Cho, I.; Oh, J.-A.; Kim, J. H.; Park, S. Y. *Adv. Funct. Mater.* **2013**, 23, 3519.

63. Wu, Q.; Li, R.; Hong, W.; Li, H.; Gao, X.; Zhu, D. *Chem. Mater.*, **2011**, 23, 3138.

64. Polander. L. E.; Tiwari, S. P.; Pandey, L.; Seifried, B. M.; Zhang, Q.; Barlow, S.; Risko, C.; Brédas , J.; Kippe;em, B.; Marder, S. R,; *Chem. Mater.*, **2011**, 23, 3408.

65. Liang, Z.; Tang, Q.; Xu, J.; Miao, Q. *Adv. Mater.*, **2011**, 23, 1535.

66. Chikamatsu, M.; Itakura, A.; Yoshida, Y.; Azumi, R.; Yase, K. *Chem. Mater.*, **2008**, 20, 7365..

67. Zhang, J.-L.; Nan, Y.-X.; Li, H.-G.; Qiu, W.-M.; Yang, X.; Wu, G.; Chen, H.-Z.; Wang, M. *Sensor Acuat. B-Chem*, **2012**, 162, 361.

# CURRICULUM VITAE

---

## Ming-Ling Yeh

### EDUCATION

**Johns Hopkins University** | Baltimore, MD 2008-2014

*PhD, Materials Science and Engineering*

Dissertation | 'Molecular Design and Process Aspects of Pyromellitic and Oligosilane Small Molecule Organic Semiconductors'

**National Sun Yat-Sen University** | Kaohsiung, TAIWAN 1996-1998

*MS, Chemistry*

Thesis | 'Synthesis of Iridoid Monoterpenes and Prostaglandins, via Photochemical Rearrangement of Bicyclo[2.2.1]hept-5-en-2-one'

**National Taiwan University** | Taipei, TAIWAN 1992-1996

*BS, Chemistry*

### EXPERIENCE

**Taiwan Semiconductor Manufacturing Company (TSMC)** | Taipei, TAIWAN

*Senior Engineer, Advanced Module Technology Division, R&D* 2004-2005

- Develop and improve physical, chemical and electrical properties of low dielectric constant (low-k) materials for better insulation between the conducting metal lines in semiconductors of 65nm generation and beyond ▪ Explore methods and materials that form nano-scale pore-sealing layer to shield porous materials from the penetration of chemical and metal
- Apply surface analytical techniques (SEM, SIMS, AFM, XPS, AES) to determine adhesion, topography, chemical composition and bonding

*Senior Process Engineer, Thin Film Department, Fab 6* 2002-2004

*Process Engineer, Thin Film Department, Fab 6* 2000-2002

- Optimize process condition of silicon oxynitride (SiON) for more stable and uniform thin film
- Use ellipsometry, Fourier transform infrared spectroscopy (FTIR) and residual gas analyzer (RGA) mass spectrometry to characterize film properties and monitor reaction progress

## PEER-REVIEWED PUBLICATIONS

1. Huang, W.; Sinha, J.; **Yeh, M.-L.**; Hardigree, J. F. M.; LeCover, R.; Besar, K.; Rule, A. M.; Breysse, P. N.; Katz, H. E. "Diverse Organic Field-Effect Transistor Sensor Responses from Two Functionalized Naphthalenetetracarboxylic Diimides and Copper Phthalocyanine Semiconductors Distinguishable Over a Wide Analyte Range" *Adv. Funct. Mater.* **2013**, *23*, 4094.

2. Kola, S.; Kim, J. H.; Ireland, R.; **Yeh, M.-L.**; Smith, K.; Guo, W. Katz, H. E. "Pyromellitic Diimide-Ethynylene-Based Homopolymer Film as an N-Channel Organic Field-Effect Transistor Semiconductor" *ACS Micro Lett. 2013*, **2**, 664.

3. Kola, S.; Tremblay, N. J.; **Yeh, M.-L**.; Katz, H. E.; Kirschner, S. B.; Reich, D. H. "Synthesis and Characterization of a Pyromellitic Diimide-Based Polymer with C- and N-Main Chain Links: Matrix for Solution-Processable n-Channel Field-Effect Transistors" *ACS Micro Lett.* **2012**, *1*, 136.

4. Zhang, B.; Liu, Y.; Agarwal. S.; **Yeh, M.-L.**; Katz, H. E. "Structure, Sodium Ion Role, and Practical Issues for beta-alumina as a High-k Solution-Processed Gate Layer for Transparent and Low-Voltage Electronics" *ACS Appl. Mater. Interfaces* **2011**, *3*, 4254.

5. Jung, B. J.; Tremblay, N. J.; **Yeh, M.-L.**; Katz, H. E. "Molecular Design and Synthetic Approaches to Electron-Transporting Organic Transistor Semiconductors" *Chem. Mater.* **2011**, *23*, 568.

6. Sun, J.; **Yeh, M.-L.**; Jung, B. J.; Zhang, B.; Feser, J.; Majumdar, A.; Katz, H. E. "Simultaneous Increase in Seebeck Coefficient and Conductivity in a Doped Poly(alkylthiophene) Blend with Defined Density of States" *Macromolecules* **2010**, *43*, 2897.

## PATENTS

1. Fisher, K. C.; Huang, Q.; Papa Rao, S. S.; **Yeh, M.-L.** "Photovoltaic device with aluminum plated back surface field and method of forming same" US 20130014812 A1, **2013**.

2. **Yeh, M.-L.**; Yu, C.-H.; Lin, K.-C.; Bao T.-I.; Jeng, S.-M. "Forming semiconductor device e.g. damascene interconnect structure involves forming porous dielectric layer; forming opening in porous dielectric layer; and selectively forming pore sealing layer along sidewalls of the opening", US 7564136. Granted Jul. 21, 2009.

3. Jeng, S.-M.; **Yeh, M.-L.**; Bao, T.-I.; Lin, K.-C. "Forming semiconductor device having low-k dielectric layer, involves forming hydrocarbon layer on the low-k dielectric layer, forming a recessed feature using plasma etching, and forming conductor in the recessed feature", US 7365026, Granted Apr. 20, 2008.

4. Lin, K.-C.; Jeng, S.-M.; **M.-L. Yeh**, Bao, T.-I. "Sealing pores of low-k dielectrics using CxHy", US 7135402. Granted Nov. 14, 2006.